RF COUPLING TO REALISTIC WIRE SYSTEMS IN COMPLEX ENVIRONMENTS

A DISSERTATION IN
Electrical and Computer Engineering
and
Physics

Presented to the Faculty of the University of
Missouri-Kansas City in partial fulfillment of
the requirements for the degree

DOCTOR OF PHILOSOPHY

by
MOHAMED Z. M. HAMDALLA

M.S. Electrical Engineering,
Arab Academy for Science Technology & Maritime Transport (AASTMT), 2016
B.Sc. Electronics and Communications Engineering,
Arab Academy for Science Technology & Maritime Transport (AASTMT), 2012

Kansas City, Missouri
2021

RF COUPLING TO REALISTIC WIRE SYSTEMS IN COMPLEX ENVIRONMENTS

Mohamed Hamdalla, Candidate for the Doctor of Philosophy Degree

University of Missouri-Kansas City, 2021

ABSTRACT

With the continuous emergence of new wireless technologies, the possibility of unintentional electromagnetic interference (EMI) increases significantly. EMI coupling pathways to any Device Under Test (DUT) can be classified into two categories: front-door coupling and back-door coupling. Front-door coupling is interference through the DUT's intended receiving elements such as antennas and sensors. In contrast, the back-door coupling is interference through cables, traces, and slots not intended for electromagnetic reception, which is more challenging to predict and mitigate.

Back-door Radio Frequency (R.F.) coupling to a DUT depends on its orientation, environment, and the convoluted properties of its wires and linear/nonlinear load terminations. In this work, we adapted the Characteristic Mode Analysis (CMA) to quantify the variations in R.F. coupling with the DUT's orientation. CMA decomposes the currents excited on the DUT by the impending electromagnetic waves in a set of fundamental modes. CMA is used to identify the significant modes within the frequency band of interest and the radiation characteristics of these modes. The orientations that maximize coupling to the DUT can be identified using these two factors. However, R.F. coupling also depends on both the wires and the electronic devices connected by these wires in the DUT. The Equivalent Circuit Approach (ECA) provides a unique solution to this complicated coupling problem by modeling the wires

as a receiving antenna represented by a Thevenin equivalent circuit terminated with the linear/nonlinear load of interest. The advantages of the ECA are that it provides physical insight into the factors that dominate R.F. coupling at a fraction of the time needed by full-wave solvers.

In this work, the CMA and the ECA are adapted to predict and guide coupling to a wide range of DUTs with progressively increasing complexity. Furthermore, we augment these computational modeling approaches with innovative experimental measurements to validate their predictions. To demonstrate the versatility of the developed techniques, we apply them for the first time to guide and predict EMI to practical Unmanned Aerial Vehicles (UAV) with realistic shapes, materials, and wire distributions. We conclude by showing how the coupling approaches developed can be adapted to predict/guide R.F. coupling to a wide range of DUTs.

APPROVAL PAGE

The faculty listed below, appointed by the Dean of the School of Graduate Studies, have examined a dissertation titled "R.F. Coupling To Realistic Wire Systems In Complex Environment" presented by Mohamed Hamdalla, candidate for the Doctor of Philosophy degree, and certify that in their opinion it is worthy of acceptance.

Supervisory Committee

Ahmed M. Hassan, Ph.D., Committee Chair
Department of Computer Science and Electrical Engineering

Anthony Caruso, Co-discipline Advisor
Department of Physics and Astronomy

Masud Chowdhury, Ph.D.
Department of Computer Science and Electrical Engineering

Deb Chatterjee, Ph.D.
Department of Computer Science and Electrical Engineering

Paul Rulis, Ph.D.
Department of Physics and Astronomy

CONTENTS

ILLUSTRATIONS

TABLES

ACKNOWLEDGEMENTS

This work was supported in part by Office of Naval Research (ONR) grant # N00014-17-1-2932: "RF Coupling Re-visited," Office of Naval Research (ONR) grant # N00014-17-1-3016: "ONR Short Pulse Research, Evaluation and non-SWaP Demonstration for C-sUAV study" and School of Graduate Studies research grant program, University of Missouri-Kansas City (UMKC).

First, I thank God, the most merciful and compassionate, for this incredible opportunity to further my education and give me the power and desire to finish this work.

On a professional note, I would like to convey my profound special thanks and heartful gratitude to my supervisor, Dr. Ahmed Hassan, for his continuous support and motivation since the first day I joined Multidisciplinary Multiscale Electromagnetics Lab (MMEL). I am thankful to him for guiding me throughout all the stages of this work, including, but not limited to, teaching me the professional way of thinking, providing me with necessary references, and helping me in the presentation of this work. His direct and precise supervision was the leading guide to help me complete this work. Apart from my Ph.D. supervisor, I would like to express my gratitude to the rest of my Ph.D. committee members Dr. Anthony Caruso, Dr. Masud Chowdhury, Dr. Deb Chatterjee, and Dr. Paul Rulis, for their advice, support, and guidance throughout my degree.

I would also like to thank my fellow lab mates for the time we spent together, for their company during the sleepless nights that enabled us to meet challenging deadlines, for stimulating research ideas, and for pleasant conversations to rest my mind outside of research.

I am grateful to my parents for their unconditional love and constant support. My appreciation also goes to my siblings, who support me financially during my education.

Last but not least, I cannot express in words the gratitude I have for my wife, Mona, throughout this process. She has strongly supported and encouraged us, and at the same time, she has cared for our two children, born during my Ph.D. study! Mona, you are the foundation of our family and instilled peace, love, joy, and faith at all times. Thank you for everything you do. I am also incredibly grateful for my children| Rahma (2.5 years) and Maryam (7 months), and the joy that they have given me over the past few years. They have always led me to smile and remember what is most important during stress and anxiety.

CHAPTER 1

1 INTRODUCTION

In a highly congested wireless spectrum, electromagnetic interference poses a significant challenge in a wide range of applications. The high intensity radiated fields environment (HIRF) inspired the Federal Aviation Administration (FAA), which maintains standards for civilian aircraft, to propose specific regulations and standards for such environments [1]–[3]. Not following such standards can result in catastrophic accidents [1]. Therefore, it is essential to understand the coupling to complex electronic systems.

The coupling pathways need to be defined to understand electromagnetic interference to any complex system. The coupling pathways to any electronic system can be classified into two categories: front-door coupling and Back-door coupling. The front-door coupling is the coupling through the system receiving devices such as antennas and sensors, while the back-door coupling is coupling through the unintended coupling path such as cables, traces, and slots. The front door coupling is relatively easier to overcome and has been studied in several works of literature [4]–[7].On the other hand, the backdoor coupling is a much more complicated area of study and is the focus of this work.

The problem of undesirable RF coupling to wires and electronics has been receiving high interest for several decades. This work develops a combined experimental and modeling approach to quantify coupling to realistic wire systems in realistic environments.

1.1 Problem Statement

Bäckström *et al.* showed that field-to-wire coupling is one of the most dominant coupling mechanisms to complex systems [8]. However, the electromagnetic coupling to complex systems varies with the environment. That is its function of the orientation,

polarization, frequency, and incident direction of EM waves [9]. Therefore, estimating the worst-case coupling to wiring systems typically requires an exhaustive trial and error approach that can be prohibitive for practical devices [10], [11]. Furthermore, most of the previously reported coupling studies simplify the geometries of the wires, i.e., assume all wires are straight, which can lead to deviations from measurements of practical devices. Therefore, there is a strong need for accurate techniques that can rapidly predict RF coupling to practical DUTs. In this work, we try to satisfy this need by using two different approaches: (*i*) Characteristic Mode Analysis (CMA) and (*ii*) Equivalent Circuit Approach (ECA).

1.2 Literature Review

Wires form a significant part of most electronic systems. Therefore, a solid understanding of field-to-wire coupling is essential to predict electromagnetic coupling and interference. Three approaches have been previously applied to model the field-to-wire coupling: the quasi-static, the Transmission Line, and the full-wave approaches [12]. The quasi-static treatment, which assumes infinitely fast propagation and, therefore, is only valid for wires much smaller than the wavelength of the exciting field [12]. The Transmission Line (TL) model, as outlined by Paul [13], is the intermediate approach providing a reasonable approximation at a relatively low computational cost.

The Taylor, Agrawal, and Rachidi models are the main three models developed to understand the coupling to transmission lines [14]–[17]. The three models are similar in quantifying the electromagnetic coupling to transmission lines from external fields but different in the formulation. Several improvements for the latter approach have been reported [18]–[20].

Another fundamental approach based on the TL approach is the Baum-Liu-Tesche (BLT) equation reported in [21]. In BLT, the multiconductor transmission line network is represented graphically by tubes and junctions where the tube is a transmission line, and the junction/node is where one or more tubes meet. The graphical representation of the network facilitates the visualization of complicated networks in a more straightforward form. The original BLT equation was based on the excitation of the network by lumped voltage and current sources. The current and voltage waves on a transmission line and at the junctions can be decomposed into forward and backward traveling components. The BLT network equation can be formed by combining the current propagation and the scattering matrices for all tubes junctions. Note that each tube can represent a group of transmission lines, and each junction can represent a group of nodes. Thus, each tube and junction need to be simplified to more detailed graphs with sub-components (tubes and nodes). Although the original formulation was in the frequency domain, several attempts to extend this approach to the time domain for nonlinearly loaded networks have been reported [22]–[24]. Since the BLT equation was based on the traveling and reflecting waves along the lines and neglecting the radiation effect, another extension to the original BLT was achieved to include the effect of the EM radiation [25]. Moreover, generalization for the BLT equation was achieved to handle nonuniform multiconductor [26]. However, the BLT equation approach is a TL-based approach, which suffers from its limitations such that the TL length has to be larger than the separation between the wires and greater than the height above the ground [27].

Recently, several methods have been developed to overcome the limitation of the T.L approach while maintaining its efficient computational time compared to the full-wave approach [28]–[32]. However, most previous studies assume that the wires are above an

infinite ground plane which might not be the case in several applications. To overcome this limitation, other studies were successfully applied to two parallel wires [33], [34] and multiple wires [35], [36]. However, the new formulations can only handle straight transmission lines, and typically they can not accurately account for arbitrarily shaped wires. Different enhancements to the T.L model were proposed [37], [38]. *Wang et al*. proposed an upgrade for the T.L approach to account for the non-straight multi-wire harness [39] but without accounting for unterminated transmission lines.

Recently, several research works have been reported to model irregularly shaped wire and wire harnesses to study their electromagnetic compatibility. The reported techniques present a good compromise between accuracy and the computational time compared to full-wave solutions [39]–[48]. However, the reported techniques are applicable only for wires parallel to a metallic ground plane. The development of techniques that account for arbitrarily shaped wires with loops that are not parallel to a ground plane is still under investigation [49], [50].

Recently, many numerical approaches have been reported to predict the coupling to wires and PCBs in terms of the terminal voltages and currents along the line [51]–[54]. In addition, non-conventional techniques such as Machine learning have been evoked in estimating the voltages and currents induced on cables [55]–[57]. Although all of these studies could be sufficient for different kinds of TLs, namely twisted pairs, single wires, and PCB traces, most of these studies suffer from the TL limitation that requires a ground plane close to the TL.

The most accurate approach to evaluate the field-to-wire coupling is the full-wave approach that is based on the thin wire antenna theory [27]. However, it suffers from the most substantial computational cost, especially when dealing with long wires [27]. The full-wave approach is the primary approach followed in this work. In particular, two independent commercial electromagnetic solvers are employed: FEKO [58] and CST Microwave Studio [59]. Multiple full-wave approaches are employed to validate the results and conclusions. This work will also be extended to include experimental measurements to further validate the effectiveness of the proposed approaches.

On the other hand, several experimental studies measured and reported the electromagnetic properties and coupling of non-straight traces. Lee *et al.* investigated the difference between straight and curved TLs in terms of their radiation loss [60]. They showed that bent traces have more radiation loss than straight traces with no bends. They also showed that a 90° bent trace (L shape) has lower radiation loss than a smoother bend such as a quarter-circle bend [60]. However, they only bent the trace in one direction, which is a good representation of PCBs but not realistic for wires due to their three-dimensional (3D) flexibility.

Kasper *et al.* studied the stochastic electromagnetic field coupling to curved transmission lines experimentally [61]–[63]. The measurements were done in a reverberation chamber. The coupled voltage on a curved wire above a ground plane was calculated for different stirrer positions. The measurements observed that the induced voltage on a curved wire is higher than that of the straight wires. However, no physical insight nor explanation of such behavior is reported.

The following two computational techniques will guide the experimental measurements by predicting and quantifying the frequency and the orientation that causes the maximum electromagnetic coupling to a complex DUT.

1.3 Methodology

In this work, the differences in field-to-wire coupling between straight and non-straight wires will be quantified using characteristic mode analysis (CMA). In addition, the analysis will be extended to include realistic wire systems such as terminated wires above a ground plane, terminated wire loops, simplified wire models of a UAV, and the complete wiring system of a quadcopter UAV.

Linear and nonlinear loads will be attached to the previously described wiring systems. For nonlinear loads, the time-domain (TD) response is of great interest for electromagnetic compatibility [64]. However, CMA needs extensive processing steps when dealing with time-domain analysis [65], [66]. The TD-CMA is based on applying IFFT for the frequency domain (FD) response of the modes, which requires a high number of modes and a wide range of frequencies for each mode. On the other hand, mode tracking fails at very low frequency and for a high number of modes [65]. Therefore, we propose the Equivalent Circuit Approach (ECA) as an accurate yet straightforward approach to tackle the RF coupling to a system of wires with nonlinear loads.

The Equivalent Circuit Approach (ECA) models the wires as receiving antennas that can be represented by a Thevenin equivalent circuit terminated with the linear/nonlinear load of interest. The advantages of the ECA are: *(i)* It provides physical insight into the response of the wiring system. For example, suppose the equivalent circuit of a wiring system contains larger capacitance values. In that case, it will quickly discharge the currents and voltages

generated by a short pulse high power electronic microwave (HPEM) excitation preventing the buildup of energy in the nonlinear devices *(ii)* the ECA involves performing two full-wave simulations. After that, we can use much faster circuits simulations to simulate RF coupling to hundreds of possible nonlinear loads that can be connected to the wiring system. These simulations will be much faster when performed using a circuits solver such as LTSpice than if they were performed using a full-wave solver. Also, this will allow us to simulate practical electronics and microcontrollers which tens of components in a feasible computational time. *(iii)* the ECA facilitates the studying of wires terminated with nonlinear loads over a very long-time duration which is infeasible with a full-wave solver. Finally, (*iv*) the ECA facilitates studying wires in different practice environments, such as wires inside metallic enclosures.

One of the main techniques for predicting interference in metallic enclosures is the Random Coupling Model (RCM) [67], [68]. The RCM addresses enclosures or cavities that are much larger than the wavelength of concern. Under this condition, the wave propagation inside the cavity is chaotic, meaning that any small change in the cavity or its components will lead to significantly different outcomes. Based on the properties of the enclosure or cavity, such as its quality factor, statistical information about the voltages generated at the ports can be induced. In RCM, the ports can represent apertures in the enclosures or the input ports of devices and electronic circuitry inside the enclosure. Therefore, RCM aims to statistically quantify the interactions between the enclosures and their constituents.

In this work, unlike the RCM, we will focus on the coupling to perforated enclosures comparable in size to the incident wavelength. We will explore how the frame of a UAV can affect the RF coupling to the adjacent or enclosed wiring system. We will study UAV frames composed of different dielectrics and metallic constituents. Finally, we will develop general

guidelines to protect wires and electronic circuity from electromagnetic interference using all previously described scenarios.

1.3.1 Characteristic Mode Analysis

CMA is a full-wave electromagnetic technique that decomposes the total surface current coupled to a scatterer into a set of fundamental modes, called eigen-currents, and calculates the relative importance of each mode at any frequency [69]. The modes can be calculated using the following eigenvalue equation [70]:

$$\mathbf{X}(\mathbf{J_n}) = \lambda_n \mathbf{R}(\mathbf{J_n}) \tag{1}$$

Where **X** and **R** are the imaginary and real parts of the MOM impedance matrix of the UAV model, respectively; $\mathbf{J_n}$ is the eigen-current, and λ_n is the eigenvalue of mode n. Equation (1) above is solved at every frequency to generate the corresponding $\mathbf{J_n}$ and λ_n values. At any frequency, the total current coupled to a scatterer due to an incident field can be expressed as [71]:

$$\mathbf{I} = \sum_{n} \frac{V_n \mathbf{J_n}}{(\mathbf{1} + j\boldsymbol{\lambda_n})} \tag{2}$$

where V_n Is the modal excitation coefficient representing the coupling between the incident fields and mode n. The modal excitation coefficient V_n can be calculated using the following integral over the outer surface of the scatterer [71]:

$$V_n = \iint \mathbf{J_n} . \mathbf{E^i}\, ds \tag{3}$$

where $\mathbf{E^i}$ Is the incident electric field.

To predict the coupling to any system using CMA, the following parameters should be studied in the following order:

1. Modal significance (MS_n): identifies the relative weight of mode *n,* i.e., it describes the significance of its contribution to the scatterer's total coupled current. It can be calculated as: $MS_n = \frac{1}{|1+j\lambda_n|}$. The MS_n has a maximum value of 1, which occurs when the eigenvalue λ_n has a value of zero. The ratio between the different modes' MSn values at any frequency of interest allows us to identify the modes that dominate the coupled current. The MS_n is independent of the excitation, and it only depends on the shape, size, and material properties of the scatterer and its environment.

2. Eigen-currents or modal currents $\mathbf{J_n}$: identify the current distribution of each mode *n*. The modal currents will illustrate each mode's maximum and minimum current locations. The total current, **I**, coupled to the scatterer, is a weighted sum of these eigen-currents $\mathbf{J_n}$. Therefore, knowing $\mathbf{J_n}$'s maximum/minimum locations will facilitate predicting the locations where **I** is maximum or minimum. The eigen-currents $\mathbf{J_n}$ are also entirely independent of the excitation.

3. Modal excitation coefficient V_n: represents the coupling between the incident field and mode *n* of the scatterer. The modal excitation coefficient V_n shows which angles of incidence maximize coupling to mode *n* and which angles of incidence will cause mode *n* not to be expressed at all in the total current **I**.

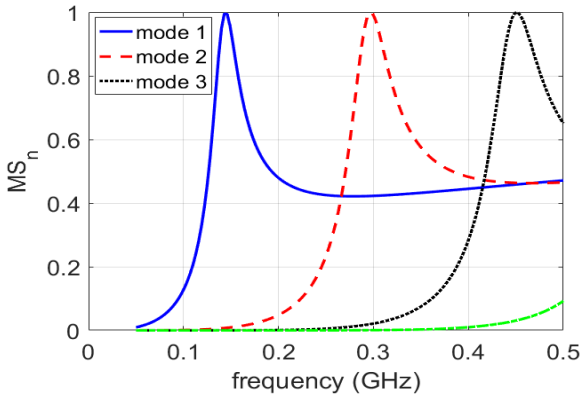

Figure 1.1 Modal significance of the first three modes of the 0.96 m single unterminated straight wire.

The following example is presented to illustrate all the previously mentioned parameters. The CMA will be applied to a 0.96 m length unterminated wire with a 6 mm radius. Fig. 1.1 shows the modal significance of the wire. In this frequency range between DC and 0.5 GHz, the wire will have three significant modes, which means three different coupling pathways. Up to 0.2 GHz, only Mode 1 will contribute to the total response, while from 0.2 GHz to 0.35 GHz, both Mode 1 and Mode 2 will contribute to the total response, but Mode 2 contributions will be more significant.

However, the total response will also depend on the modal excitation coefficient. For example, if the electric field is parallel to the wire (the blue line), the modal excitation

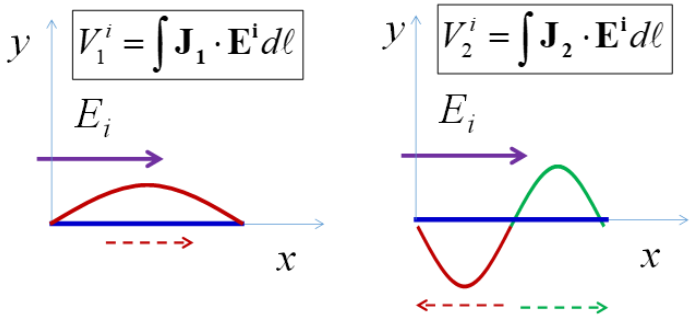

Figure 1.2 Modal currents of the first two modes of the 0.96 m unterminated wire.

coefficient of Mode 1will be the integration of the electric field with the modal current of Mode 1 (~ $\sin(\pi x)$, shown as a red curve in Fig. 1.2, where x is the normalized length of the wire). Hence, it is expected to yield a high modal excitation coefficient for Mode 1. However, for Mode 2, for the same field orientation, the positive part will cancel the negative part of the modal excitation coefficient integration resulting in zero coupling, as illustrated in Fig. 1.2.

A better graphical representation of the modal excitation coefficient is the modal field representing the effect of incident field orientation on the modal excitation coefficient. The modal fields of the unterminated wire studied here are shown in Fig. 1.3. The modal fields in Fig. 1.3 are plotted for $\varphi = 0^{\circ}$ over all θ angles. Figure 1.3 shows that if Mode 1 needs to be excited, we need an electric field with $\theta = 0^{\circ}$. However, this angle will result in a minimum modal excitation coefficient of Mode 2.

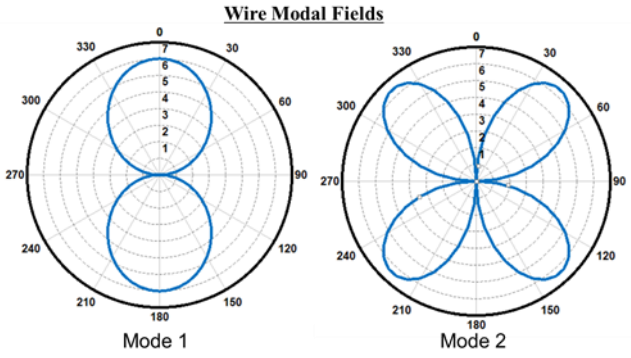

Figure 1.3 Modal fields of the first two modes of the 0.96 m unterminated wire.

For our example here, if the electric field is parallel to the wire, which means $\theta = 0^{\circ}$, it is expected to maximize the contribution of Mode 1 to the total response while Mode 2 should have zero contribution. Fig. 1.4 shows the scattering cross-section, C_{scat}, of the wire versus frequency, and it shows a peak near the resonance frequency of Mode 1, indicating that it was excited. On the other hand, no peak in C_{scat} occurs near the resonance frequency of Mode 2,

indicating that it was not excited by the incident electric field. Figure 1.4 illustrates the power of using the modal fields to predict the coupling to the wire studied herein.

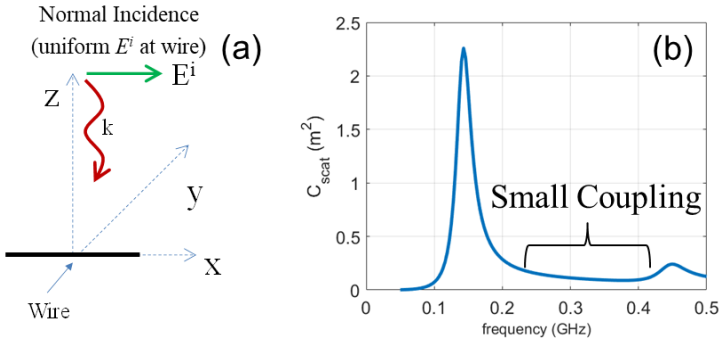

Figure 1.4 (a) The wire configuration showing the normal incident excitation field, (b) The total coupled currents to the wire over the frequency range of interest for the normal incident.

If both modes need to be excited to exhibit two peaks in the total response of the wire over the frequency range of interest, an oblique incidence is required, as shown in Fig. 1.3.

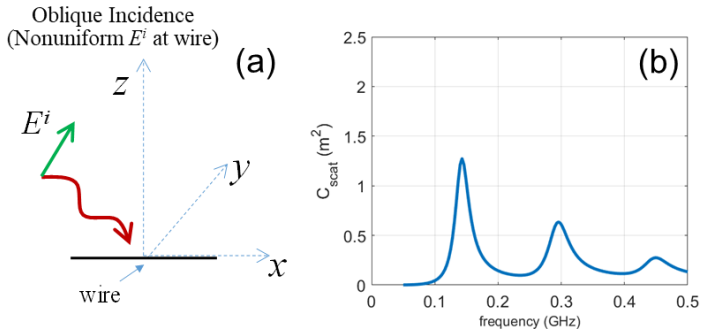

Figure 1.5 (a) The wire configuration showing the oblique incident excitation field, (b) The total coupled currents to the wire over the frequency range of interest for the oblique incident.

Figure 1.5 shows that all the modes are successfully excited for the oblique incidence, as the modal fields indicate.

In summary, CMA can predict the incident directions and frequencies to maximize coupling to practical systems like UAVs, as introduced in this section. In the next section, the parameters of the Thevenin equivalent circuit approach will be presented.

1.3.2 Equivalent Circuit Approach for RF Coupling to Wire Systems with Nonlinear Loads

Several studies have reported the use of the Equivalent Circuit Approach for different applications such as quantifying and predicting the response of shielded and unshielded wires,

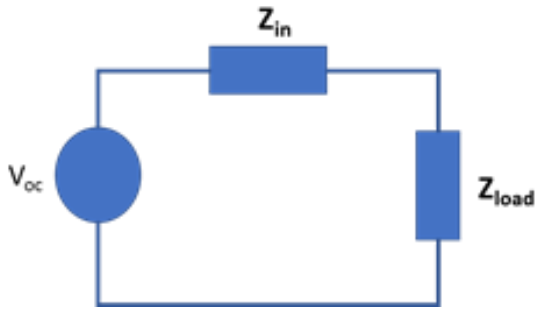

Figure 1.6 Thévenin equivalent circuit of coupling to a wiring system [88].

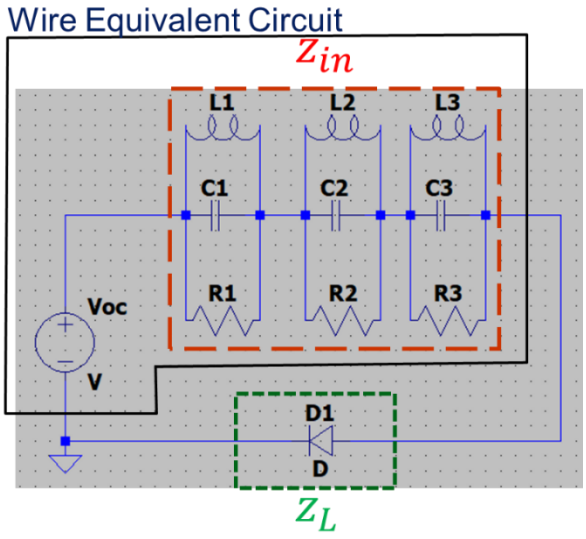

Figure 1.7 The equivalent circuit of the RF coupling to a wiring system, represented by V_{oc} and Z_{in}, connected to a load of interest, Z_L.

PCB traces, and antennas [64], [72]–[81]. This modeling approach is based on the fact that any antenna in the receiving mode, or in our case a wiring system through which back-door RF coupling can occur, can be replaced by the classical Thevenin circuit shown in Fig. 1.6 [80]. The Thévenin circuit involves two main components defined at the receiving port of the antenna or the wiring system: *(i)* the open-circuit voltage V_{oc} and *(ii)* the input impedance Z_{in} [82]. The input impedance Z_{in} is typically replaced by an equivalent circuit, as shown in Fig. 1.7. The equivalent circuit consists of a series of parallel RLC circuits for typical antennas. Typically, one RLC circuit is needed for each resonance in the frequency band of interest. The V_{oc} can be calculated by simulating the receiving antenna or the wiring system terminated with a very large load, ideally infinite. If a frequency-domain solver is used, the time-domain Voc can be easily achieved via an inverse Fourier Transform.

1.3.2.1 Validating the Equivalent Circuit Approach for RF Coupling to Wire Systems with Nonlinear Loads due to Short Pulsed Excitations

This section validates the ECA by studying different practical load combinations at various locations on the wiring system under investigation. In all of the validations in this section, the double exponential pulse shown in Fig. 1.8 is used to excite the structure [80]. The formula used to evaluate the double exponential pulse can be expressed as follows [80]:

$$E(t) = E_0 k\left(e^{-\alpha t} - e^{-\beta t}\right)h(t) \tag{4a}$$

$$k = \left[e^{-\alpha\frac{\ln(\alpha/\beta)}{\alpha-\beta}} - e^{-\beta\frac{\ln(\alpha/\beta)}{\alpha-\beta}}\right]^{-1} \tag{4b}$$

$$\beta = \frac{1}{t_r} \tag{4c}$$

$$\alpha = \frac{\beta}{\lambda} \tag{4d}$$

where $h(t)$ is the Heaviside step function. In this section, E_0 = 10 kV/m, tr = 2ns and $\lambda = 0.6$ similar to [80].

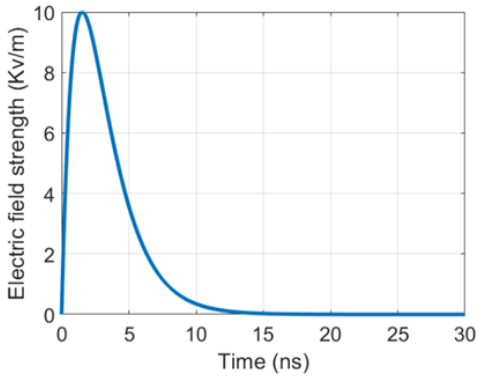

Figure 1.8 Electric field of the excitation pulse.

We studied coupling to simple nonlinear loads connected to a wiring system. In the first example, we used the equivalent circuit of a nonlinear Schottky diode similar to the model in [88]. The Schottky diode was connected to a 10.5 cm × 10.5 cm wire loop that has a radius of 0.25 mm, as shown in Fig. 1.9(a). The electric field direction is perpendicular to the loop edge that carries the diode. Fig. 1.9(b) shows the voltage across the diode calculated using both

CST MWS and LTSpice. The comparison between CST (full-wave solver) and LTSpice in Fig. 1.9(b) shows excellent agreement validating the equivalent circuit approach.

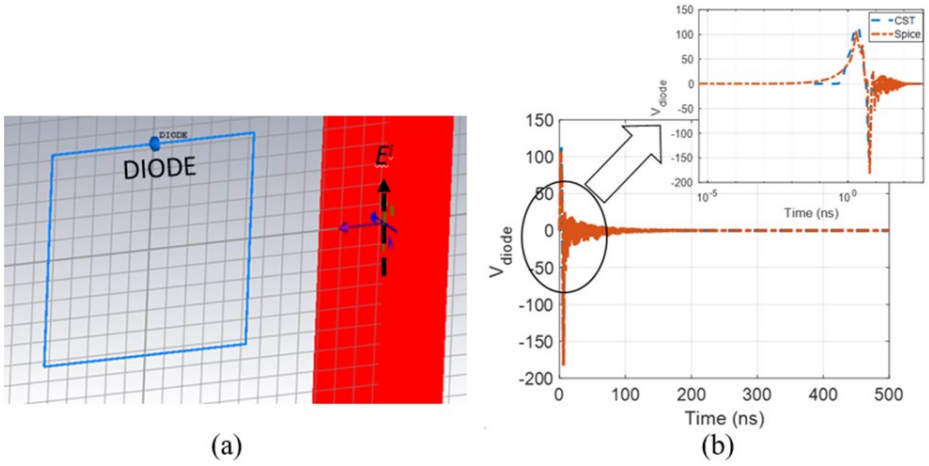

Figure 1.9 (a) Wire loop loaded by a single diode. (b) Induced voltage across the nonlinear diode, calculated using the full-wave solver (CST) and the Thévenin circuit approach (Spice).

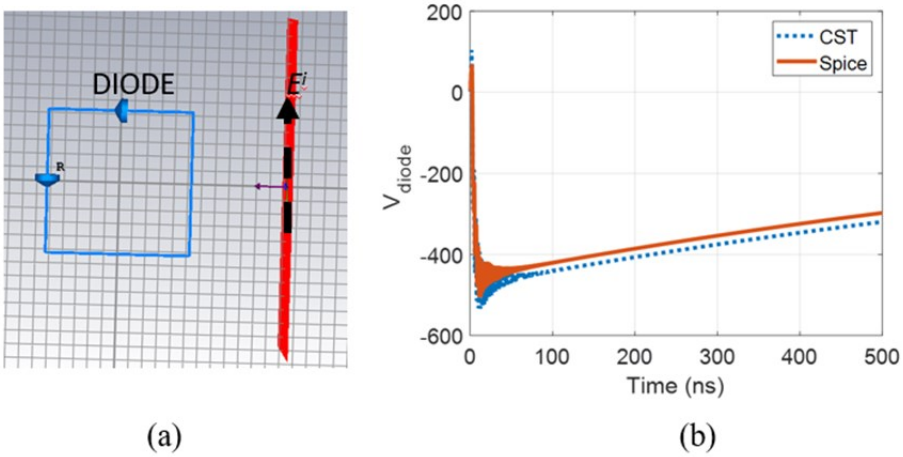

Figure 1.10 (a) Wire loop loaded by one diode and a high impedance load. (b) Induced voltage across the nonlinear diode, calculated using the full-wave solver (CST) and the Thévenin circuit approach (Spice).

Typically, a practical wire system is used to feed multiple loads. Therefore, to model a more realistic scenario, we added another high impedance load at different locations on the

loop. Fig. 1.10(a) shows the loop configuration with the Schottky diode at the upper edge of the loop and a 1 MΩ impedance at the side edge of the loop parallel to the electric field orientation. The same Schottky diode model, reported in [80], was used to achieve the results in Fig. 1.10. Fig. 1.10(b) shows the voltage across the diode, and it also illustrates the excellent agreement between CST and the LtSpice approach, even for the multiple loads' configuration.

Typically, the properties of nonlinear devices vary significantly, even for simple components like a diode. Therefore, in Fig. 1.11 and Fig. 1.12, we studied two different diode models: *(i)* An ideal diode and a practical *(ii)* 1N4148 diode. In both cases, the diode was attached to the wiring system shown in Fig. 1.11. The green and the blue arrows show the orientation of the electric field and the magnetic field, respectively, in Fig. 1.11, and for both diode models, the waveform shown in Fig. 1.10 is used to excite the structure.

The results in Fig. 1.12 illustrate the validity of the approach for the ideal and practical diodes. More importantly, Fig. 1.12 shows the significant differences between the response of an ideal diode and a practical diode. An ideal diode assumes zero resistance for forward bias and infinite resistance for reverse bias. These assumptions cause a sharp transient increase in the voltage across the diode, up to ~ -600 V, as shown in Fig. 1.12a. Moreover, it takes a long time for the voltage across the diode to discharge back to zero due to the pulse excitation shown in Fig. 1.8. However, a practical diode will have a finite reverse resistance and a parallel junction capacitance. Therefore, the maximum transient voltage for a 1N4148 diode is only -350 V versus -600 V for an ideal diode. After 500 ns, the voltage across a 1N4148 diode is less than 30 V, as shown in Fig. 1.12b, whereas for an ideal diode, the voltage perseveres to more

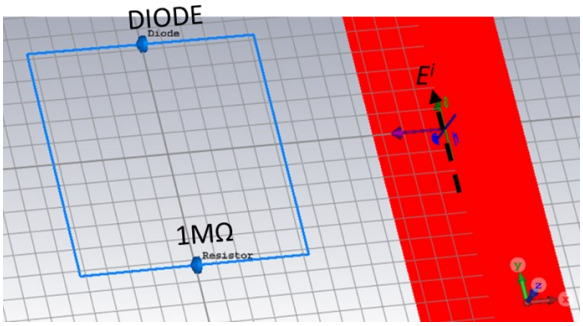

Figure 1.11 Wire loop loaded by one diode and a high impedance load opposite to the diode.

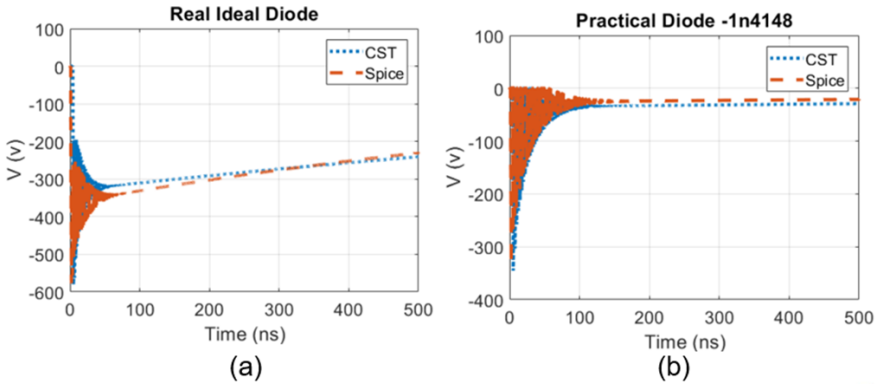

Figure 1.12 Induced voltage across the nonlinear diode calculated using the full-wave solver (CST) and the Thévenin circuit approach (Spice) for (a) ideal diode. (b) practical diode (1N4148).

than 230 V, as shown in Fig. 1.12a. Therefore, the accurate equivalent circuit of nonlinear devices needs to be incorporated in RF coupling studies and not just the ideal representation. The excellent agreement between the two solvers illustrates the accuracy of the ECA, which only requires a computational time in the order of seconds versus the several hours required by the full-wave CST. In addition, the ECA provides physical insight into the coupling problem since it explicitly shows the relative weight of the load impedance versus the input impedance of the wire. The computational efficiency of the ECA will facilitate studying multiple loads

without the need for repeating the full-wave analysis since, in this case, V_{oc} and Z_{in} are unchanged.

1.4 Research Procedure

Figure 1.13 illustrates the procedure we will use to tackle the RF coupling to a practical DUT such as a quadcopter UAV. Modeling the entire DUT will lead to a convoluted electromagnetic response, and it won't be easy to assess the contribution of each component to this overall response. Therefore, we will break down the DUT into simpler components, simulate each component individually, and combine the components progressively until the entire DUT structure is simulated. The simpler components studied herein are the wires with linear/ nonlinear loads and the frame. As illustrated in the previous section, CMA and ECA will be evoked to estimate the coupling of each component. Eventually, the conclusion of both

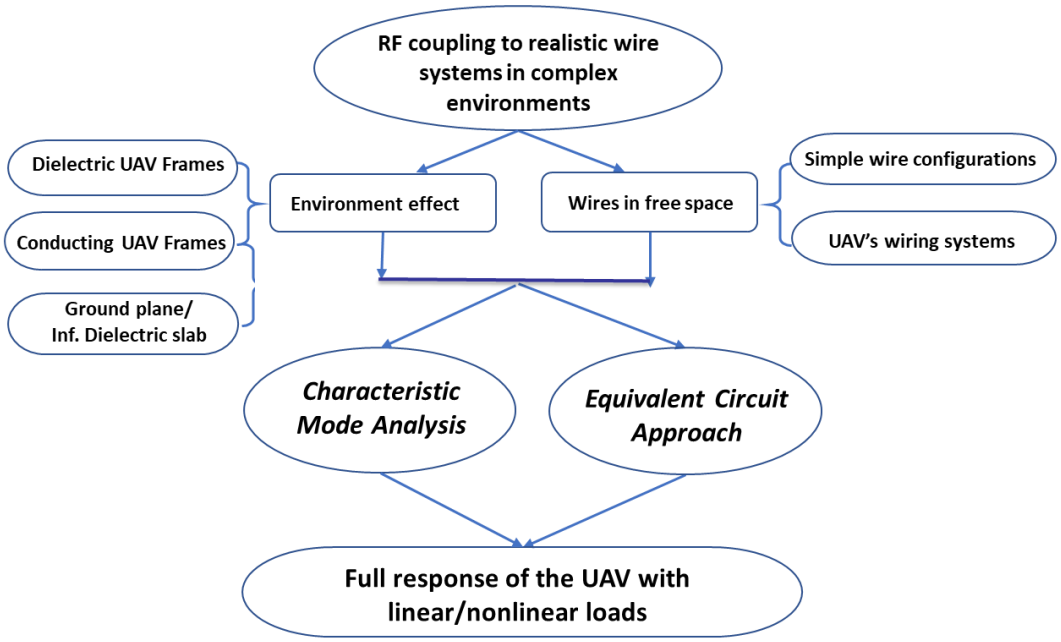

Figure 1.13 Flowchart summarizes our work for estimating the RF coupling to the realistic wire distributions of a UAV system., procedures for simplifying it, and the methods used to solve it.

approaches will be combined to predict the TD/FD response of such a complicated system in a computationally efficient time.

CHAPTER 2

2 CHARACTERISTIC MODE ANALYSIS JUSTIFICATION OF THE STOCHASTIC ELECTROMAGNETIC FIELD COUPLING TO RANDOMLY SHAPED WIRES

2.1 Abstract

Modern electronic circuits are densely packed with meandering wires with highly complex distributions. Therefore, computationally efficient approximations, assuming that the wires are perfectly straight, can calculate field-to-wire coupling values that vary significantly from the actual coupling. This work studied field-to-wire coupling to wires with realistic shapes using full-wave electromagnetic solvers. A method to generate wires with arbitrary shapes and quantifiable waviness is introduced. The simulation of these wires shows that increasing the average curvature of the wires increases the coupled current for the same field excitation. The Characteristic Mode Analysis (CMA) is used as a comprehensive method to explain these results based on the fundamental modes of the wires. The analysis presented in this work can be used for a more accurate assessment of the electromagnetic coupling to complex wire arrangements.

2.2 Introduction

A solid understanding of the field-to-wire coupling is essential to predict and avoid the failure of electronic systems due to electromagnetic coupling and interference. Three approaches have been applied to model the field-to-wire coupling: the quasi-static, the Transmission Line, and the full-wave approaches [83]. The quasi-static treatment, which assumes infinitely fast propagation and, therefore, is only valid for wires much smaller than the wavelength of the exciting field [83]. The Transmission Line (TL) model, as outlined by Paul [13], is the intermediate approach providing a reasonable approximation at a relatively

low computational cost but with certain limitations. For example, the TL length should be larger than the separation between the wires and greater than the height above the ground [84]. Finally, the most accurate approach to evaluate the field-to-wire coupling is the full-wave approach based on the thin wire antenna theory [84]. However, it suffers from the most substantial computational cost, especially when dealing with long wires [84].

This section studies RF coupling to non-straight wires using characteristic mode analysis (CMA). CMA decomposes the total surface current of a scatterer in terms of a weighted summation of a set of fundamental modes [85]. The weights of the modes accurately quantify the contribution of each mode to the total current excited on the wire [85], [86]. The main advantage of CMA is that the weights of the modes are split into shape-dependent parameters and excitation-dependent parameters. Each can be studied separately to provide additional physical insight into coupling and scattering [86]. This work applies CMA to study coupling to a single unterminated wire with a realistic shape.

This section is arranged as follows: Section 2.3 presents the computational method used to study the difference in the coupling between straight and arc-shaped wires. Section 2.4 introduces the equivalent circuit of the studied cases using CMA. Section 2.5 extends the treatment to the coupling and interference to arbitrarily random-shaped wires with quantifiable waviness. Finally, section 2.6 summarizes the conclusions and future work.

2.3 Straight vs. Curved Wires, Simulation Analysis

The commercial MOM-based electromagnetic solver FEKO is used to study field-to-wire coupling to the series of wire shapes shown in Fig. 2.1. The wires represent circular arcs with varying curvatures. The wires in Fig. 2.1 have identical lengths, L = 40 cm, diameter d =

3.6 mm, and their shapes were created by partially wrapping every wire around a circle with a different radius. Therefore, as the angle α in Fig. 2.1 increases, the curvature of the wire increases while other geometrical properties stay the same. All wires were exposed to a plane wave incident with different electric field polarizations from multiple directions. A total of 19×37 = 703 angles were simulated where the azimuthal angle "θ" varies from 0° to 180° with 10° increment and the elevation angle "φ" vary from 0° to 360° with 10° increment. Then the average coupled current over all the incident angles is calculated. Fig. 2.2 shows the coupled current generated at the center of the wires in Fig. 2.1 averaged over all angles of incidence θ and φ. Fig. 2.2 shows that the magnitude of the average coupled current increases with the angle α. The wire with the highest curvature, α = 330°, shows the most considerable average coupling current, which is 197% higher than the straight wire, as shown in Fig 2.2.

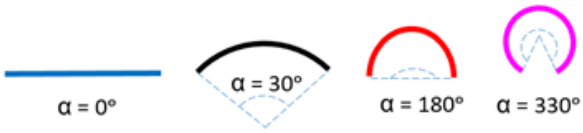

Figure 2.1 Arc-shaped wires with different curvatures.

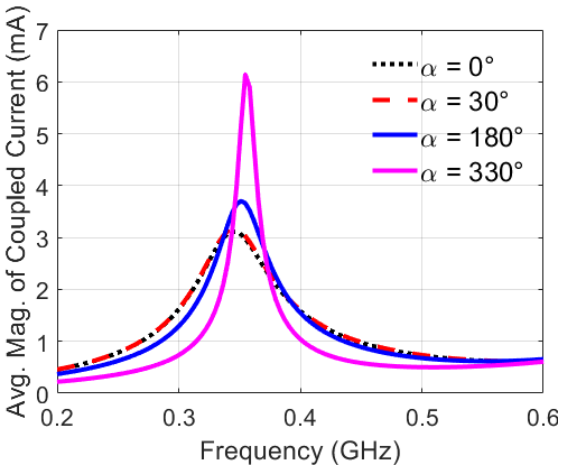

Figure 2.2 The Average magnitude of the coupled current to unterminated 40 cm arc-shaped wires with different curvatures.

To explain the increase in coupled current, we applied the CMA for the arc-shaped wires in Fig. 2.1. The modal significance of Mode 1 of the wires is plotted in Fig. 2.3 in the range from 200 to 600 MHz. By comparing Fig. 2.2 and Fig. 2.3, clearly, the coupled current to the wires is maximal at the resonance frequency of Mode 1. That is, the peak coupled current in Fig. 2.2 corresponds to Mode 1 of the wire, 344 MHz for the straight to 355 MHz for the curved wire (see Fig. 2.3). Further, Fig. 2.3 shows the bandwidth of Mode 1 decreases as the curvature of the arc-shaped wire increases, typically from 85 MHz for the straight wire to 18 MHz for the arc wire with the highest curvature, which agrees with the observations in [87]

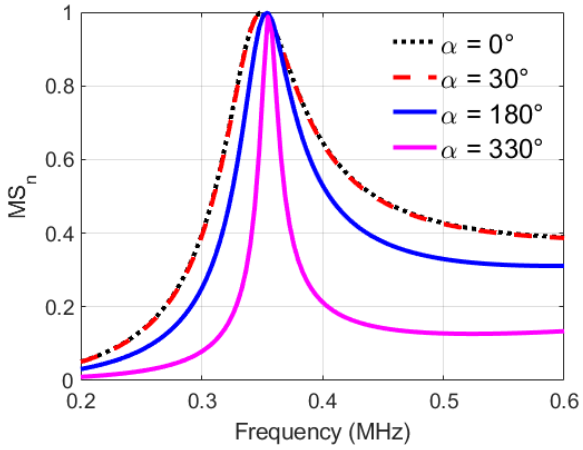

Figure 2.3 Modal significance of arc-shaped wires with different curvatures.

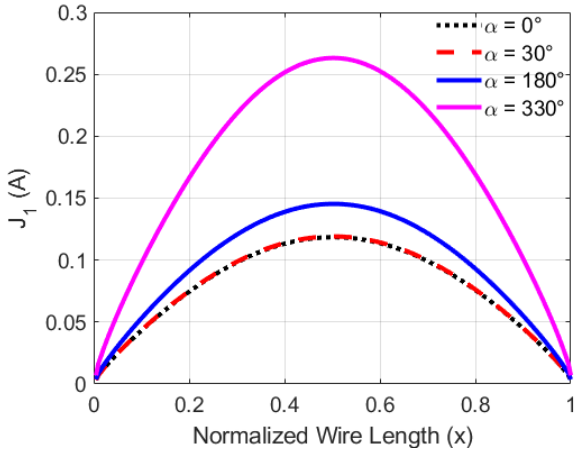

Figure 2.4 First modal current J_1 for arc-shaped wires with different curvatures.

and will be further explained in the next section. Another pattern is the resonance frequencies of the wire modes shifts slightly to higher values as the curvature increases. This behavior is similar to zigzag and mandarin wire antennas, as reported in [87], [88]. This behavior will also be justified in the next section using the CMA.

The low-frequency approximation will be introduced to illustrate the difference between the wires in terms of the magnitude of the coupled current. At low frequencies below 600 MHz, only one mode, Mode 1, contributes to the total current I, as illustrated in Fig. 2.3. Therefore, the low-frequency approximation of (1) can be expressed as:

$$\mathbf{I}(\mathbf{x}) = \frac{V_1 \, \mathbf{J_1}(\mathbf{x})}{(1+j\lambda_1)} \tag{5}$$

We calculate the modal current J_1, which is a shape-dependent parameter and independent of the angles of incidence and polarization, for each wire at the resonant frequency of its first mode. At this frequency, $\lambda_1 = 0$ yields a modal significance of unity. Fig. 2.4 shows the calculated modal currents of the 1st mode, J_1, for the wire geometries illustrated in Fig. 2.1. The amplitude of the current of Mode 1, J_1, significantly increases with the wire curvature, which is the main reason that the average coupled current to a curved wire is higher than that of a straight wire. It is worth mentioning that the coupling to a straight wire at certain angles of incidence might be higher than a curved wire. However, if we average the coupled current over all angles of incidence, the curved wire will always show a higher average coupled current due to the higher amplitude of J_1, as shown in Fig. 2.4. Fig. 2.5 illustrates the effect of the excitation orientation on the modal excitation coefficient, consequently the total induced current. In Fig. 2.5, the solid blue line represents the induced current at the center of the c-shaped (arc-wire with $\alpha = 330^o$) wire while the dashed blue line represents the induced currents

at the center of the straight wire. The red lines represent the modal excitation values for the c-shaped (solid) and straight (dashed line) wires. As the modal current at a single frequency (resonance frequency of the wire) has a fixed value, the total induced currents follow the same trend as the modal excitation coefficient.

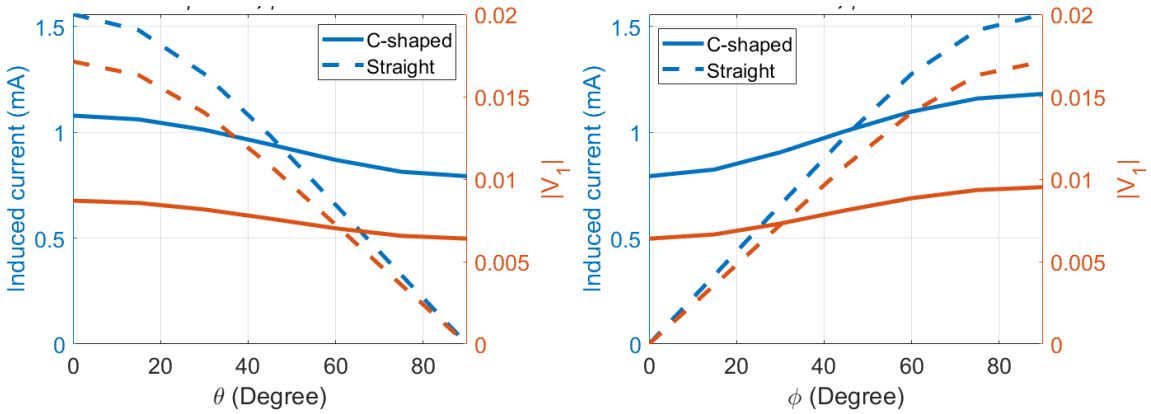

(a) (b)

Figure 2.5 The comparison between the induced currents and the modal excitation coefficient for (a) different elevation angels. (b) different azimuthal angels.

The modal currents are entirely independent of the excitation and are a feature of the geometry. This analysis shows that the highly curved wires can handle, on average, more currents than the straight ones at low frequencies depending on the excitation polarization. This conclusion is also true to some extend at slightly higher frequencies.

The equivalent circuit model of both straight and c-shaped wires needs to be introduced to explain the behavior of the resonance frequency shift and bandwidth reported herein.

2.4 Input Impedance Using CMA

An eigenmode-based approach was recently reported for modeling antenna impedances and radiation fields [89]. In this approach, the total input impedance of the antenna is

decomposed into a set of individual input impedances, each related to one mode. The physics-based circuit representations of each mode's input impedance are then developed. The input admittance of the antenna at the feed point can be written as a summation over the modal admittances as in [89]:

$$Y_{in}[m] = \sum_n \frac{\mathbf{J}_n^2}{1+\lambda_n^2}(1 - j\lambda_n) \tag{6}$$

Where $Y_{in}[m]$ is the total input impedance at the feed point, $\mathbf{J_n}$ is the Eigen current of mode (n), and λ_n are the eigenvalues.

Clearly, the total input admittance can be decomposed into a summation of a set of superimposed simple individual input impedances. The broadband impedance of each mode can be represented as a high-pass circuit [89], as shown in Fig. 2.6. The parameters of the circuit model of one mode can be estimated as follows [90]:

$$R = Q^2\, re(\frac{1}{Y_1(f_r)}) \tag{7}$$

$$C = \frac{1}{2\pi f_r Q R} \tag{8}$$

$$L = \frac{QR}{2\pi f_r} \tag{9}$$

where R, L, and C are the parameters of the equivalent circuit of each mode, f_r is the resonance frequency of the mode, and Q is the quality factor of the mode and can be calculated as follows [89]:

$$Q = \frac{f_r}{2}\frac{d\,\lambda(f)}{df}\Big|_{f=f_r} \approx R\sqrt{\frac{C}{L}} \tag{10}$$

The high-pass circuits of all the modes are combined in parallel to form the overall input impedance of the antenna. As this procedure can be applied to any system, it will be applied to the wire configurations in this paper. i.e., straight and c-shaped wire.

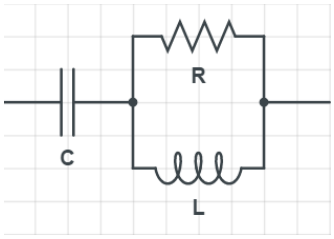

Figure 2.6 High pass circuit models for low order modes.

Table 2.1 Values of the circuit elements used to represent the input impedance of the straight and the arc wire

Circuit element	Straight	Arc-shaped
R1(Ω)	2099	9261.7
C1(pF)	1.1757	1.2005
L1(μH)	0.1758	0.1665
R2(kΩ)	1479.2	1325.7
C2(fF)	1.132	0.6234
L2(μH)	43.166	65.929
R3(Ω)	9848.7	4077.3
C3(pF)	0.14003	0.1888
L3(μH)	0.15248	0.1034

Table 2.1 summarizes the elements' values of the first three modes for both the straight and the c-shaped wire. All the values in Table 2.1 are calculated at the center of the wire. The magnitude of the input admittance of the straight and curved wire, calculated using the equivalent circuit, perfectly agrees with the input admittance calculated using FEKO, as shown

in Fig. 2.7 and 2.8, respectively. At the resonance frequency of Mode 1, the input admittance of the C-shaped wire is higher than that for the straight wire, which explains the ability of the curved wire to couple more to the external fields.

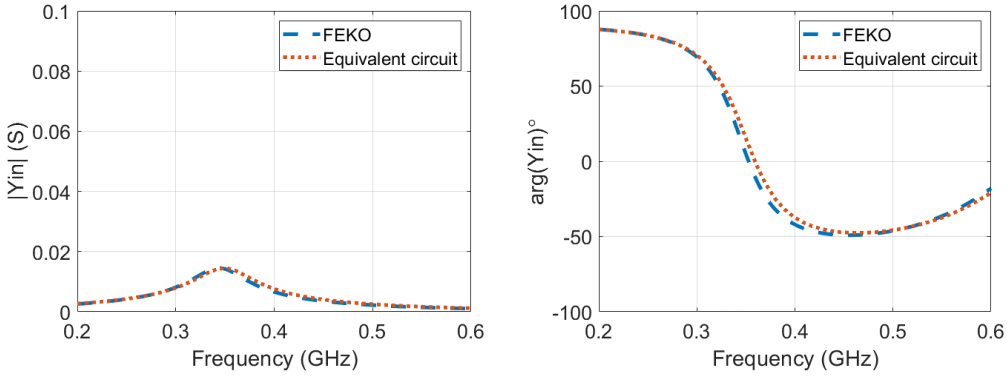

(a) (b)

Figure 2.7 (a) Magnitude, (b) phase of the straight wire's input admittance.

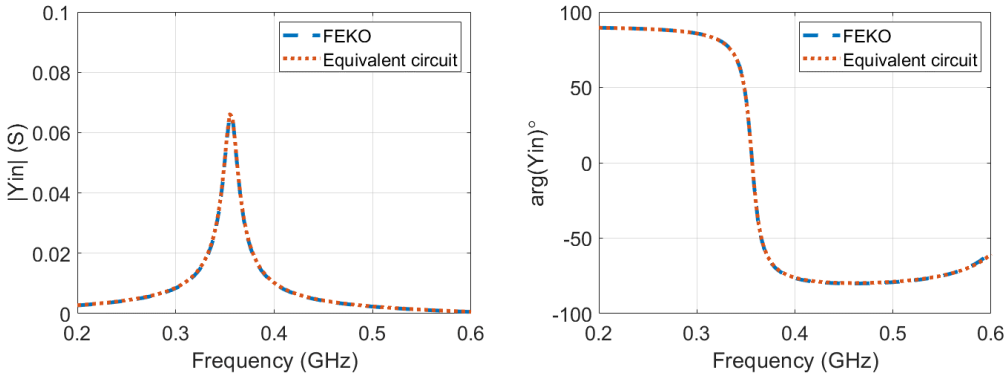

(a) (b)

Figure 2.8 (a) Magnitude, (b) phase of the C-shaped wire's input admittance.

Comparing the resistance (R1) of Mode 1 for both cases shows that the quality factor (Q) of the arc-shaped wire is higher than that of the straight wire according to (10), which consequently leads to narrower bandwidth in the frequency response of the arc-wire at the frequency range of interest. Another consequence of having a higher quality factor is the slower damping rate of any coupled signal to the curved wire than the straight wire. To test the

damping time of the coupled pulse to both wire configurations, a 350 MHz Gaussian RF pulse with 10% bandwidth, sampled at a rate of 5.5 GHz shown in Fig. 2.9, is used as excitation. The induced short circuit current at the center of the wires is presented in Fig. 2.10. Clearly, the amplitude of the induced current on the curved wire is high than that of the straight wire for the specified electric field orientation, chosen according to the modal excitation coefficient curve in Fig. 2.5. Also, the damping time of the induced pulse is higher for the curved wire because of the higher quality factor, as illustrated in this section. The signal damping time is independent of the excitation direction. It depends only on the values of the components of the input impedance, which depends on the wire shape and material properties. The same analysis

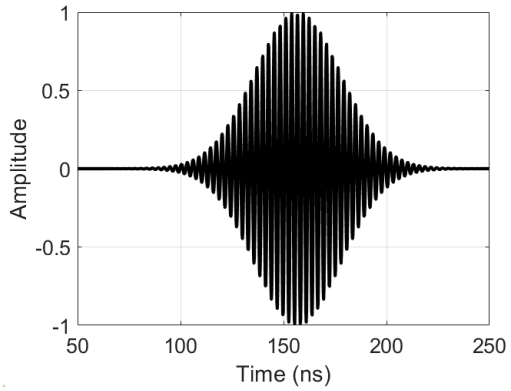

Figure 2.9 The Gaussian excitation pulse.

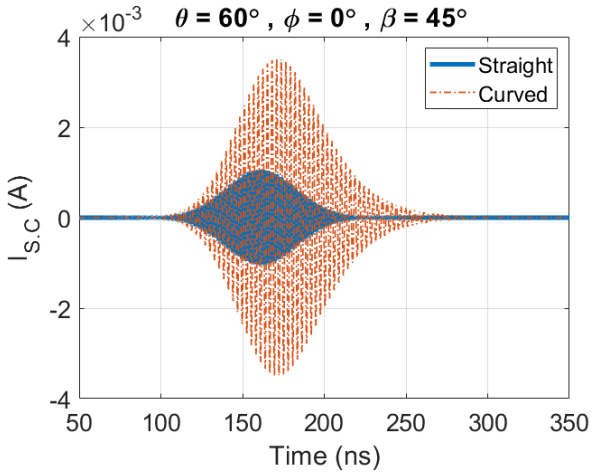

Figure 2.10 The induced currents on the straight and curved wire.

is introduced using the modal significance in the previous section and agrees perfectly with the circuit approach conclusions. Therefore, the equivalent circuit approach applied herein effectively explains the differences between the coupling between the curved and straight wires.

The fact that the coupling to curved wires can be higher than straight wires was also proved experimentally for the terminated wires in [61], [62], giving us the confidence to extend the analysis for a more realistic set of wires. Therefore, randomly shaped wires will be studied in the next section.

2.5 Characteristic Mode Analysis of Realistic Wiring System

In a realistic wiring system, wire shapes cannot be controlled to precisely match canonical shapes like the circular arcs in Fig. 2.1. Therefore, the effect of wire shapes must be quantified to assess the field-to-wire coupling and crosstalk in practical wiring systems. One approach for constructing arbitrary wires is the Random Walking Chains (RWC) model [91]. In RWC, each wire is divided into equal segments with a pre-defined length. Each segment changes its direction by randomly varying its alignment angle β, as shown in Fig. 2.11.

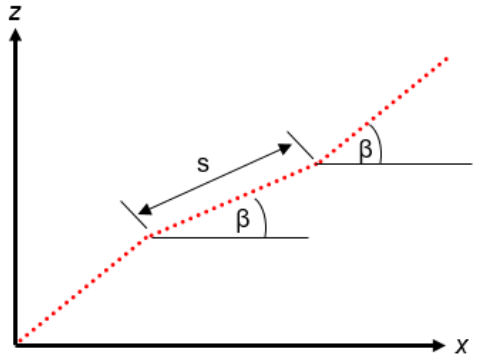

Figure 2.11 A sketch of the RWC model.

By controlling the length of the segments and the angle β, a large variety of random wire shapes can be generated. We restricted the random angle β to the x-z plane as a starting point. We used the RWC technique to generate wires with the same length but different shapes. Wires were simulated in free space to isolate the effect of the wire shape on field-to-wire coupling. All the generated wires are 40 cm long, 3.6 mm in diameter, and divided into 20 segments. We chose nine different β distribution ranges, corresponding to nine different levels of wire waviness. Three different examples of the wavy wires for different (β) are shown in Fig. 2.12.

For each β range, 100 different wire shapes were generated in a random distribution. Firstly, for each shape, the average magnitude of the coupled current, I_{shape_avg}, over multiple electric field incidence angles, the azimuthal angle "θ" vary from 0^o to 180^o and the elevation angle "φ" vary from 0^o to 360^o, is calculated at the center of the wire. Secondly, the average current over all the 100 shapes, I_{β_avg}, is calculated by averaging the 100 individual I_{shape_avg}. This value, I_{β_avg}, represents a single value of the blue curve in Fig. 2.14. The values of maximum and minimum coupled currents among the 100 Ishape_avg are shown in red. In Fig. 2.12, the average coupled current increased by ~ 40% by comparing the highest and lowest wire curvatures.

The reason for the coupled current behavior shown in Fig. 2.12 is expected to be the modal current as illustrated in the modal analysis in the previous sections. As the wire segments become closer, the interaction between these segments increases and increases the modal current of the wire. Nakamura *et al.* investigated the effect of the bent on the wire in terms of

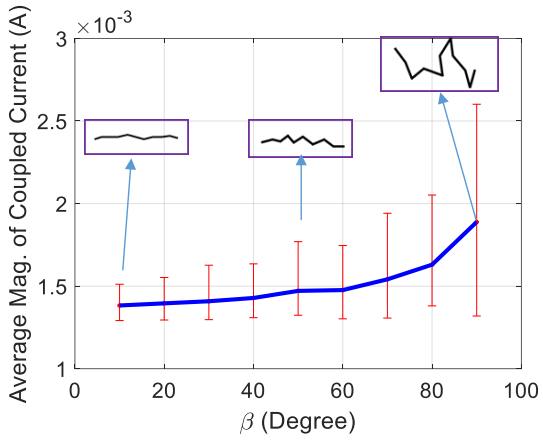

Figure 2.12 Average magnitude of coupled current to wavy 40 cm wires in free space for different waviness levels.

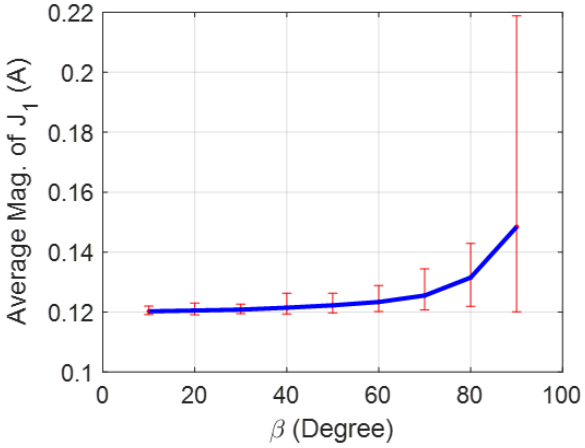

Figure 2.13 Average magnitude of J1 of an unterminated 40 cm crumbled wire in free space.

the radiation [92]. By reciprocity, the conclusions of [92] for the odd modes can be applied to Mode 1 of the wire. Fig. 2.13 shows the average calculated current of the 1st mode, J_1, for 100 wire shapes for each β angle range. The amplitude of the current of Mode 1, J_1, significantly increases with curvature, explaining the increase in the overall coupled current I of the wires.

2.6 Conclusion

Characteristic Mode Analysis (CMA) was applied as an efficient method that provides physical insight into field-to-wire coupling for complex wire shapes. Curved wires exhibit a

higher average coupling current than straight wires, with a narrower bandwidth and at slightly higher resonance frequencies. An input impedance approach using CMA was applied to explain the response of the wires in the time domain. The Random Walking Chains (RWC) model generated hundreds of complex wire shapes. Applying CMA to the wires generated by the RWC model illustrated that the modal currents magnitude increases by increasing wire waviness in agreement with the behavior shown in wires with canonical shapes.

CHAPTER 3

3 PREDICTING ELECTROMAGNETIC INTERFERENCE TO A TERMINATED WIRE USING CHARACTERISTIC MODE ANALYSIS

3.1 Abstract

Electromagnetic coupling to realistic wire configurations exhibits significant variations with respect to the interfering signal's frequency, incident angle, and polarization. In this work, Characteristic Mode Analysis (CMA) is used to calculate the fundamental modes of a terminated wire above an infinite ground plane. Then, the coupled currents to the wire's loads are predicted for different incident excitations using the properties of the modes. Using this simple but practical wire configuration, we show the versatility of CMA in practical electromagnetic interference and coupling applications.

3.2 Introduction

In a highly congested wireless spectrum, electromagnetic interference poses a significant challenge in a wide range of applications. Therefore, predicting the coupling or interfering current to a particular load in a practical wiring system has received rising interest over the last decade [93], [94]. However, for a particular wire configuration, several simulations and/or measurements are needed to exhaustively quantify the variations in the

coupled currents due to variations in the frequency, angle of incidence, and polarization of the interfering signal. This work applies Characteristic Mode Analysis (CMA) to predict the coupling to a terminated wire above an infinite ground plane. CMA decomposes the currents induced on a scatterer in terms of a set of independent modes and quantifies the modal behavior, such as the relative importance of each mode at the frequency of interest [70]. This work shows how this modal behavior can guide coupling and interference to practical wire systems.

3.3 CMA Analysis

3.3.1 Single Wire Configuration

Figure 3.1 shows a 1 m,3 mm in radius wire with a height of 0.1 m above an infinite ground plane. The wire is terminated at both ends by 50 Ω loads labeled Load 1 and Load 2,

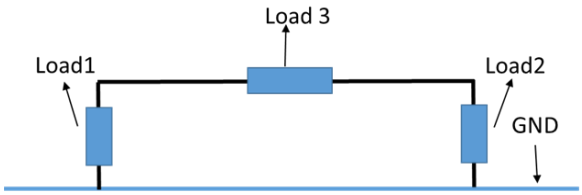

Figure 3.1 Terminated wire above perfectly conducting ground plane.

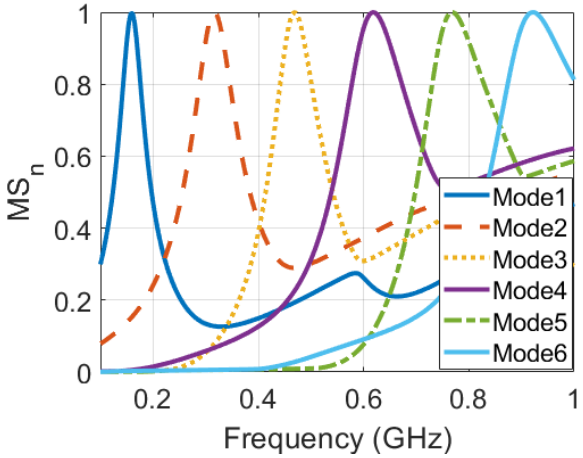

Figure 3.2 Modal Significance of the wire configuration shown in Fig. 3.1.

respectively. Moreover, a third 50 Ω load, Load 3, is attached to the middle of the wire. Despite the simplicity of the configuration in Fig. 3.1, it has practical relevance in a wide range of studies [51], [95], [96]. Next, we show how CMA can simplify the coupling analysis to the different loads in Fig. 3.1.

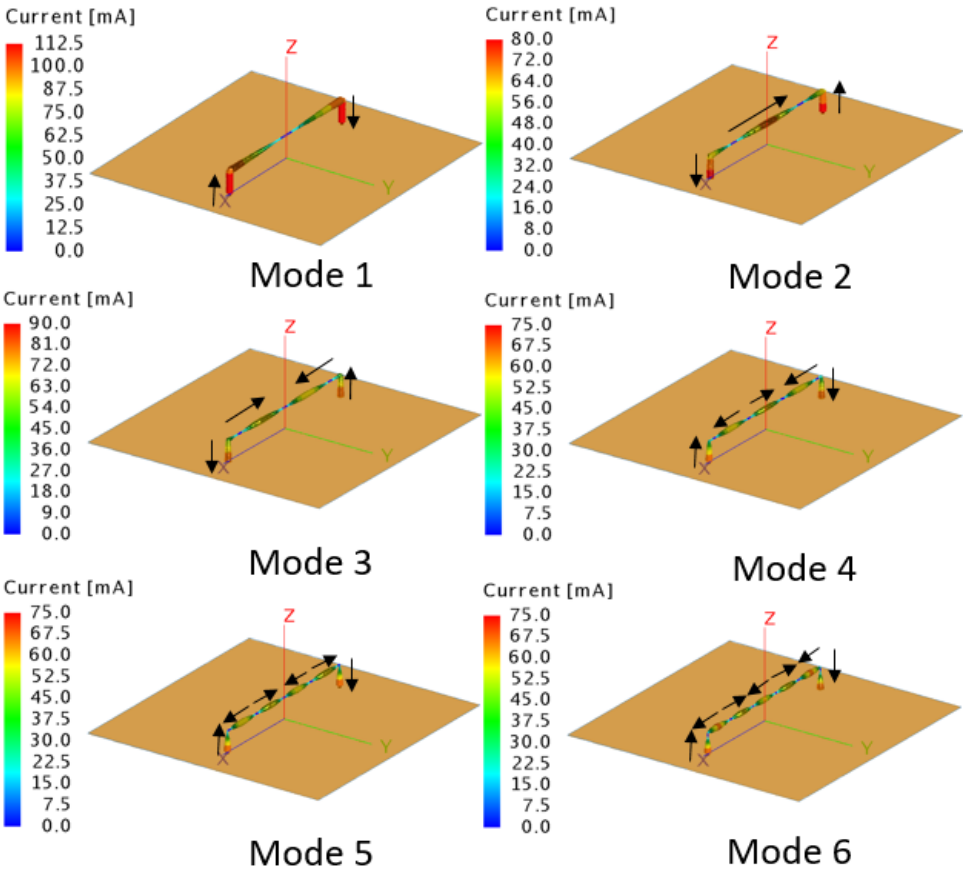

Figure 3.3 Modal currents of the first six modes of the wire configuration.

CMA provides the current distribution of the structure's fundamental modes, allowing the prediction of the response at different wire locations. For example, Fig. 3.3 shows that only the even modes, Modes 2, 4, and 6, have nonzero currents at the middle of the wire. Thus, the middle load, Load 3, is immune to coupling from the odd modes. Starting with Mode 2, Fig. 3.4 shows that Mode 2 is more efficiently excited by excitation at incidence angles of $\theta = 90^{o}$ and $\Phi = 45^{o}$ (the green curve). Fig. 3.3 shows that Mode 2 resonates at 0.3 GHz. Therefore,

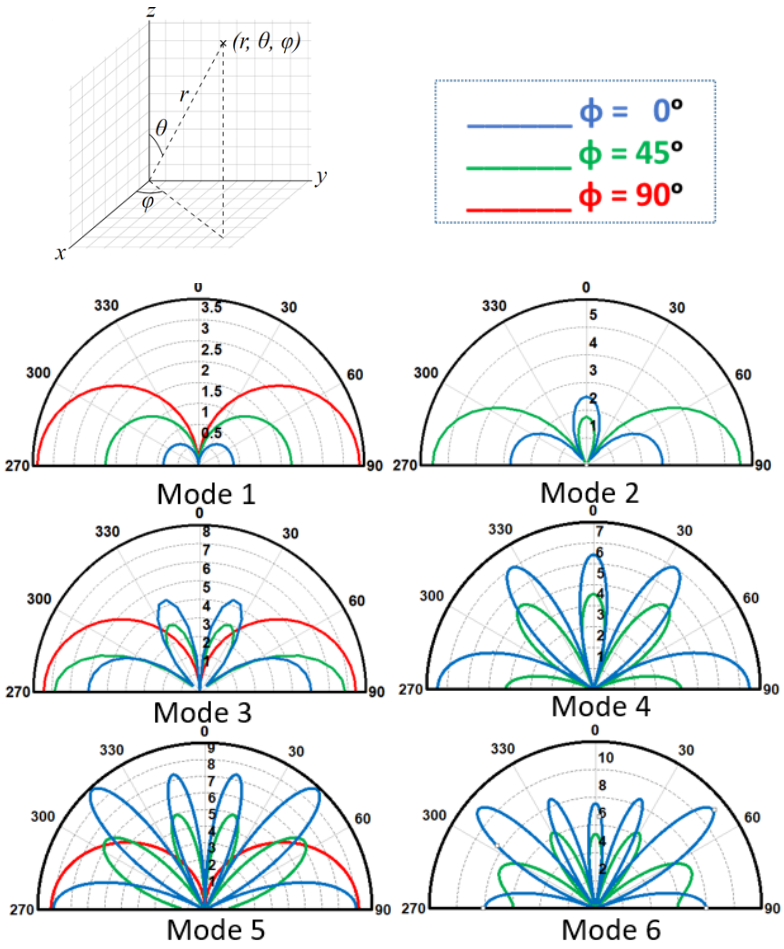

Figure 3.4 Modal fields of the first six modes of the wire configuration shown in Fig. 3.1.

Mode 3 should be strongly expressed in the coupled current to Load 3 at 0.3 GHz for an incident plane wave at angles of incidence $\theta = 90^{o}$ and $\Phi = 45^{o}$. On the other hand, Fig. 3.2 shows that Mode 6 resonates at 0.9 GHz and Fig. 3.4 shows that Mode 6 can be most efficiently excited for $\theta = 50^{o}$ and $\Phi = 0^{o}$. Therefore, at angles of incidence $\theta = 50^{o}$ and $\Phi = 0^{o}$ maximum coupling should occur at 0.9 GHz, which is the resonance frequency of Mode 6.

To test this hypothesis, Fig. 3.5 shows the coupled current to Load 3 for two different excitations. Clearly, the current coupled to Load 3 is maximum at 0.3 GHz when $\theta = 90^{o}$ and

$\Phi = 45^{o}$, due to the intense excitation of Mode 2, and the current coupled to Load 3 is maximum at 0.9 GHz when $\theta = 50^{o}$ and $\Phi = 0^{o}$, due to the excitation of Mode 6.

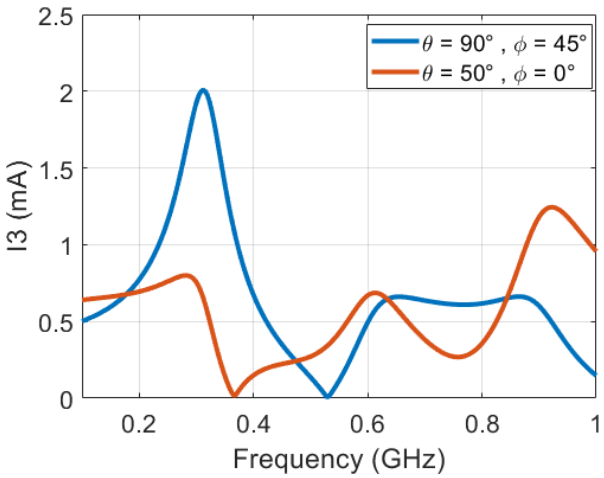

Figure 3.5 Induced current on Load 3 for different field orientations.

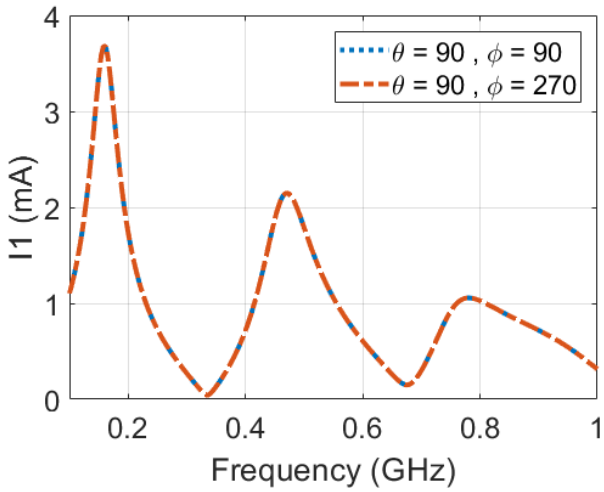

Figure 3.6 Maximum induced current on Load 1.

All the modes have high current values at the load locations for the terminal loads, Load 1 and Load 2, as shown in Fig. 3.3. However, for frequencies below the resonance frequency of the first mode, i.e., frequencies below 0.15 GHz, only Mode 1 will contribute to the current coupled to the terminal loads because it will be the only significant mode, as shown in Fig. 3.2. Fig. 3.4 shows that if the incident field is exerted at $\theta = 90^{o}$ and $\Phi = 90^{o}$, maximum

coupling to Mode 1 will occur, directly maximizing the coupling to the terminal loads. For these angles of incidence, the maximum coupling to the terminal loads will occur at the resonance frequency of Mode 1, 0.15 GHz, as shown in Fig. 3.6. As the frequency increases, the higher-order modes, both odd and even, will start contributing to the current coupled to the terminal loads according to their modal significance shown in Fig. 3.2 and their modal fields in Fig. 3.4.

3.3.2 Arbitrarily Shaped Wires

This section summarizes our conclusions for arbitrarily shaped wires terminated with loads. Fig. 3.1 is the first wire configuration, and Fig. 3.7a shows the second configuration where a wire replaces the ground plane to close the loop. 50 Ω loads terminate the loop labeled Load 1 and Load 2, respectively. Also, a third 50 Ω load, Load 3, is attached to the middle of the wire. The wire configuration in Fig. 3.7a has the exact dimensions as the configuration in Fig. 3.1. Figure 3.7b shows the corresponding modes of the wire configuration in Fig. 3.7a.

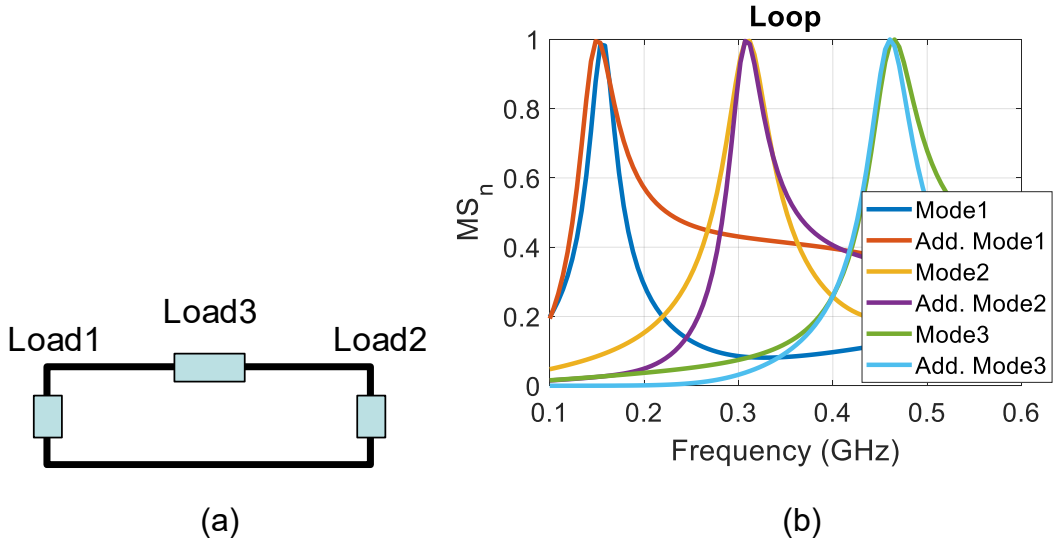

Figure 3.7 (a) Loop at free space. (b) Modal significance of the configuration in (a).

Clearly, the modes in Fig. 3.7b are double the number of modes in Fig. 3.2. The ground plane's presence halves the number of modes or reduces the number of possible coupling pathways to the wire and the loads. Another critical difference between the two configurations is that Load 3 in Fig. 3.1 will only be affected by even modes. In contrast, Load 3 in Fig. 3.7a will be affected by both even and odd modes.

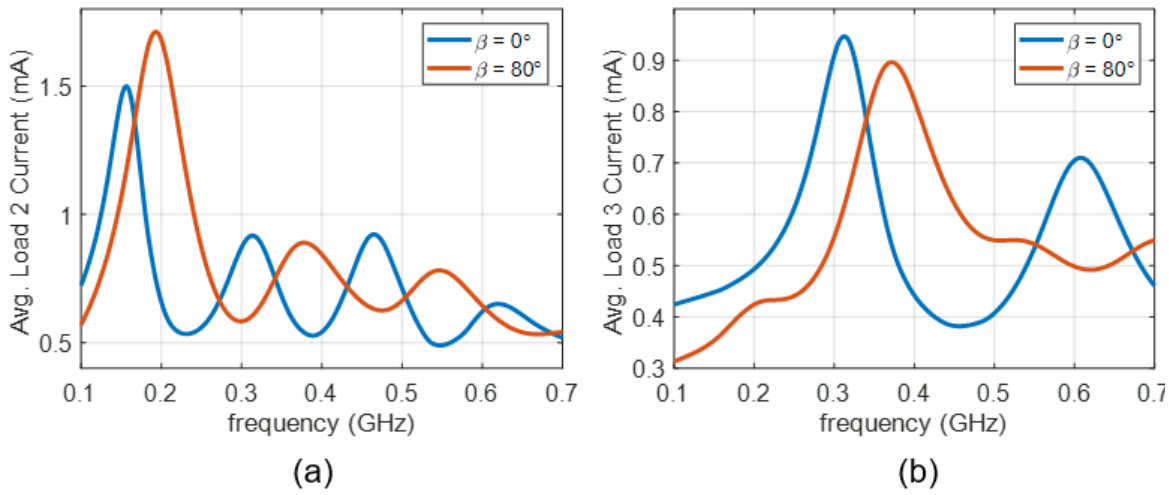

Figure 3.8 The average magnitude of the coupled current for the wire configuration in Fig. 3.1 for (a) Load 1 and (b) Load 3.

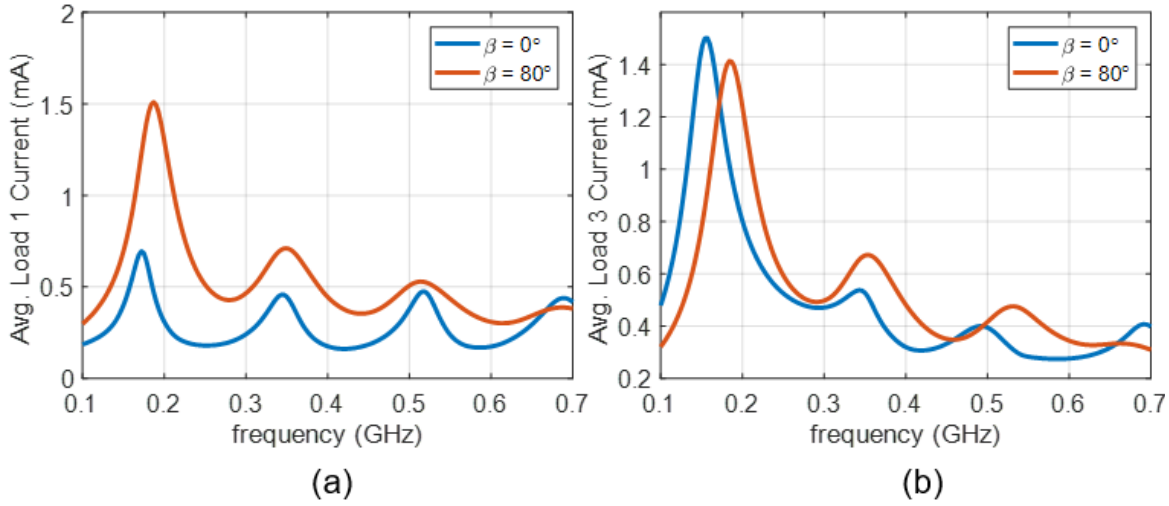

Figure 3.9 The average magnitude of the coupled current for the wire configuration in Fig. 3.7a for (a) Load 1 and (b) Load 3.

To demonstrate these predictions, the Full-wave solver FEKO is used to simulate the configurations in Fig. 3.1. The average current over multiple electric field incidence angles, the azimuthal angle "θ" vary from 0^o to 90^o, and the elevation angle "φ" varies from 0^o to 360^o, is calculated at the different loads of the two configurations. Fig. 3.8a and Fig. 3.8b show the average coupled current to Load 1 and Load 3, respectively, for the configuration in Fig. 3.1. The curve labeled as $\beta = 0^o$ represents a perfectly straight wire, whereas the $\beta = 80^o$ curve corresponds to a wire with high waviness. From Fig. 3.8, we can achieve the following conclusions:

1. The resonance frequency of curved wires constantly shifts to higher frequencies than that of a perfectly straight wire.

2. The average magnitude of the induced current on Load 1 at the first Mode for a curved wire is always higher than that of the straight wire.

3. Only the even modes can couple at the middle of the wire in Fig. 3.1a explaining the number of resonances of Load 3 as shown in Fig. 3.2b. Therefore, Load 3 is more immune to coupling than Loads 1 and 2.

The second wire configuration in Fig. 3.7a is also studied. Figure 3.9 summarizes all of our conclusions that can be presented as follow:

1. The resonance frequency of the curved loop slightly shifts to higher frequencies than the straight one.

2. The magnitude of the induced current on Load 1 of the curved wire is always higher than that of the square loop. This conclusion is valid at the resonance frequency of the first Mode,

3. Load 3, at the middle of the wire, can couple to both the odd and the even modes

4. On average, Load 3 for a curved wire is more immune to coupling and interference than Load 3 connected to a straight wire at Mode 1. However, it's the opposite trend for higher-order modes.

3.3.3 Two Wires Configuration

In this section, we performed the CMA of the wire-pair in Fig. 3.10. The first Mode of a single wire splits into two modes for a wire-pair: in-phase and out of phase. Fig. 3.11 shows the current distribution of Mode 1 and Additional Mode 1. Fig. 3.11 shows that for Mode 1 and Additional Mode 1, both wires carry currents that have a $\sin(\pi x)$ behavior where x is the normalized length of each wire. However, for Mode 1, the currents in the two wires are in phase; for the Additional Mode 1, the currents are 180° out of phase. For higher-order modes, the current distribution of each wire will be in the form of $\sin(n\pi x)$ distribution where n is the mode number. The modal significance spectrum of the wire-pair is shown in Fig. 3 for higher-order modes. The information provided by CMA can be used to predict and control the coupling to this wire configuration. For example, the CMA calculates where the different modes will resonate, as shown in Fig. 3.12. It also indicates that the out-of-phase additional modes can be more efficiently excited by oblique incidence and not by normal incidence.

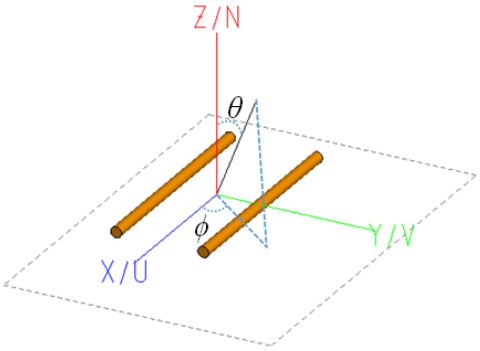

Figure 3.10 A wire pair showing two wires of radius a, length L, and inter-wire separation *d*.

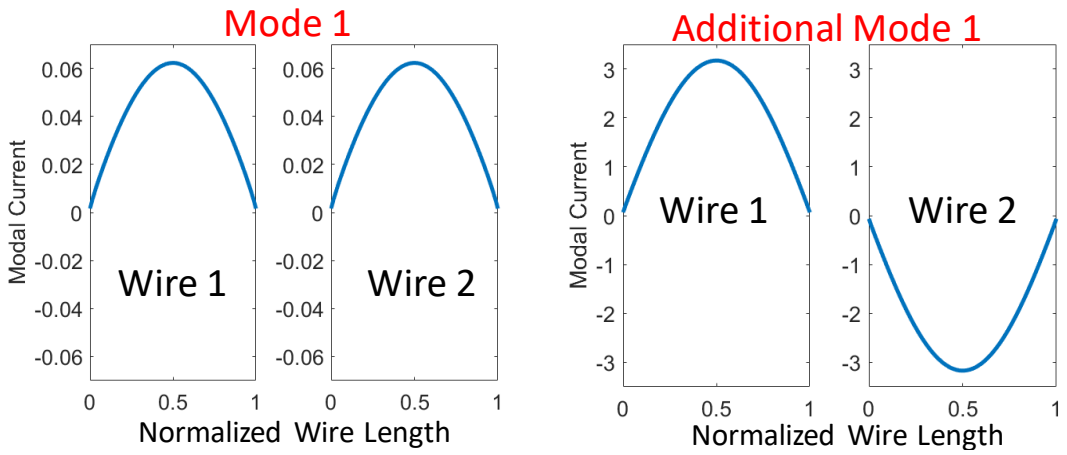

Figure 3.11 The current distribution of in-phase Mode 1 and out-of-phase Additional Mode 1.

Our goal of studying such wire configuration, regardless of its simplicity, is to perform novel experiments to prove these CMA predictions.

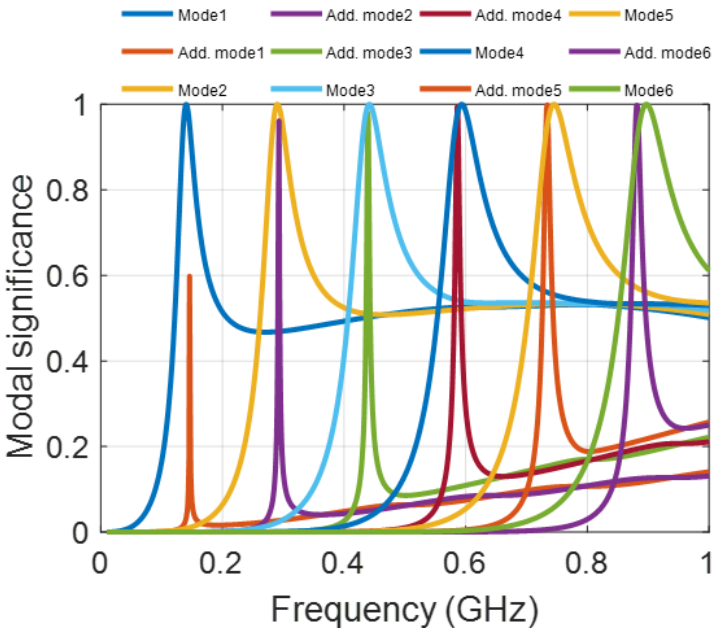

Figure 3.12 Modal significance of the unterminated wire-pair in Fig. 3.10.

3.4 Experimental Verification of CMA Predictions

The devices were placed inside an EMCO 5317 GTEM excited by a Rohde & Schwarz ZVA 24 vector network analyzer (VNA), as shown in Fig. 3.13. The wave propagates from the narrow end to the broad side of the GTEM, where pyramidal foam absorbers are placed to absorb the incident radiation and prevent reflections. The BCP-512 Broadband Current Probe with a frequency range of 1 MHz – 1 GHz was positioned at different points of interest to sample the local coupled current as shown in Fig. 3.13c. The output of the current probe is connected to port 2 of the VNA. The VNA S21 measurements are then collected and transformed into the actual coupled current values using the impedance response of the probe.

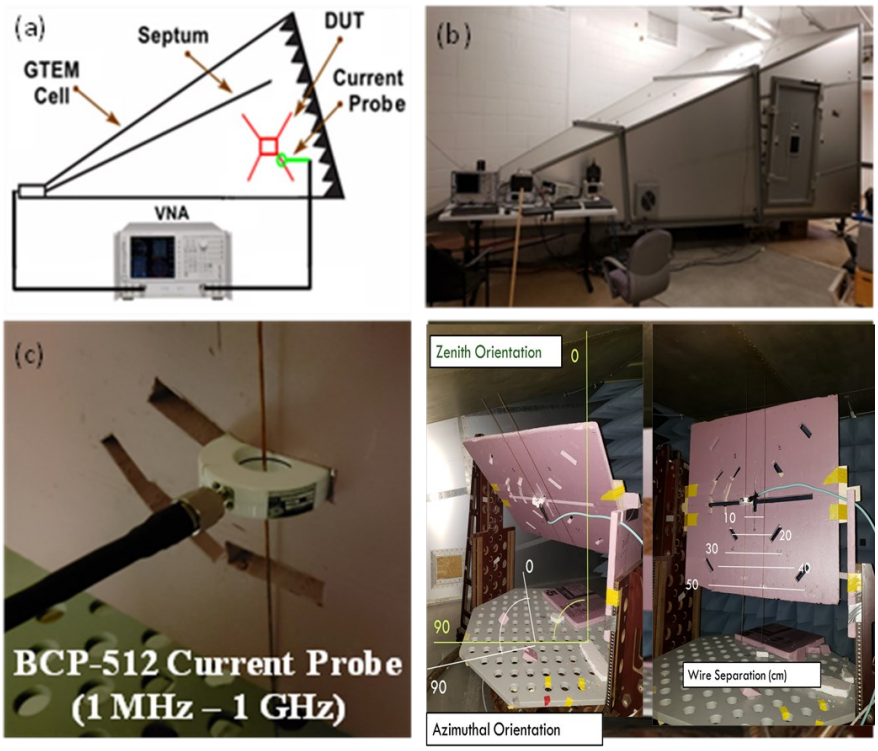

Figure 3.13 (a) A sketch of the experimental setup, (b) the GTEM cell, (c) the Current Probe (d) an example of a DUT.

Two 1 m long wires with 10 cm separation and 1 mm radius were studied Using a modeling and experimental approach. We performed the simulations and measurements for two different field directions: oblique ($\theta = 45^\circ$ and $\phi = 45^\circ$) and normal incidence ($\theta = 0^\circ$ and $\phi = 0^\circ$). the experiment was performed using the GTEM to measure the coupled currents to the studied cases, as illustrated in Fig. 3.13d. The current probe was positioned at the center of one of the wires in the pair. Fig. 3.14 shows a comparison between the measured and simulated coupled current for a wire pair at normal and oblique incidence. Excellent agreement is achieved, indicating the accuracy of both the measurements and the simulations.

Moreover, by comparing the two incident directions, we can see apparent differences in the coupled currents in the 0.4 GHz to 0.8 GHz frequency range. Two sharp maxima emerge

in this frequency range in the case of the oblique incidence due to additional Mode 3 and additional Mode 5. These maxima indicate coupling pathways in the 0.4 GHz to 0.8 GHz frequency range where the wires will be prone to coupling and interference. The main contribution of Fig. 3.14 is to prove the CMA predictions for a more complex wire system using accurate coupling experiments. Hence, the CMA simulations can be trusted for many complex wire distributions.

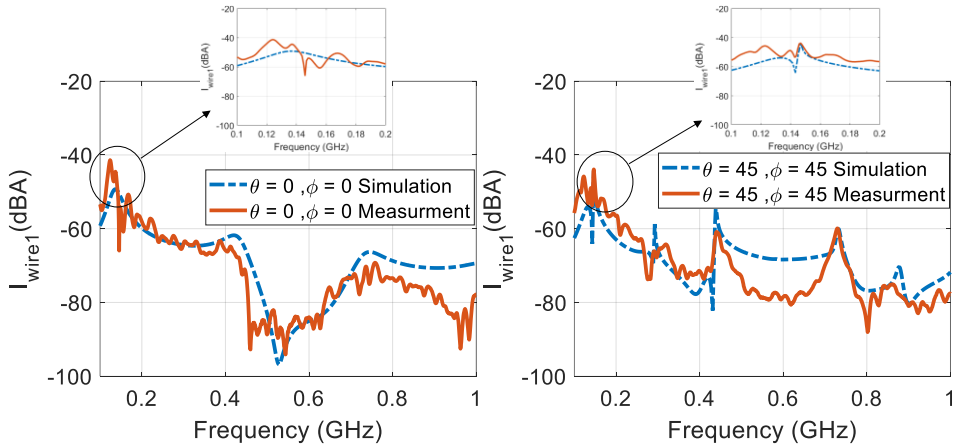

(a) (b)

Figure 3.14 The coupled current at the center of wire 1 for two different incident field angles: a) normal incidence (b) oblique incidence.

We also studied how varying the separation between the wires affects the field-to-wire coupling, as shown in Fig. 3.15 for the case of oblique incidence. Again, excellent agreement between the simulations and the measurements is achieved. Fig. 3.16 shows the coupled current near the resonance in the 0.65 GHz to 0.8 GHz range for different wire separations. Fig. 3.16 shows that the coupled current increases in magnitude and decreases in bandwidth as the separation between the wires decreases. This behavior agrees with the CMA predictions. In other words, the out-of-phase modes increase in amplitude and decrease in bandwidth as the

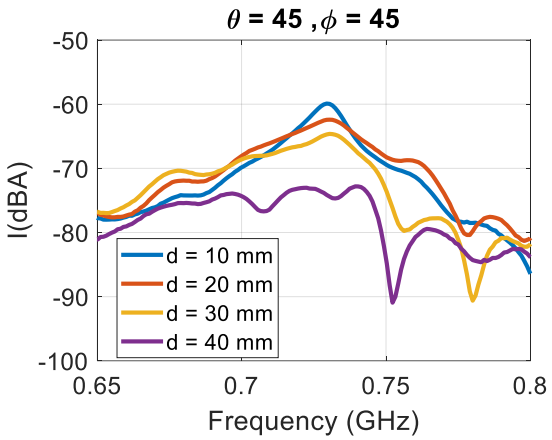

Figure 3.15 Effect of wire separation on the current coupled to a wire pair.

separation between the wires decreases. The analysis in Fig. 3.15 and Fig. 3.16 shows that the current coupling estimates based on only a single wire may underestimate the coupling and

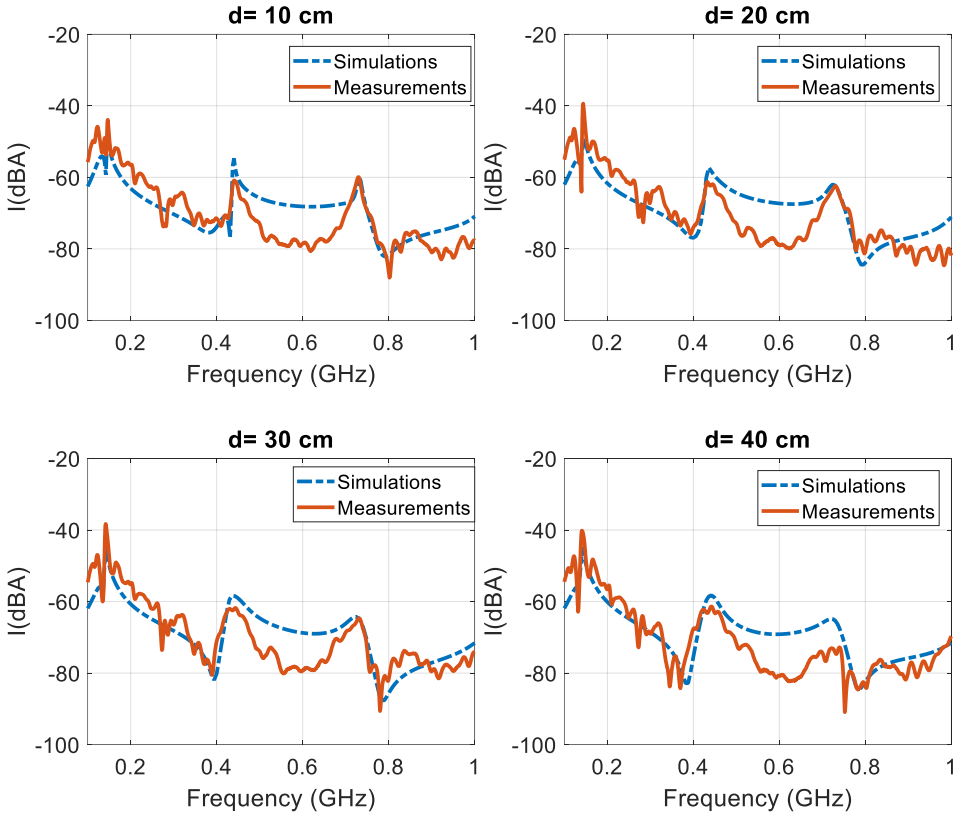

Figure 3.16 Comparison between the simulations and the measurements of two unterminated wires in free space for different values of wire separation (d).

interference when placed in a bundle.

For the oblique incidence case, there is a slight discrepancy between the simulated and measured current in the central frequency range between 0.4 GHz and 0.7 GHz. To investigate this discrepancy, we repeated the simulations for θ and ϕ values that are slightly different from the exact value of 45 degrees and plotted the results in Fig. 3.17. As a result, the central region of the coupled current became much closer to the measurements. However, the other regions

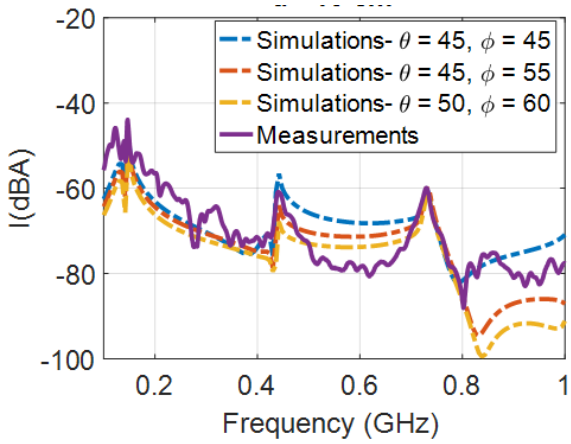

Figure 3.17 Sensitivity analysis of the coupled current to variations in θ and ϕ.

stayed insensitive to these small θ and ϕ variations, as shown in Fig. 3.17, which indicates a slight misalignment in the direction of the incident field concerning the DUT. We hypothesize that this misalignment was caused by a shift in the DUT orientation or by the slight inhomogeneity of the electric field inside the TEM cell itself. Moreover, this analysis shows that some frequency regions are more sensitive to the orientation of the DUT than others. It, therefore, will require a finer step size in varying θ and ϕ, which can help guide the RF coupling analysis and experimental measurements.

3.5 Conclusion

Three different simple wire configurations were studied computationally and experimentally to prove the validity of the Characteristic Mode Analysis (CMA) in the EMC applications. CMA was applied to identify all the modes of the structures and the possible ways to maximize/minimize coupling to each mode. Moreover, the experimental validation example previously discussed validates the versatility of CMA for predicting coupling to simple wire systems. The next chapter demonstrates the capability of CMA to quantify coupling to a more complex wire system.

CHAPTER 4

4 CHARACTERISTIC MODE ANALYSIS PREDICTION AND GUIDANCE OF ELECTROMAGNETIC COUPLING MEASUREMENTS TO A UAV MODEL

4.1 Abstract

This work studies the current coupled to a simplified Unmanned Aerial Vehicle (UAV) model using a dual computational and experimental approach. The simplified surrogate structure reduced the computational burden and facilitated the experimental measurement of the coupled currents. However, a wide range of simulations and measurements must be performed for a practical system to analyze the induced current variations concerning the incident excitation waveform properties such as the frequency, angle of incidence, and polarization. Characteristic Mode Analysis (CMA) was used to compute the eigen-currents of the UAV model and predict where and under which RF excitation conditions the coupled current is maximized. We verified these predictions using direct experimental measurement of the coupled currents. The presented simulations and measurements show the usefulness of CMA for studying electromagnetic coupling to practical systems.

4.2 Introduction

Unmanned aerial vehicles (UAVs) have a wide range of applications and typically operate in congested wireless environments that may cause unwanted interference [97]–[101]. In addition, the commercial UAV industries have recently expressed interest in using UAVs as mobile base stations [102]–[105] and as backhaul infrastructure [102]–[105], which further exacerbate their intra- and inter-induced electromagnetic compatibility (EMC) and electromagnetic interference (EMI) protection and/or shielding requirements.

Currently, it is challenging to model and predict the induced currents in UAV wires and electronics due to electromagnetic interference [106], [107]. Numerous simulations and measurements must be performed for a specific UAV to exhaustively quantify the variations in the coupled currents due to the various flying conditions and possible environments. That is, predicting the coupled current to a UAV is complicated by the variation of its orientation relative to the direction, polarization, and frequency of the incident field. Electromagnetic coupling to practical Devices Under Test (DUTs) shows significant variations, ~ 50 dB or more, with changes in frequency, angle of incidence, polarization, and/or DUT orientation [108]–[111]. Therefore, hundreds and sometimes thousands of measurements are needed to detect the frequency and orientation that causes the maximum electromagnetic coupling to a DUT [108]–[111].

Furthermore, as the DUT gets electrically larger, its radiation characteristics become even more complex, requiring more measurements to detect the frequency and orientation for maximum coupling [110]. As a result, current EMC measurements risk under-testing, where only a limited number of frequencies and orientations are tested, and therefore, the immunity of practical DUTs may be underestimated. On the other hand, measuring an extremely large

number of frequencies and orientations, i.e., overtesting, can be unnecessarily expensive and sometimes is practically unrealistic [108]–[111]. Therefore, to avoid under-testing and overtesting in EMC measurements, there is a strong need for a computational tool to guide experimental measurements by predicting and quantifying the frequency and the orientation that causes the maximum electromagnetic coupling to a complex DUT.

To meet this need, we adapt the Characteristic Mode Analysis (CMA) to guide experimental measurements by predicting the frequencies and angles of incidence where the electromagnetic coupling is maximum. CMA decomposes the currents induced on a DUT in terms of a set of fundamental independent modes and provides the relative significance of each mode at the frequency of interest [70]. CMA has been extensively employed in designing antennas and analyzing the electromagnetic scattering characteristics of various nanostructures [112]–[115]. Moreover, CMA has been previously employed to study the use of a UAV's frame as an antenna [116], [117]. We recently used CMA to study coupling and interference to wires and other simple structures [118]–[120]. A preliminary version of this work was presented in [121]. This analysis is the first experimentally verified analysis of coupling and interference to a UAV using CMA to the best of our knowledge. Relevant previously reported CMA studies are summarized in Table 4.1 and compared to this work.

Table 4.1 Comparison Between This Work And Previously Reported CMA Electromagnetic Coupling

Referenc	Scatterer Complexity	No. Of Modes	Orientation Sensitivity	Experimental Verifications
[122]	Simple (rectangular box)	4	NO	YES

[123]	Simple (rectangular box with slot)	10	NO	NO
[124]	Medium (PCB connected to cable)	3	NO	YES
[125]	Simple (flat circuit loop)	4	NO	NO
	Simple (bent PCB)	6	NO	NO
	Simple (Heatsink model as metallic box)	6	NO	NO
[126]	Simple (High speed connector)	10	NO	NO
[127]	Heatsink	5	NO	YES
[128]	Complex (Car excited by monopole)	10	YES	NO
[129]	Complex (Airplane)	6	YES	YES
[130]	Complex (Airplane)	4	YES	YES
This work	Complex (UAV model)	11	YES	YES

Most of the papers in Table 4.1 studied the total radiated power by the DUT. The DUT, therefore, has to be connected to an external source, which is not the goal of this analysis where

coupling due to an incident plane wave is the main focus. Ma *et al.* evoked the CMA approach to utilize the characteristic modes of an airplane model to design a direction-finding antenna array operating at the HF band [129]. Wang *et al.* also employed CMA to design a VHF aircraft-integrated antenna array with switchable beams [130]. However, utilizing the aircraft frame as an antenna is not the goal of this analysis. The main goal is to avoid under-testing and over-testing by developing a predictive tool to guide experimental measurements by predicting incidence frequencies and angles that maximize coupling to a UAV. In summary, the novel aspects of this work in comparison to the previous studies in Table 4.1 are: *(i)* A detailed analysis of how CMA can be adapted to guide EMC experiments is presented; *(ii)* a novel UAV quadcopter model is studied; *(iii)* a new experimental setup to verify CMA predictions using a broadband current probe and a Gigahertz Transverse Electromagnetic Cell (GTEM) is developed.

In this paper, a quadcopter UAV and its subsystems are represented by a simplified model that consists of 4 wires attached to a square metallic patch, as shown in Fig. 1. The model was designed to represent the metallic parts typically found in a UAV since the metallic parts dominate the electromagnetic response [131]. Each of the four wires represents the fusion of all the cables commonly found in the arms of a quadcopter, whereas the square metallic patch represents the ground plane of the quadcopter controller. The fusion of the wires with the square metallic patch generates a modal behavior significantly different from that of wire or a patch by itself. The UAV model is simple enough to allow the quantitative assessment of the coupled current using both full-wave simulations and experimental measurements. Yet, the model is complex enough to generate conclusions that can be applied to a wide range of quadcopters with similar symmetries in shape.

CMA was applied to calculate the fundamental modes of the proposed UAV model and the characteristics of these modes. Then, we use these modes to predict and explain the coupled current calculated at different locations on the UAV model due to plane wave excitations at different frequencies and incident directions.

4.3 Simplified UAV Model

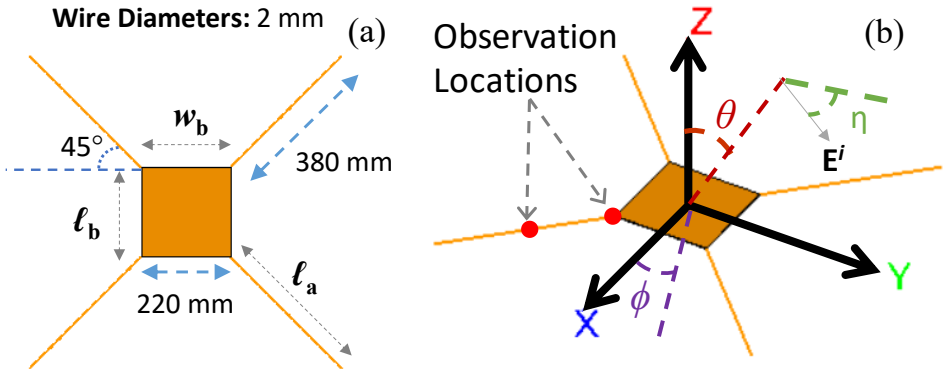

Figure 4.1 (a) A sketch of the quadcopter UAV model showing the general dimensions of the structure, (b) A sketch of the model showing the UAV model orientation with respect to the angles θ, ϕ, and η.

The simplified UAV model is shown in Fig. 4.1a. The proposed model consists of a square patch with a 220 mm edge length and four wires attached at the patch's corners. The four wires of the model make an angle of 45◦ with the edge of the square patch. The four identical wires represent the wire connections between the controller and the motors of a quadcopter UAV. The wires' lengths and radii are 380 mm and 0.5 mm, respectively. In UAVs, the wires might have larger radii. Still, we found that the radius of the wire has a negligible effect on the following results as long as the aspect ratio for the wire is high enough to maintain the thin wire configuration. A perfect electric conductor boundary condition is assigned to all model components in Fig. 4.1a.

The proposed UAV model was excited by a 150 mV/m incident plane wave at multiple angles of incidence, θ, and ϕ, as defined in Fig. 4.1b. The polarization angle (η) was fixed at

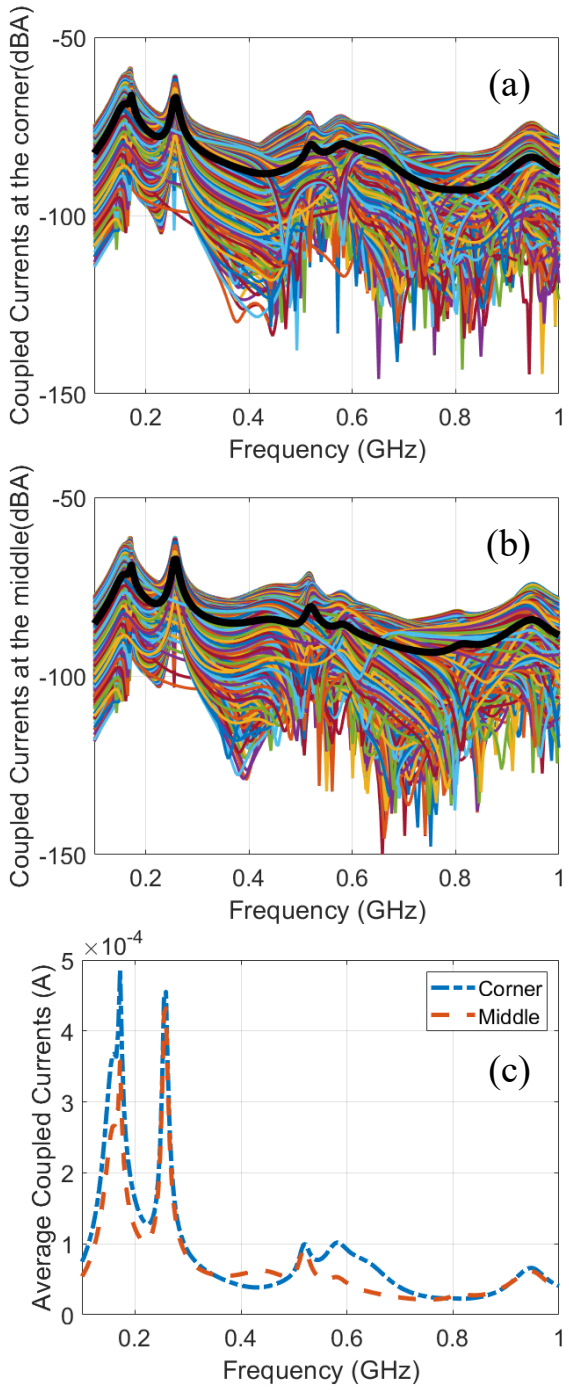

Figure 4.2 The FEKO simulated coupled current to the UAV model at 2701 different angles of incidence θ and ϕ measured at (a) the edge of the wire and (b) the middle of the wire. (c) The average coupled current over all incidence orientations.

zero in this work. However, the effect of the polarization angle will be studied in future work. The magnitude of the excitation signal was chosen to match the value in the experimental setup that will be presented in the next section. The coupling problem studied in this work is linear, so the magnitude of the excitation signal should not affect the CMA predictions.

The coupled current varies with the observation location on the UAV model. Therefore, current monitors were placed at two locations on the UAV model: *(i)* the edges of one of the four wires, where it meets the corner of the square patch, and *(ii)* the middle of the wire, as shown in Fig. 4.1b. The two observation locations will be termed corner and middle, respectively, for the remainder of the manuscript.

The UAV model was simulated using the full-wave Method of Moments (MOM) solver FEKO [58]. The simulated coupled currents versus frequency are shown in Fig. 4.2 for 2701 different angles of incidence, θ, and ϕ, where θ varies from 0˚ to 180˚ in a 5˚ step, and ϕ varies from 0˚ to 360˚ in a 5˚ step to cover the entire sphere covering the UAV model. Figure 4.2a shows the coupled current where the corner of the board meets the wire, and Fig. 4.2b shows the current at the middle of the same wire. Each colored curve in Fig. 4.2 represents a different incident direction, i.e., a different $\{\theta, \phi\}$ value. The black curves in Fig. 4.2a and Fig. 4.2b represent the average magnitude of the coupled current at each location versus frequency. The coupled current exhibits significant variations of more than 70 dB depending on the frequency and angle of incidence. The coupled current can even approach zero at some incidence angles, which is not shown in the log-scale curve in Fig. 4.2a and Fig. 4.2b. Figure 4.2c shows the coupled current averaged over all the incidence angles at the two observation locations. Fig. 4.2c shows the black curves in Fig. 4.2a and Fig. 4.2b except in linear scale. Clearly, the coupled current differs with respect to the observation location.

From Figure 4.2, it is difficult to predict the incidence angles that maximize the coupling current or the frequency range where the coupled current is maximum on average. Therefore, the CMA theory is briefly summarized in the following section to show how it can facilitate predicting the coupled current at arbitrary frequencies and incidence angles.

4.4 CMA of Simplified UAV Model

Using the full-wave solver FEKO, we performed the CMA of the UAV model in Fig. 4.1 over the frequency range from 0.1 GHz to 1 GHz. Then the three aforementioned CMA parameters were studied as follows.

4.4.1 Modal Significance for Simplified UAV Model

The UAV model's modal significances, MSn, are shown in Fig. 4.3. The modal significance spectrum in Fig. 4.3 shows all the possible coupling pathways to the UAV model. The peaks of the resonance frequencies of the modes represent the frequencies where the coupled current can reach maximum values. For example, Modes 1 and 2 resonate at 0.17 GHz, Mode 3 resonates at 0.19 GHz, and Mode 4 resonates at 0.24 GHz. These are the critical frequencies for the UAV model in Fig. 4.1 for the frequency range up to 0.4 GHz. Therefore, the first advantage of the CMA is that it identifies the critical coupling frequencies for the DUT. As a result, one can only focus on a few frequencies around where the modes resonate instead of testing the structure at hundreds of frequencies. Table 4.2 lists the resonance frequencies of the 11 modes in Fig. 4.3, which determine the frequency regions to characterize the UAV.

It is important to emphasize that the coupled current, for a specific excitation at a particular angle of incidence, will not show all the peaks in the MSn spectrum in Fig. 4.3. This behavior is because different modes are excited at different incidence angles, as described in

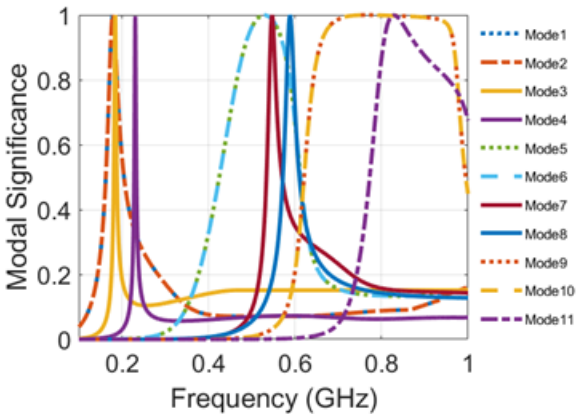

Figure 4.3 Modal significance of the first 11 modes of the proposed UAV model in Fig. 4.1.

the following paragraph. However, the MSn spectrum identifies the critical frequencies quantitatively, with no trial and error, where we need to focus our full-wave simulations and experimental measurements. Moreover, the frequency range where the modes' density is low or where the MSn does not reach high values is the frequency range where the coupled current will be lower on average than other frequency ranges of the same bandwidth. For example, the frequency range between 0.26 GHz and 0.39 GHz does not have any modes with considerable modal significance. Therefore, the average coupled current in this frequency range should be lower than that at slightly lower or slightly higher frequencies. This assertion is confirmed in Fig. 4.2 at all observation locations. In this sense, the observation of MS_n is more helpful in identifying where the coupling is *unlikely* to occur rather than where the coupling is *likely* to occur. All the previous conclusions are achieved directly from Fig. 4.3 without testing hundreds of different angles of incidence.

Table 4.2 Resonance Frequencies And Optimum Incident Angles (θ) For The UAV Modes

Mode	Resonance Frequency (GHz)	Optimum Angle of Incidence (θ°)
1	0.17	0

2	0.17	0
3	0.19	90
4	0.24	45
5	0.52	45
6	0.52	60
7	0.55	90
8	0.59	20
9	0.77	0
10	0.77	0
11	0.83	90

4.4.2 Modal Currents for Simplified UAV Model

The eigen-current distributions $\mathbf{J_n}$ of the UAV model are shown in Fig. 4.4. Each eigen-current distribution in Fig. 4.4 is plotted at the resonance frequency of its mode. The eigen-current distribution in Fig. 4.4 is normalized with respect to the maximum current value of each mode. The red arrows in Fig. 4.4 represent the general trend of the current of each mode or eigen-current, whereas the colors show the exact distribution. The hotspots of the modal currents, i.e., the locations where the modal currents are maximum, are shown in red, whereas the locations where the modal currents are zero are shown in blue. For example, Mode 1 has a hotspot at the corner observation location, whereas Mode 9 has a minimum at both the corner and middle observation locations. In general, the modal current is much more important at the corner, as this is generally where the wire connects to the electronic circuitry on board and where it would be perceived as a noise voltage.

The UAV model in Fig. 4.1, and many quadcopters, has 4-fold symmetry. This symmetry is reflected in the current distribution of the eigen-currents or modes shown in Fig.

4.4. For example, Mode 2 is identical to Mode 1 if it is rotated by 90°. Similarly, Mode 5 is identical to Mode 6, and Mode 9 is identical to Mode 10, except for a 90° rotation, as shown in Fig. 4.4. Due to this symmetry, the three previously mentioned mode pairs have identical MSn, as shown in Fig. 4.3. MS1 = MS2, MS5 = MS6, and MS9 = MS10, which means that

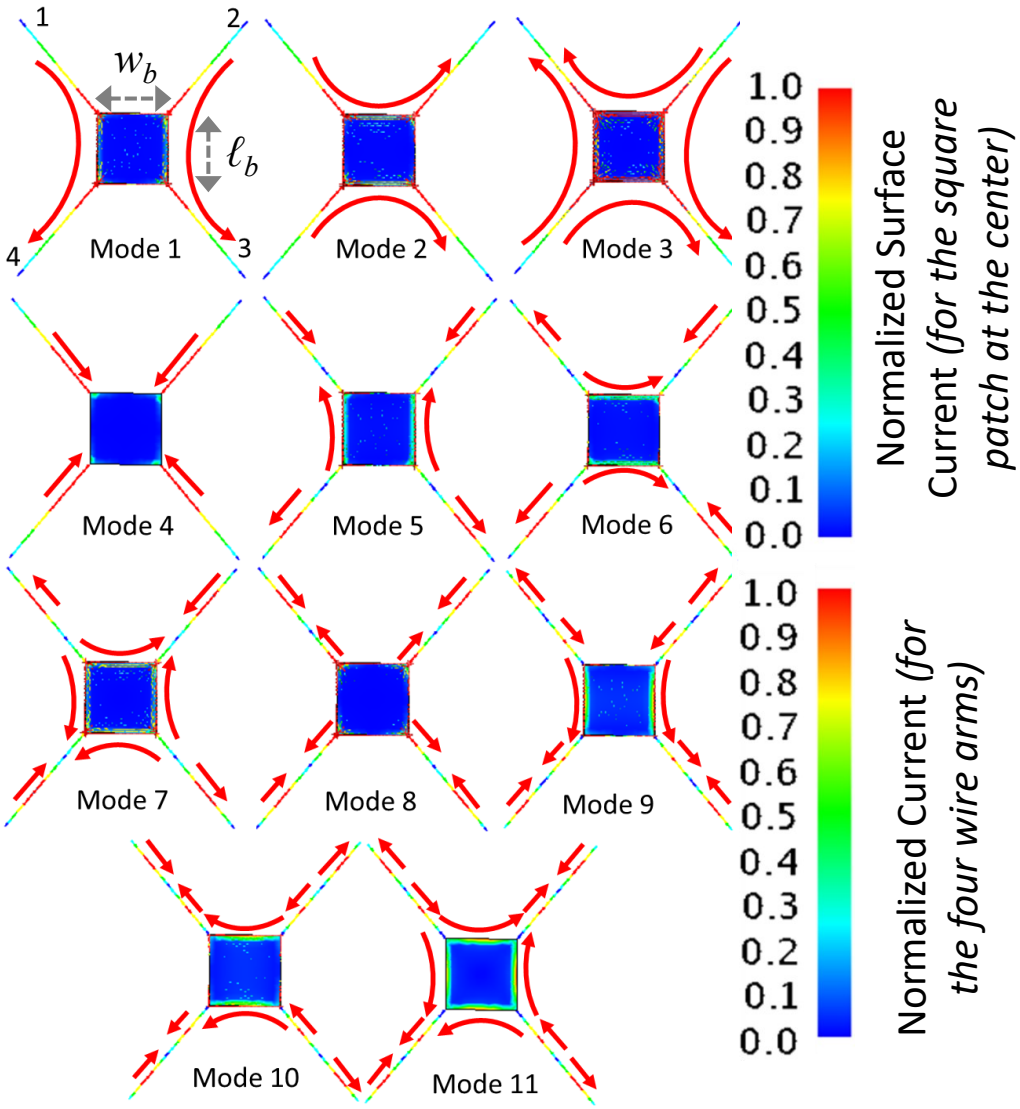

Figure 4.4 Normalized eigen-current distribution of the first 11 modes of the UAV structure. Each eigen-current distribution is plotted at the resonance frequency of its mode.

Mode 1 and Mode 2 will resonate at the same frequency. The previous mode pairs will have different modal significance if the symmetry is broken.

On the other hand, the current distribution of Mode 3 is a merge of Mode 1 and Mode 2, as shown in Fig. 4.4, and it resonates at a slightly higher frequency, as shown in Fig. 4.3. This behavior was previously reported in similar but simpler structures with 4-fold symmetry [132], [133]. However, combining the four wires to the square plate led to the emergence of new modes that were not easy to predict from the individual modes of the wire or the individual modes of the square plate.

4.4.3 Modal Fields/Radiation Pattern for Simplified UAV Model

The Modal Excitation Coefficients, Vn, can be calculated by using transverse electromagnetic plane waves at different angles of incidence, identifying the incident electric field due to this excitation, Ei, and recalculating the modal excitation coefficient Vn according to (3). The Modal Excitation Coefficients Vn of the first 11 modes, which by reciprocity can be estimated using the radiation characteristics of each mode, calculated using FEKO, are shown in the polar plots in Fig. 4.5. The radiation pattern of each mode in Fig. 4.5 is plotted at the resonance frequency of this mode and normalized to its maximum value. All the radiation patterns in Fig. 4.5 are in the θ plane with a fixed ϕ value of 0^o and a fixed polarization angle of 0°. Angles where the modal excitation coefficient is maximum represent the optimum direction to excite a particular mode. Angles of zero modal excitation coefficient in Fig. 4.5 indicate incident directions that cannot excite the mode regardless of its significance at a particular frequency. For example, Mode 4 cannot be excited at any frequency at $\theta = 0°$ or at $\theta = 90°$ for $\phi = 0^o$, and it can be optimally excited when the incidence angle is at $\theta = 45°$. Table 4.2 also shows the optimum angles to excite each mode. These angles represent the critical

angles of incidence (which can also be related to the DUT orientations) needed to accurately assess the UAV model's EMC characteristics. As a result, instead of testing thousands of angles as reported in [108], [109], the CMA-generated angles in Table 4.2 provide a significantly

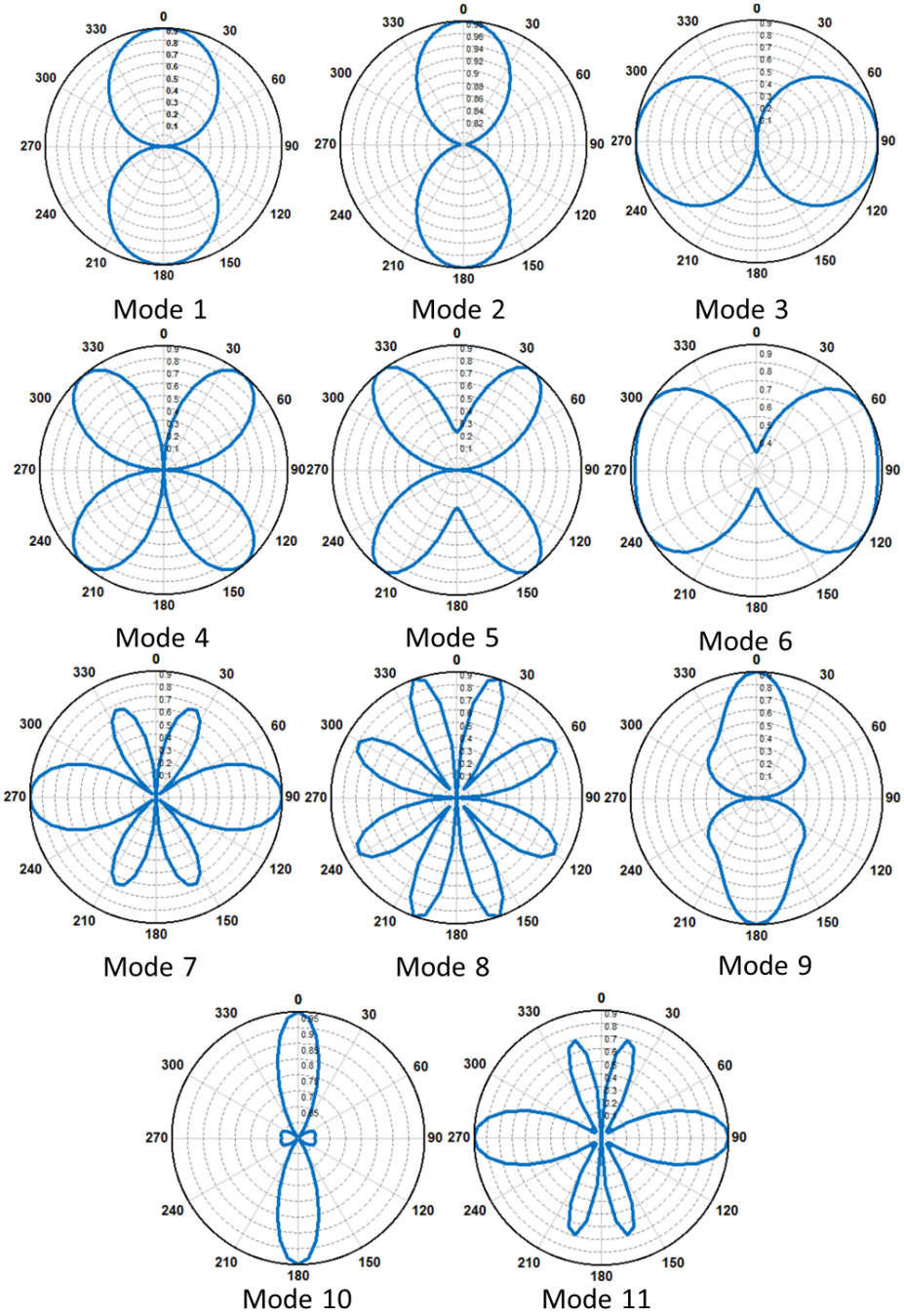

Figure 4.5 Normalized Modal Fields of the first 11 modes of the UAV model. The radiation pattern of each mode is plotted at the resonance frequency of this mode.

lower number of angles to test and measure the optimum coupling to each mode of the DUT. However, if more than one mode is significant at one frequency, the optimum angle might be in the middle between the angles in Table 4.2 and can be calculated by analyzing (2).

Most of the 11 modes are narrowband modes. Hence, the changes in the eigen-current distribution within the frequency band where a mode is significant can be neglected. For example, Fig. 4.6 presents the eigen-current distribution and the radiation characteristics of Mode 5 at three different frequencies within the bandwidth of Mode 5, i.e., at three frequencies where MS5 is larger than 0.707. The current distribution of Mode 5 and its radiation pattern does not change dramatically within the bandwidth of the mode. The magnitude of the modal current only changes slightly with frequency. Still, the hotspot locations are maintained, and the radiation pattern of the modes does not change significantly, as shown in Fig. 4.6. For frequencies that are significantly larger or smaller than the resonance frequencies of the mode,

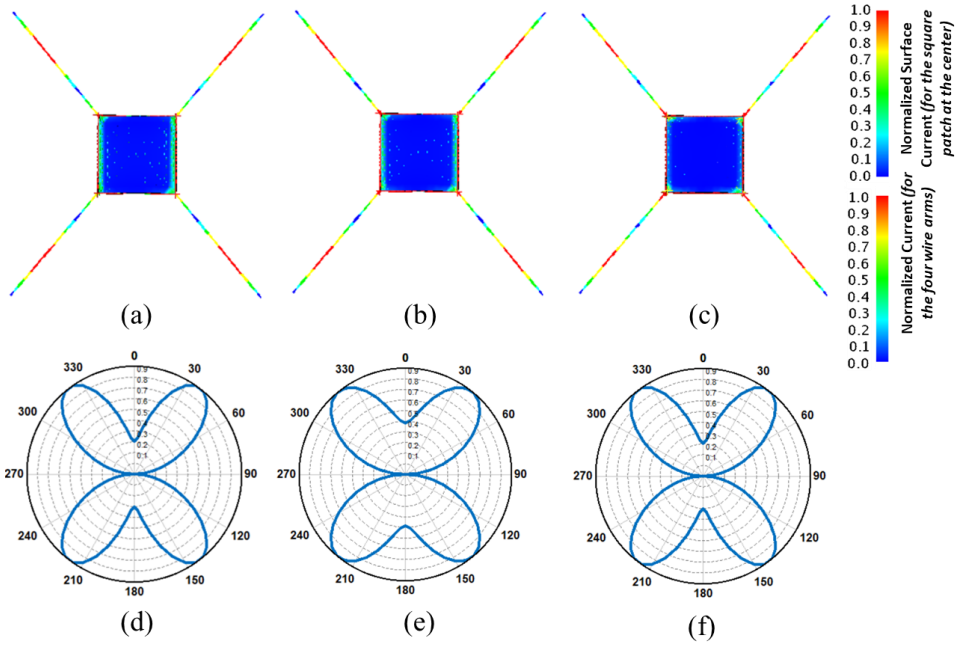

Figure 4.6 Eigen-current distribution of Mode 5 of the UAV structure at (a) 490 MHz, (b) 520 MHz, (c) 580 MHz. Normalized Modal Fields of Mode 5 of the UAV model at: (d) 490 MHz, (e) 520 MHz, (f) 580 MHz.

the eigen-currents and the radiation characteristics of a mode might show significant differences from the patterns at resonance. At these frequencies, however, the MSn of the modes will be too low to provide any significant contribution to the total coupled current.

4.4.4 Predicting The Dominant Mode

The CMA information presented in Fig. 4.3 to Fig. 4.5 allows us to understand how a wide range of excitations might couple to the UAV. For example, Fig. 4.3 can identify the significant modes in this frequency range. Next, by investigating Fig. 4.4, we can determine whether these significant modes have nonzero currents at the location of interest. Next, by examining Fig. 4.5, we can identify the incident directions that excite these modes. Then, the coupled current can be maximized at these incident directions and in their close vicinity. By then performing the summation in (2), we can predict the incident excitation that generates the maximum coupled current.

On the other hand, if the angle of incidence of the excitation is known, we can predict the modes that will be excited. Based on their modal significance in Fig. 4.3, we can predict the frequencies where coupled current resonates. For example, consider the case where one is interested in the current coupled to the corner observation location when the plane wave excitation is incident at $\theta = 0°$ and $\phi = 0^{o}$. This direction of incidence can only excite Modes 1, 2, 9, and 10. By examining the current distributions of these modes, shown in Fig. 4.4, one can see that only Modes 1 and Mode 2 have hotspots, shown in red, at the corner observation location. Modes 9 and 10 have minimal current, shown in blue, at this location. We, therefore, expect the total coupled current to show peaks only at the resonance frequencies of Modes 1 and 2, shown to be around 0.17 GHz in Fig. 4.3. Figure 4.7 confirms these predictions by showing the full-wave simulated current at the corner observation location due to a plane wave

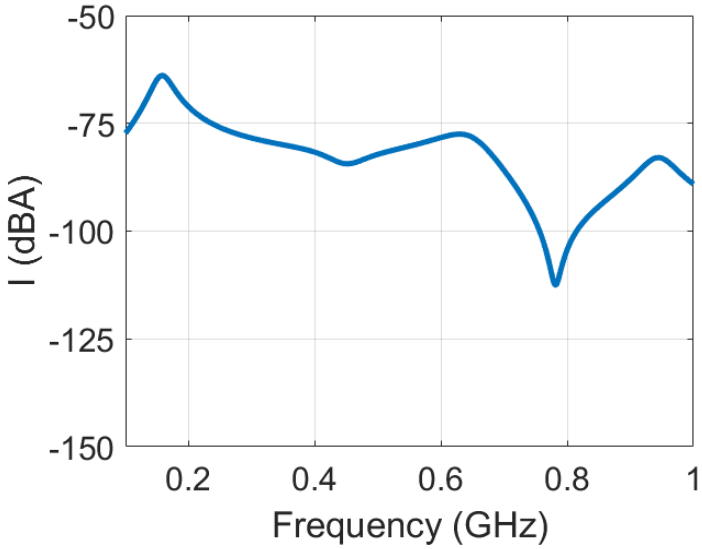

Figure 4.7 Coupled current to the edge of the wire due to an incident wave at θ = 0°.

excitation at θ = 0°. A clear peak is present in the coupled current in Fig. 4.7 near the frequency of 0.17 GHz, which is the same resonance frequency of Modes 1 and 2. Figure 4.7 also shows a strong minimum near 0.77 GHz. This minimum is not due to the absence of current coupling pathways because Modes 9, 10, and 11 are significant at this frequency. The minimum in the coupled current at 0.77 GHz exists because these three modes contribute zero current at the corner observation location. These predictions were achieved from the CMA information generated in Fig. 4.3 to Fig. 4.5. The following section describes how varying the UAV model dimensions can affect previously described modal behavior.

4.5 Sensitivity of Modes to UAV Model Dimensions

In this section, we explore how the modal characteristics vary with the dimensions of the UAV model. Three dimensions of the UAV model in Fig. 4.1a were varied: ℓa (arm' length), ℓb (length of the controller board), and wb (width of the controller board). The effect of varying the UAV's arm length ℓa on the modal behavior for fixed center body dimensions ℓb = wb = 220 mm, is plotted in Fig. 4.8a. For this analysis, the arm length ℓa was increased from 200 mm to 500 mm in 50 mm increments. For each value of ℓa, the modal significance,

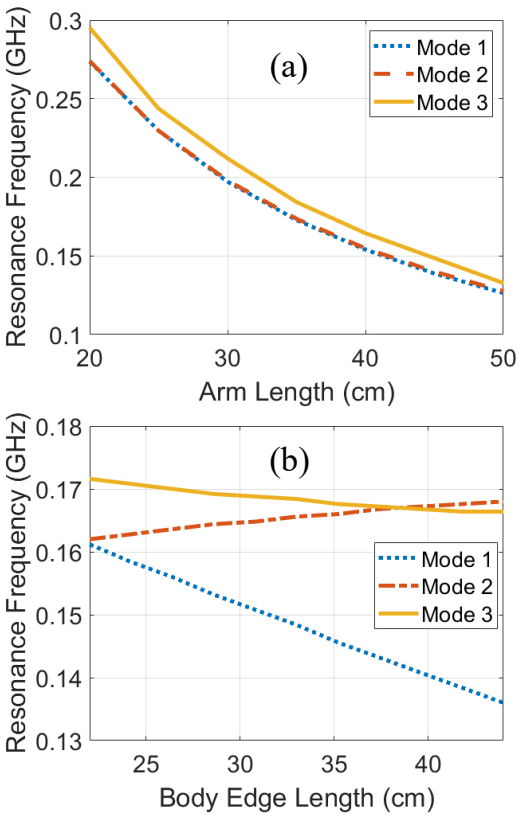

Figure 4.8 The resonance frequencies of the modal significance of Modes 1-3 when (a) the arm length ℓa was varied and (b) when the body length ℓb was varied.

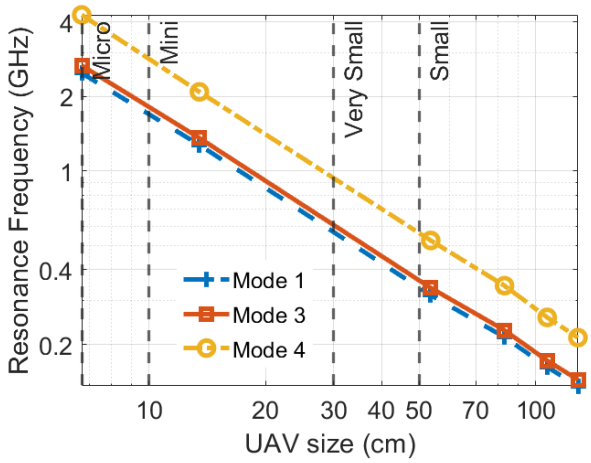

Figure 4.9 The resonance frequencies of the modal significance of Modes 1.3, and 4 when the size of the UAV was varied according to the size of different UAV classes.

MSn, was recalculated (not shown for brevity), and the resonance frequency of MS1 –MS3 was plotted as shown in Fig, 8a. Fig. 4.8a shows that the resonance frequencies of Modes 1-3 decrease proportional to ~ 1/ℓa.

The effect of varying the patch's length, ℓb, for a fixed arm length and patch width, ℓa = 380 mm and wb =220 mm, is shown in Fig. 4.8b. As the body length ℓb increases from 220 mm to 440 mm in 22 mm increments, the center patch becomes a rectangle instead of a square breaking the 4-fold symmetry. Instead of Mode 1 and Mode 2 showing identical resonance frequencies, Fig. 4.8b shows that as ℓb is increased that Mode 1 and Mode 2 start showing opposite trends. That is, the resonance frequency of Mode 1 starts to decrease, and the resonance frequency of Mode 2 starts to increase. The resonance frequency of Mode 1 is the most sensitive to the change in ℓb, decreasing from 0.162 GHz to 0.136 GHz, which corresponds to a 15.5% reduction in the resonance frequency for a 100% increase in ℓb. On the other hand, Mode 2 only shows a 3.5 % increase in its resonance frequency for a 100 % increase ℓb.

The current distribution of the modes shown in Fig. 4.4 explains this behavior because the current distribution of Mode 1 is parallel to ℓb. Still, the current distribution of Mode 2 is parallel to wb. Therefore, increasing ℓb and keeping wb constant marginal affects Mode 2 but significantly affects Mode 1. Mode 3 is a hybrid mode combining the current distributions of Mode 1 and Mode 2, as shown in Fig. 4.4. Its resonance frequency follows approximately the average of the trends of Mode 1 and Mode 2. Since Mode 1 shows a more significant decrease than Mode 2, the overall trend of Mode 3 is to decrease with an increase in ℓb.

The effect of varying the UAV size was also studied. Sadraey *et al.* classified the UAV according to their sizes, where the size is defined as the longest dimension of the UAV [134]. For a quadcopter, then, the size of the UAV is measured from the opposite corner motors. Most commercial off-the-shelf (COTS) UAVs fall within the following four classes: Micro UAVs where the size is less than 10 cm, Mini UAVs where the size is between 10 cm and 30 cm, Very Small UAVs when the size is between 30 cm and 50 cm, and Small UAVs where the size is from 50 cm up to 2 m. Since the model in Fig. 4.1 is classified as a Small UAV, its dimensions were scaled down to cover other UAV classes and to study the effect of the UAV size on the modes of the frame. Figure 4.9 illustrates the variation of the resonance frequencies of Mode 1, Mode 3, and Mode 4 when the overall size of the UAV changes. The analysis of the resonance frequency of Mode 2 is omitted since it is identical to Mode 1 for the symmetric model, as illustrated in the previous section. Figure 4.9 shows that the resonance frequencies of the modes scale up when the size of the UAV scales down in a logarithmic fashion. Thus, the coupling problem studied in this work is invariant with respect to a simultaneous change of the dimensions and frequencies. Therefore, the CMA analysis performed in this work can be scaled based on the size of the UAV frame. Moreover, Fig. 4.9 shows the frequency range

of the first four modes for different UAV size classes. For example, the resonance frequencies of the first four modes of UAVs in the "Mini" class should be confined between 0.6 GHz and 3 GHz if they are similar in shape to the model in Fig. 4.1.

In summary, the advantage of the CMA is that it explicitly delineates the current distribution of the modes. This current distribution will allow us to predict which modes will change their resonance frequencies and which modes will have their resonance frequencies unaffected by a change in the DUT's geometry. The mode resonances are directly related to the coupled current, which is a weighted summation of the modes (2). Moreover, scaling the overall size of the UAV leads to a linear shift in the resonance. Now that the modal characteristics and behavior are fully quantified, the following section shows how CMA can predict the coupled current in experimental measurements.

4.6 Experimental Testing of CMA Predictions

An EMCO 5317 GTEM was used for testing the CMA predictions. The GTEM cell has a maximum septum height of 1.5 m and a recommended frequency range of DC - 18 GHz. The GTEM has a 50 Ω 7/16 DIN coaxial input at its feed. Port 1 of a Rohde & Schwarz ZVA 24 vector network analyzer (VNA) was connected to this feed to generate the incident TEM wave. The GTEM was terminated with pyramidal foam absorbers and distributed resistive loads to prevent any reflections. The UAV model in Fig. 4.1 was built from copper wires and a square copper sheet. It was placed inside the GTEM at a 1.5 m septum height to be excited by the generated TEM fields, as shown in Fig. 4.10. The field strength at the UAV location can be estimated by dividing the input voltage at the TEM-cell port by the septum height. A 225 mV stimulation was applied at port 1 of the GTEM, giving a field strength at the UAV location of ~225/1.5 = 150 mV/m. A BCP-512 clamp-on broadband current probe with an operable

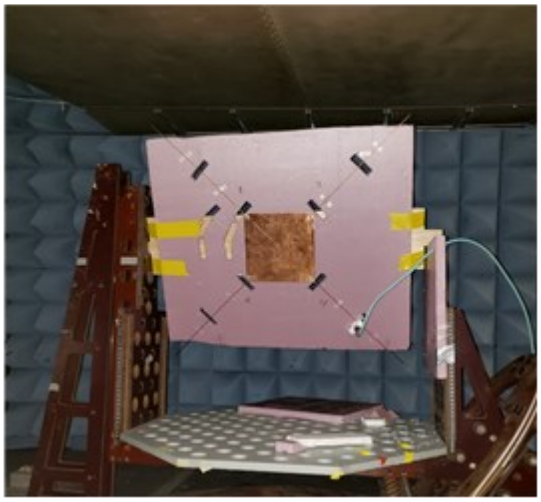

Figure 4.10 Experimental setup showing the realized UAV model inside the GTEM and the current probe at one location.

frequency range of 1 MHz – 1 GHz was placed at different locations on the UAV model to sample the total coupled current. The experimental setup in Fig. 4.10 was used to validate the CMA predictions since the total coupled current is a weighted summation of the modes in Figs. 3-5. The current probe was connected to Port 2 of the VNA. The measured S-parameter, S21, was converted to the coupled current through the following formula [135], [136]:

$$\left|I_{\text{probe}}\right|_{\text{dBA}} = \left|V_G\right|_{\text{dBV}} + \left|s_{21}\right|_{\text{dB}} - \text{cable loss}_{\text{dB}} - \left|Z_T\right|_{dB\Omega} \quad (4)$$

Where V_G is the voltage at the GTEM input port and is calculated based on the required field strength at the location of the UAV. The summation of the V_G and s_{21} yields the voltage received at the current probe. Z_T is the transfer impedance of the probe. Z_T represents the transfer function that converts the voltage readings from the current probe into corresponding current values, as obtained from the datasheet of the current probe [43]. The "Cable Loss" term represents the attenuation the measured signal experiences as it travels from the current probe to the VNA and can be measured experimentally. Z_T and the "Cable Loss" are typically negative when represented in decibels. Therefore, experimental measurements will focus on

the frequencies and incident angles summarized in Table 4.2 since CMA predicts that these frequencies will maximize the coupled current.

In the first experimental measurement, the UAV model was oriented normal to the incident wave inside the GTEM, i.e., at $\theta = 0°$ and $\phi = 0°$ and with the polarization angle at zero. The current probe was placed at the corner location, and the coupled current was measured and compared to the simulations that used incident plane waves with an electric field amplitude of 150 mV/m. Excellent agreement was achieved between the measurements and the simulations, as shown in Fig. 4.11. For both the simulated and the measured current, the peak current was achieved near 0.17 GHz, the resonance frequency of Modes 1 and 2 as shown in Table 4.2.

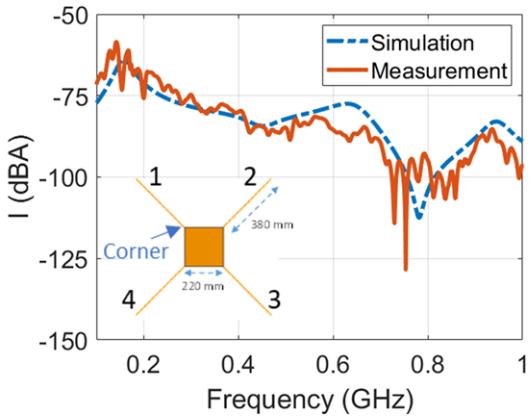

Figure 4.11 Comparison between the measured and simulated currents at the edge of Wire 1 for normal incidence $\theta = 0°$and $\phi = 0°$.

A minimum was experimentally observed in the coupled current near 0.77 GHz, even though this is the resonance frequency of Modes 9 and 10, as shown in Table 4.2. Figure 4.4 shows that these modes' current distributions have a minimum at the corner location. The maximum of their current distribution occurs at the middle location. Therefore, CMA predicts that this dip in the coupled current will disappear if the current probe is moved to the middle of the wire. Figure 4.12 shows the simulated and the measured current at the middle of the wire

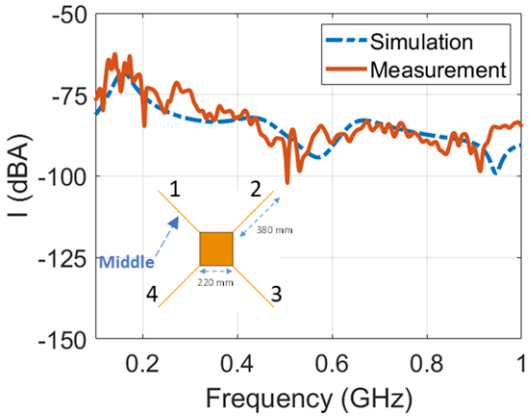

Figure 4.13 Comparison between the measured and simulated currents at the middle of Wire 1 for normal incidence $\theta = 0°$and $\phi = 0°$.

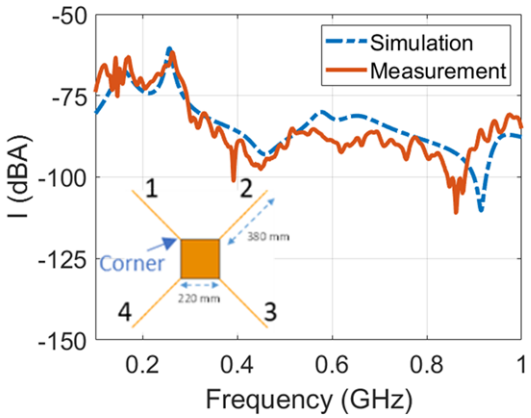

Figure 4.12 Comparison between the measured and simulated currents at the edge of Wire 1 for oblique incidence $\theta = 45°$and $\phi = 0°$.

for the same UAV orientation. The dip in the coupled current near 0.77 GHz is significantly

reduced, validating the CMA prediction. Specifically, in Fig. 4.11, the minimum coupled current was less than -115 dBA, but in Fig. 4.12, it was on the order of ~ - 90 dBA.

To further examine CMA's ability to predict coupled current, we examined Mode 4, which cannot be excited by normal incidence. Figure 4.5 and Table 4.2 show that the optimum angle of exciting Mode 4 is $\theta = 45°$. Therefore, if we change the orientation of the incident wave relative to the UAV model, Mode 4 can be excited. As a result, we expect a new peak to emerge in the coupled current at its resonance frequency of 0.24 GHz, as shown in Fig. 4.3. Figure 4.13 shows the coupled current at the corner location at an oblique incidence angle of $\theta = 45°$ and $\phi = 0°$ and polarization angle of zero. As predicted by CMA, a new peak emerges at 0.24 GHz caused primarily by Mode 4. Therefore, without thousands of trials and errors, CMA provides a straightforward technique to predict the frequencies and angles of incidence where the peaks in the coupled current exist.

4.7 Conclusion

In this work, we developed a simple model for the wires and electronic circuitry of quadcopter Unmanned Aerial Vehicles (UAVs) using a square metallic patch and four wires. Characteristic Mode Analysis (CMA) was successfully applied to calculate the fundamental modes supported by the UAV model and the characteristics of these modes. The knowledge of this modal behavior facilitates the quantification of the UAV's electromagnetic interference and allows one to identify the resonant frequencies that maximize the coupled current. Moreover, we showed that the CMA could predict the orientations that maximize the coupled current to the UAV model at a particular frequency. The CMA predictions were tested experimentally by building the UAV model, exciting it with plane waves inside a GTEM, and measuring the coupled current using a clamp-on current probe. Excellent agreement was

achieved between the simulations and the measurements validating this approach for quantifying electromagnetic coupling and interference to UAVs and similar devices of interest.

Furthermore, the CMA could efficiently predict the incident angles, frequencies, and probe locations where the coupled current to the UAV model will be maximum. Thus CMA could guide the EMC testing of a practical DUT by reducing the number of necessary experimental measurements needed to ensure that maximum coupling is detected. In the future, we will extend the CMA approach employed herein to study more complicated and practical UAV models with a larger number of wires and electronics and by expanding the model from a quasi-3D to a full 3D model.

The only caveat of using CMA for predicting the coupling to complex wire systems will be the increase in computational time. In Chapter 5, this will be optimized by evoking different approaches to handle complex systems.

CHAPTER 5

5 EMC ANALYSIS OF QUADCOPTER UAVS USING EQUIVALENT CIRCUIT APPROACH

5.1 Abstract

Studying the electromagnetic compatibility of an Unmanned Aerial Vehicle (UAV) using full-wave electromagnetic simulations is computationally challenging. RF coupling to a UAV depends on the convoluted properties of its wires and the linear/nonlinear load terminations. In this work, we show how the Equivalent Circuit Approach (ECA) can be used to study RF coupling to the complete wiring system of a quadcopter UAV in a computationally efficient manner. The ECA is based on modeling the direct coupling to the wiring system with a Thevenin equivalent circuit terminated with the load under test. We study different circuit representations for this Thevenin equivalent circuit and show the advantages of each representation. Moreover, the equivalent circuit of the UAV wires can be used to study different linear/nonlinear loads and different waveform excitations in a fraction of the time required by brute force full-wave simulations. In addition to reducing the computational time significantly, we will show how the ECA provides physical insight that can facilitate the prediction of RF coupling to the UAV and similar complex devices.

5.2 Introduction

Unmanned Aerial Vehicles (UAVs) have been proposed for a wide range of applications due to their low cost, easy operation, and high mobility [137]–[143]. Moreover, UAVs have been studied to operate as mobile base stations in remote areas [144], [145]. Therefore, extensive research has been conducted to improve the operation of UAVs in different environments and for different applications [146]–[150]. However, with the increased

demand for UAVs in wireless communication applications, the risk of high electromagnetic interference (EMI) and unintentional coupling to the UAVs increases [151]–[153]. Thus, the requirements for the protection and/or shielding of UAVs increase.

In a relatively complex system such as a UAV, its operation is vital to the accurate execution of its electronic equipment [154]. Therefore, accurate estimation of the coupling to these systems is essential [154]. However, unintentional coupling and interference might be challenging to predict and quantify. Hamdalla *et al.* used Characteristic Mode Analysis (CMA) to guide the experimental characterization of coupling and interference to a simplified UAV model [120], [121], [155]. In addition, the effect of electromagnetic pulses and lightning on a wide variety of vehicles has been previously studied [156]–[159]. However, these studies were conducted for simplified wire distributions, and the reported studies lacked physical insight into the coupling pathways of the DUT.

In this chapter, we study electromagnetic coupling to the complete wiring system of the quadcopter UAV shown in Fig. 5. 1. Sadraey *et al.* classified UAVs according to their sizes, where the size is defined as the longest dimension of the UAV [134]. For a quadcopter, the size of the UAV is measured from the opposite corner motors. In this work, we studied a quadcopter 54 cm in size, which belongs to the class of *small* UAVs. We created a full-wave model of a small UAV system with all its wires and components to be used as a numerical platform for studying the RF coupling. The MakerBot Digitizer Desktop 3D scanner was used to scan the Commercial off-the-Shelf (COTS) quadcopter shown in Fig. 5. 1a. The MakerBot scanner is a desktop 3D scanner with a small turntable where the object to be scanned is placed. It uses laser scanning technology to scan the object. Using the MakerBot Digitizer scanner, we developed an accurate representation of the quadcopter, as illustrated in Fig. 5. 1b.

The effect of the frame is negligible since it is composed of a low permittivity dielectric [107], [119]. Thus, we removed the frame and retained the same wire distribution as shown in Fig. 5. 1c and Fig. 5. 1d, which show two different views of the UAV wiring system. In Fig. 5. 1c and Fig. 5. 1d, the wires' lengths and diameters match the values in the actual scanned UAV, and all the components are represented by blue ports to which an arbitrary impedance can be assigned. In the wiring system, all the wires are assumed to be AWG 18 with 0.5 mm radii. Twenty-four loads were connected to the wiring system to act as a rough representation of the various UAV components/devices. Each of the four arms has five loads to represent the

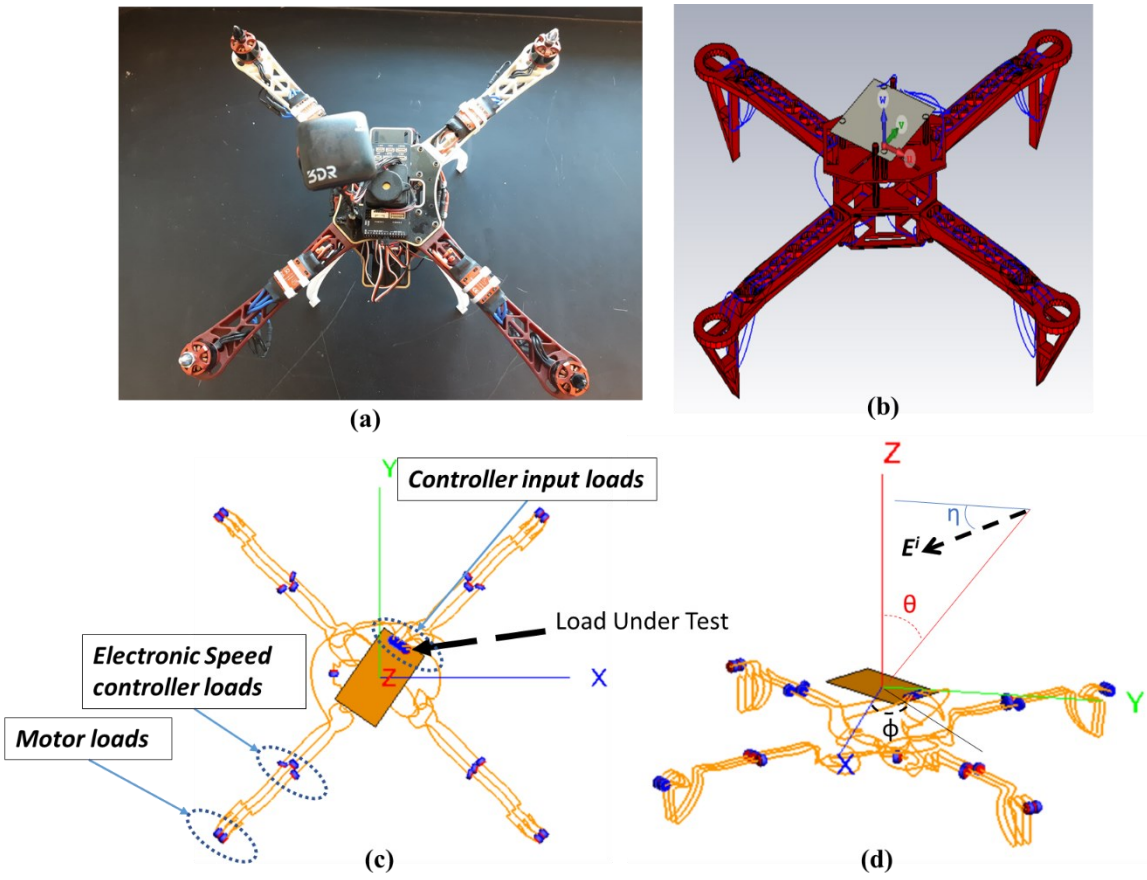

Figure 5.1 (a) UAV picture, (b) UAV quadcopter wiring diagram above a dielectric frame, (c) The top view of the proposed model of the UAV wiring system in (a) and (b), (d) side view of the proposed model of the UAV wiring system.

various electronic devices and the motor located in the arm. Four loads are added at the center of the UAV to represent the input impedance between the pins and the rectangular ground plane of the controller. The controller is assumed to be backed with a rectangular ground plane that is 85 mm × 48.5 mm, as shown in Fig. 5. 1. Without loss of generality, we selected one of the four loads of the controller in Fig. 5. 1c, labeled as the load under test (LUT), and we studied coupling and interference to this load due to a wide range of different excitations. However, the LUT can be varied to be any of the twenty-four loads in the system. Additional loads can be added to the wiring system to better approximate the actual UAV devices. However, the system in Fig. 5. 1 represents a compromise between simplicity and accuracy in representing the UAV.

Simulating a complex configuration similar to the one shown in Fig. 5. 1 is computationally challenging using a full-wave solver. Several prior studies employed the Equivalent Circuit Approach (ECA) as a computationally efficient approach to model electromagnetic coupling to various DUTs. The previously studied DUTs include shielded, unshielded wires, PCB traces, and antennas [64], [72], [73], [75]–[79], [160]. However, most prior studies focused on simple wire and trace configurations. The novelty of this work is that we extend the ECA to a significantly more complex wire distribution than what was studied before. Another contribution is to investigate two different circuit topologies to generate the equivalent circuit of the complex DUT in Fig. 5. 1 and highlight the advantages and disadvantages of each topology. Finally, for the first time, we also show some of the physical insight provided by the ECA and how it can predict electromagnetic coupling.

This chapter is arranged as follows. Section 5.3 provides a summary of the ECA and the two different circuit topologies that can be used to realize it. Section 5.4 presents the Numerical Results, and Section 5.5 summarizes the Conclusions and Future Work.

5.3 Equivalent Circuit Approach (ECA) Theory

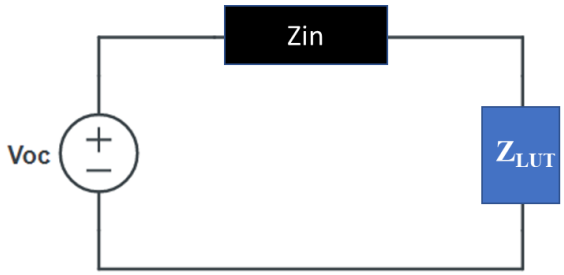

Figure 5.2 Thévenin equivalent circuit of the RF coupling to the UAV LUT.

The Equivalent Circuit Approach (ECA) is based on the fact that any linear wiring system can be treated like a receiving antenna that can be represented by the classical Thévenin circuit shown in Fig. 5. 2 [82], [161]. The Thévenin circuit involves two main components defined at the receiving port of the LUT: (*i*) the open-circuit voltage of the system V_{oc} and (*ii*) the input impedance/admittance (Z_{in}/Y_{in}) of the system as seen at the port where the LUT is connected. It is important to emphasize that V_{oc} and Z_{in} need to be calculated once using a full-wave solver. Once V_{oc} and Z_{in} are calculated, the ECA allows the testing of several load/excitation parameters using a SPICE solver, which is much faster than a full-wave solver. These two parameters will be utilized to study the coupling to the LUT due to various excitations and for different impedances assigned to the LUT, Z_{LUT}.

Using the ECA representation in Fig. 5. 2, we can formulate a transfer function (TF) that calculates the coupled voltage to a linear LUT using the voltage divider rule as follows:

$$TF = V_{oc} * \frac{Z_{load}}{Z_{load}+Z_{in}} \tag{11}$$

For any linear LUT, the TF can be analytically calculated computationally efficiently using (1). Thus, the TF can facilitate the prediction of the frequencies with high/low coupling to the LUT. To highlight this role, we set all the loads of the UAV wire system, except the LUT, to be 1 kΩ. That is, all the blue dots in Fig. 5. 1 are set to be 1 kΩ. This value is chosen to qualitatively agree with the average of the UAV experimental measurements reported in [111]. The UAV is excited by a 100 V/m plane wave. The excitation angle of incidence is chosen to be $\theta = 0^{\circ}$ and $\varphi = 0^{\circ}$, and the polarization angle is chosen to be $\eta = 0^{\circ}$. The input impedance, Z_{in}, and the V_{oc} at the port of the LUT are then simulated using the full-wave solver CST Studio Suite [59].

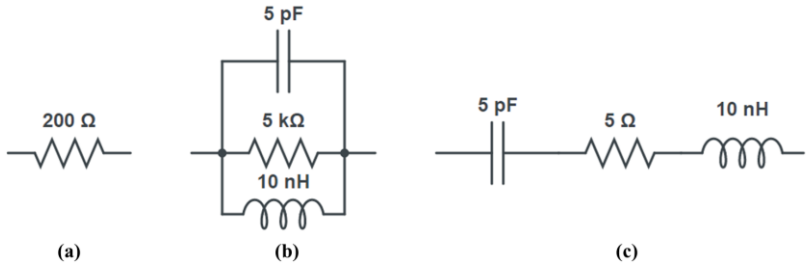

Figure 5.3 Sketch showing the three loads assigned for the LUT (a) Load 1, (b) Load 2, and (c) Load 3.

Three different linear loads are tested for the LUT in Fig. 5. 1c: *load1* is a resistive load where R = 200 Ω, *load2* is a parallel RLC with R = 5 KΩ, L = 10 nH, and C = 5 pF, and *load3* is a series RLC load with R = 5 Ω, L = 10 nH, and C = 5 pF. Fig 3 shows the three loads under test. The TFs for the three linear cases are calculated analytically using (1).

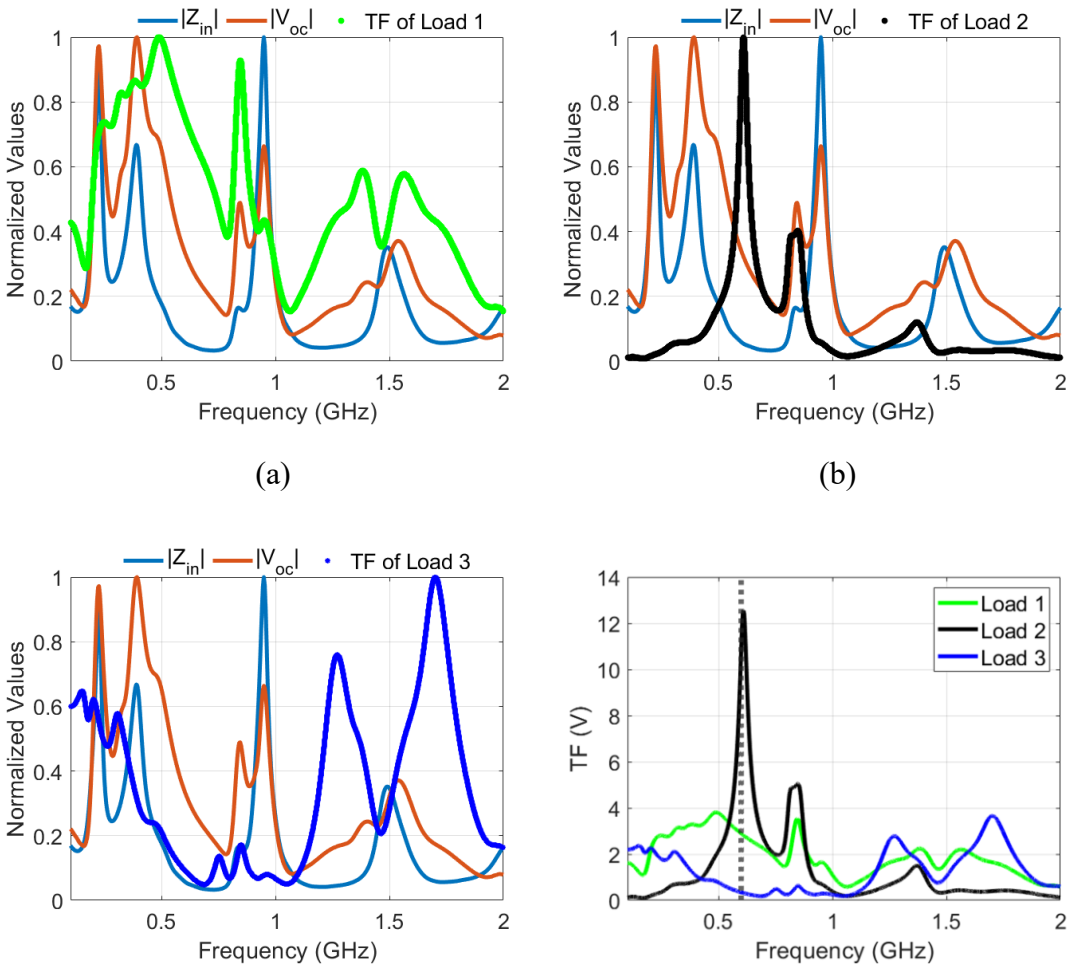

Figure 5.4 The normalized values of the open-circuit voltage (Voc), the input impedance (Zin), and the transfer function (TF) for (a) Load 1, (b) Load 2,(c) Load 3, (d) the TF for three different loads non-normalized.

Fig. 5. 4 shows the normalized Z_{in}, V_{oc}, and the TFs for all loads. The parameters Z_{in} and V_{oc} do not change with the change in the LUT, but the TFs for all three loads show different trends. For example, the TF of *load1*, shown in Fig. 5. 4a, has a maximum value at 0.5 GHz, whereas V_{oc} and Z_{in} do not show a maximum at this frequency. Similarly, the maxima of the TF of *load2 and load3* are at 0.6 GHz and 1.7 GHz, respectively, different from the TF of *load1*. Therefore, predicting the maximum coupling frequencies requires the calculation of the

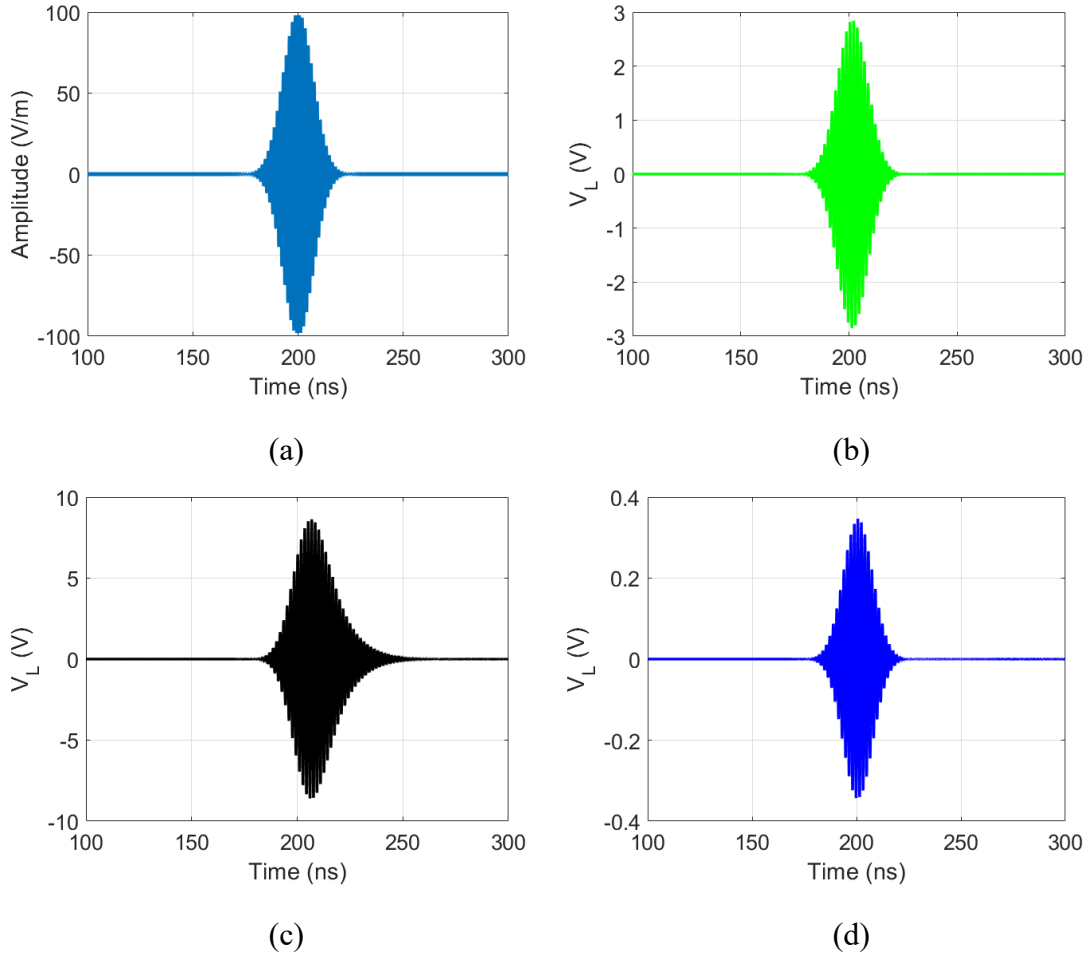

Figure 5.5 (a) The incident electric field of the Gaussian excitation centered around 0.6 GHz, (b) the time domain LUT voltage for load1, (c) the time domain LUT voltage for load2, and (d) the time domain LUT voltage for load3 due to the Gaussian excitation in (a)

TF, which determines how the voltage coupled to the wiring system is partitioned between the wiring system and the LUT.

To highlight the physical insight provided by the ECA, the TFs in Fig. 5. 4 are used to predict the response of the UAV to a time-domain pulsed excitation. The UAV is excited by the Gaussian pulse shown in Fig. 5. 5a. The Gaussian pulse is centered around 0.6 GHz and has a peak amplitude of 100 V/m and a bandwidth of 50 MHz.

Fig. 5. 4d shows the non-normalized values of the TFs of all the three studied loads, which indicates that at 0.6 GHz, the TF of *load2* shows the highest value, followed by *load1* and then *load3*. This behavior is because the impedance of *load2* has the highest magnitude at this frequency, followed by *load1* and then *load3*. Therefore, the TF predicts that if the UAV is excited by a pulse centered at 0.6 GHz, the coupled voltage to the LUT when *load2* is assigned will be the highest while the coupled voltage to *load3* will be the minimum.

To confirm this prediction, we used CST MWS to perform a full-wave simulation of the UAV, and we directly calculated V_{load} for the three loads due to the Gaussian pulsed excitation previously discussed. When *load1, load2, and load3* are assigned to the LUT, Fig. 5. 5a, Fig. 5. 5b, and Fig. 5. 5c show the coupled V_{load} due to the Gaussian pulse excitation, respectively. When *load2* is assigned for the LUT, the coupled V_{load} is higher than the other two loads, as shown by comparing Fig. 5. 5a with Fig. 5. 5b and Fig. 5. 5c. In summary, ECA provides the input impedance of the wires, Z_{in}, and, by comparing its magnitude with the magnitude of Z_{LUT} at the frequencies of interest, we can determine the portion of the coupled voltage that will be dissipated in the wires and the portion that will be passed on to the LUT.

However, the TF cannot be calculated analytically for LUT with nonlinear components. Therefore, a SPICE solver is typically needed to numerically solve the circuit in Fig. 5. 2 and calculate the coupled voltage to the LUT due to different pulsed time-domain excitations [64]. The steps of calculating the coupling to a nonlinear load using the ECA are as follows:

1) Calculate the input impedance seen at the port of the LUT. The input impedance, Z_{in}, should be calculated over the frequency bandwidth of interest using a full-wave electromagnetic solver.

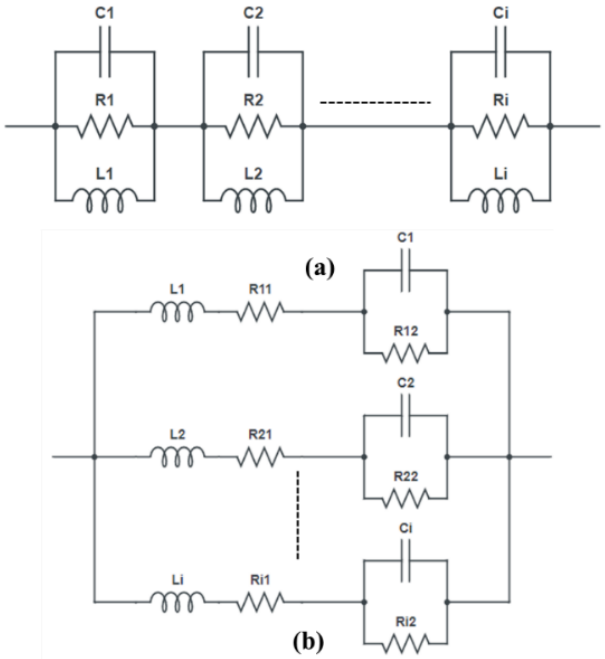

Figure 5.6 Circuit representation of Zin (a) Circuit1 representation (b) Circuit2 representation.

2) Represent the input impedance calculated in the previous step with an equivalent circuit.
3) Use the full-wave electromagnetic solver to calculate the open-circuit voltage at the port of interest versus frequency. This open-circuit voltage will be calculated at a particular incident direction and polarization.
4) Use SPICE simulations to calculate the coupled voltages/currents to the LUT

Voc and Zin parameters need to be calculated only once using a full-wave solver. The calculation of V_{oc} is performed in the frequency domain, over the frequency band of interest, using a constant incident field of amplitude 1 V/m. Once V_{oc} and Z_{in} are calculated, an equivalent circuit similar to Fig. 5. 2 can be realized. Any variations in the impedance of the LUT, Z_{LUT}, can be studied using much faster SPICE simulations, as long as the UAV wiring system does not change. For each different time-domain pulsed excitation, a different time-domain V_{oc} is required in the SPICE simulations. However, instead of re-running the full-wave

solver, postprocessing converts the frequency domain V_{oc} in Fig. 5. 4 to the time domain and convolute it with the excitation pulse to estimate the corresponding time-domain V_{oc} for each time-domain pulsed excitation. The calculation of the time domain V_{oc} requires only a few seconds which is more efficient than re-running the full-wave solver to calculate the time-domain V_{oc} for every different excitation waveform. The following section will show how Z_{in} in Fig. 5. 2 can be represented by different circuit representations in the SPICE simulations.

A. Circuit Topologies for the Z_{in} Representation

The accuracy of the circuit representation of Z_{in} is essential for the SPICE simulations to match the full-wave results. The input impedance can be represented by different circuit topologies [162]. In this work, we studied two circuit topologies for the input impedance representation. The two representations are categorized as (*i*) *Circuit1*: In this circuit representation, each resonance in the input impedance is represented by a parallel RLC branch as shown in Fig. 5. 6a [80] (*ii*) *Circuit2*: In this circuit representation, the input impedance is modeled as a summation of *N* arbitrarily weighted poles. Poles typically exist in conjugate pairs. Each pair can be represented by a Second Series-Equivalent-Circuit (SSEC) branch consisting of an inductor, a capacitor, and two resistors, connected as shown in Fig. 5. 6b [162].

The different components of the two circuit approaches can be calculated as follow:

1) *Circuit 1*: the RLC components' values can be calculated from the input impedance of the system by solving the following two equations [80]:

$$B.W_i = \frac{1}{2\pi R_i C_i} \tag{12}$$

$$f_{r_i} = \frac{1}{\sqrt{L_i C_i}} \tag{13}$$

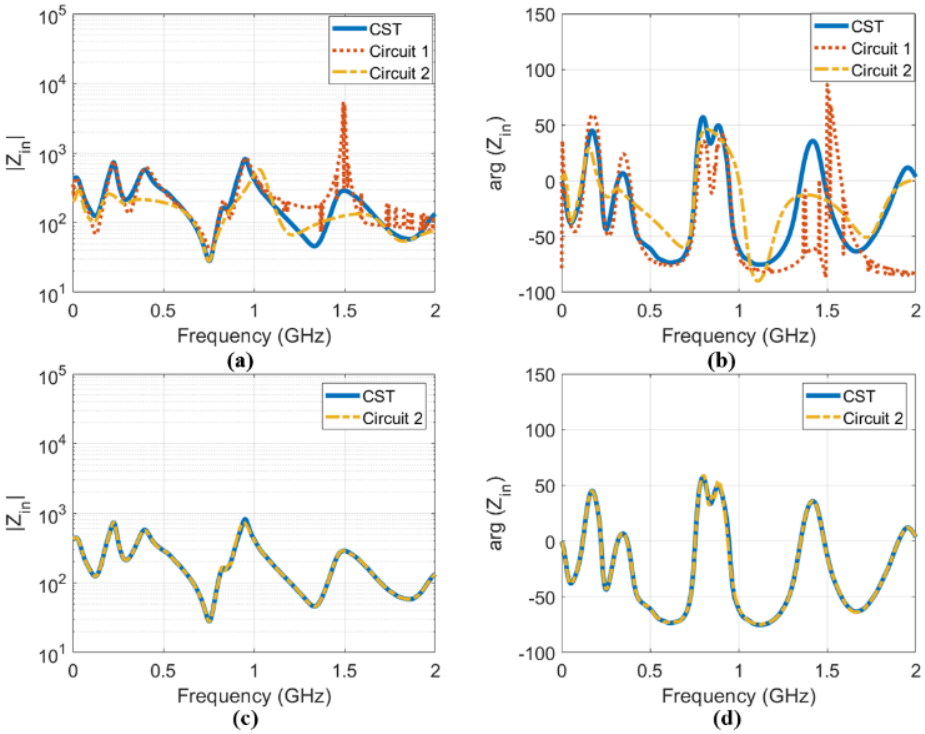

Figure 5.7 Comparison between the full-wave Zin and the Zin calculated using the different circuit representations. (a) the magnitude and (b) phase of Zin calculated using CST MWS, Circuit1 representation, and Circuit2 representation with six branches: (c) magnitude and (d) phase of Z_{in} calculated using CST MWS and *Circuit2* representation with 24 branches.

where f_{r_i} is the resonance frequency of the i^{th} peak of the input impedance response, $B.W_i$ is the bandwidth of the i^{th} peak of the input impedance response, R_i is the peak value of the input impedance at the i^{th} resonance. By solving (2) and (3), the corresponding RLC values of the entire input impedance response can be calculated. Next, the parallel RLC branches can be connected in series, as illustrated in Fig. 5. 6a, to form the overall input impedance representation of the system.

2) *Circuit 2*: Antonini *et al.* and Gustavsen *et al.* showed that any rational function F(s) could be represented as the following summation [162]–[164]:

$$F(s) = \sum_{i=1}^{N} \frac{r_i}{s+p_i} \quad (14)$$

where N is the number of poles, $s = j\omega$ is the complex frequency, r_i and p_i are the residues and poles, respectively. Poles p_i are typically complex and exist in conjugate pairs. A pair of conjugate poles yields a single branch similar to the configuration shown in Fig. 5. 6b. Hence, the number of branches is $M = N/2$. The parameters r_i and p_i can be estimated using the vector fitting technique detailed in [165], [166]. The values of R_{i1}, R_{i2}, L_i, and C_i representation in Fig. 5. 6b can be calculated using the values of r_i and p_i as described in detail in [162]. It is worth mentioning that this method might generate negative impedance values, which can be replaced by an equivalent positive impedance and a parallel current-dependent-current-source (CDCS). That is, Circuit 2 is, in general, more complex than the Circuit 1 representation. However, unlike the representation in Circuit 1, the value of M can be smaller or larger than the number of Z_{in} peaks in the frequency range of interest. Moreover, M can be increased progressively to achieve the desired level of agreement between the Z_{in} calculated using the full wave solver and the Z_{in} calculated using the Circuit 2 representation in Fig. 5. 6b.

5.4 Numerical Simulations of Nonlinear LUT

A. UAV Wiring System Z_{in}

For the UAV wiring system shown in Fig. 5. 1c, Fig. 5. 7a and Fig. 5. 7b show the magnitude and phase, respectively, of Z_{in} at the port of the LUT. Fig. 5. 7a and Fig. 5. 7b show

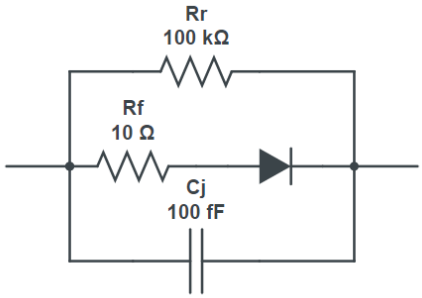

Figure 5.8 Sketch showing the equivalent circuit of the nonlinear Schottky diode assigned to the LUT.

a comparison between the magnitude and phase of Z_{in} calculated using the Full-wave solver, CST MWS [59], and the corresponding values calculated using the two different equivalent circuit representations in Fig. 5. 7. Since there are six peaks in the response shown in Fig. 5. 7a, the *Circuit1* representation will consist of six RLC network branches to represent the full-wave input impedance of the UAV model. For a fair comparison in terms of circuit complexity, we also used six branches for the *Circuit2* representation in Fig. 5. 7a. Fig. 5. 7a illustrates that *Circuit1* agrees better with the full-wave Z_{in} at low frequencies, up to 1 GHz than *Circuit2*. However, in the high-frequency range > 1 GHz, *Circuit1* does not show close agreement with the full-wave response. *Circuit2*, on the other hand, shows considerable deviations from the full-wave Z_{in} over the entire frequency band.

Since the *Circuit2* representation is based on the fitting technique, the value of *M*, the number of branches, can be increased to improve the Z_{in} representation. Increasing *M* increases the complexity of the SPICE simulations, but it is still orders of magnitude faster than the full-

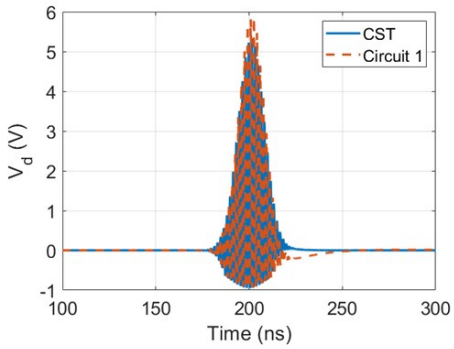

(a)

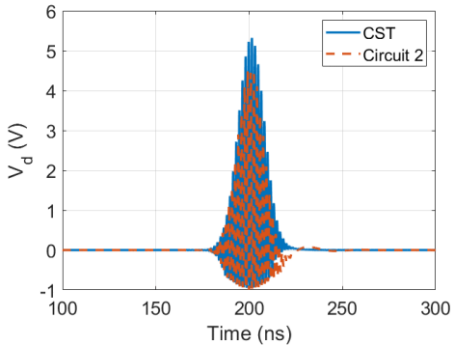

(b)

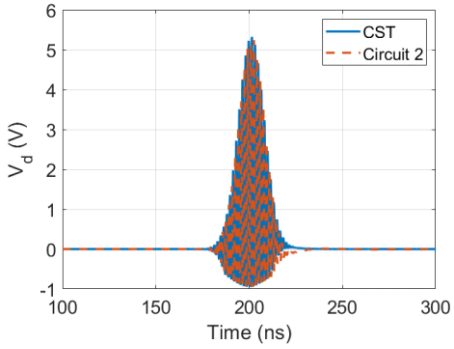

(c)

Figure 5.9 The coupled voltage across the LUT, calculated using the (a) Circuit1 representation, (b) Circuit2 representation with six branches, and (c) Circuit2 representations with 24 branches. In all cases, the UAV was excited by a Gaussian pulse centered around 0.6 GHz with a peak amplitude of 100 V/m and a bandwidth of 50 MHz.

wave solvers. We tested multiple values of M and showed that $M = 24$, which corresponds to

4 branches per resonance, is the smallest value of *M* that yields a maximum error with the full-wave impedance < 9 %. Fig. 5. 7c and Fig. 5. 7d show the comparison between the magnitude and phase of Z_{in} calculated using CST MWS and Circuit 2 with 24 circuit branches connected as shown in Fig. 5. 6b. The response of the improved circuit representation of *Circuit2* closely matches the full-wave Z_{in}. In summary, when the same number of branches are used, Circuit 1 can be better than the Circuit 2 representation, especially at lower frequencies, as illustrated in Fig. 5. 7. However, the Circuit 2 representation is much better than the Circuit 1 representation in agreeing with Z_{in}, especially when the number of circuit branches is increased.

We excited the UAV by a Gaussian pulse centered around 0.6 GHz with a peak amplitude of 100 V/m and a bandwidth of 50 MHz to test the different circuit representations. The excitation angle of incidence is chosen to be $\theta = 0^{\circ}$ and $\varphi = 0^{\circ}$, and the polarization angle is chosen to be $\eta = 0^{\circ}$. A nonlinear Schottky diode, shown in Fig. 5. 8, was assigned to the LUT. The diode has a forward impedance of 10 Ω, a reverse impedance of 100 KΩ, and a 0.1 pF junction capacitance. Fig. 5. 9 shows the load voltage at the LUT calculated using the two circuit representation using LtSpice [167]. Fig. 5. 9 illustrates that using *Circuit1* representation for calculating V_{load} is better than *Circuit2* representation with six branches. The maximum percentage error between V_{load} calculated using the *Circuit1* representation of Z_{in} and V_{load} calculated using CST MWS is 9.91%. However, V_{load} calculated using *Circuit2* representation with six branches has a maximum percentage error of 17.35%. *Therefore, circuit2* representation with 24 branches is also tested, and the maximum percentage error in V_{load} is 3.48 %. Clearly, *Circuit2* representation with 24 branches provides the best representation of the full-wave Z_{in}, as illustrated in Fig. 5. 7, leading to the best estimation of V_{load}. Hence, an accurate representation of Z_{in} of the system is essential.

For further validation, we used the Circuit2 representation with 24 branches to study a rectangular modulated pulse centered around 0.6 GHz with a 50 MHz bandwidth and a peak amplitude of 100 V/m. Fig. 5. 10a shows the time domain V_{oc} for the excitation calculated using both the full-wave solver and the postprocessing technique of converting the frequency-domain V_{oc} into the time-domain using the inverse Fourier transform and convoluting it with the rectangular modulated pulse. Excellent agreement between the full-wave solver and the postprocessing technique is achieved. However, the computational time of the ECA postprocessing technique is orders of magnitude less than the full-wave solver. The calculated time-domain V_{oc} is then used as the source for the equivalent circuit of the UAV in LtSpice, as illustrated in Fig. 5. 2. The Schottky diode, shown in Fig. 5. 8, was also assigned to the LUT. Fig. 5. 10b shows V_{load} calculated using ECA /LtSpice compared to V_{load} calculated using CST MWS. Again, excellent agreement between the full-wave solver and ECA/LtSpice is achieved with less than 4 % error. For the results in Fig. 5. 10b, the full-wave solver required 40 minutes to perform the calculations of $V_{load,}$ whereas the ECA/LtSpice results required only ~1 second. Thus, the ECA technique is computationally efficient in estimating RF coupling to practical DUT with complex wiring systems like a quadcopter UAV.

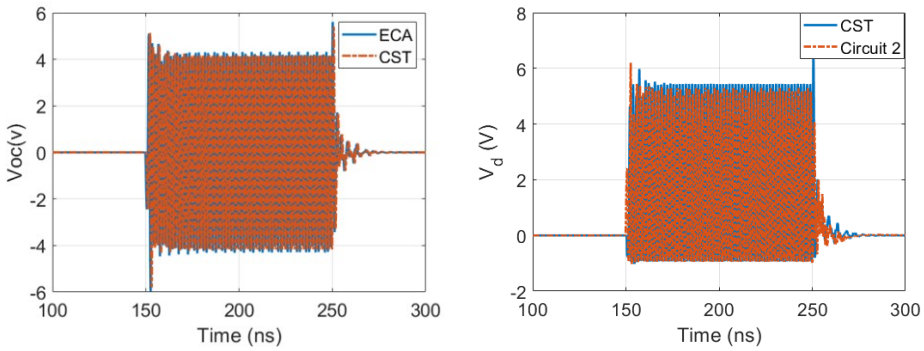

(a) (b)

Figure 5.10 (a) The time-domain open-circuit voltage calculated using the postprocessing technique, and (b) The corresponding coupled voltage to the LUT for a modulated rectangular pulse.

5.5 Conclusion

In this chapter, we developed an accurate model for a quadcopter Unmanned Aerial Vehicle (UAV). The Equivalent Circuit Approach (ECA) was used to study RF coupling to one of the loads of the UAV. The ECA represents the UAV wires by a Thevenin equivalent circuit that can be analytically solved for linear loads or numerically using SPICE simulations for nonlinear loads. Two different circuit representations were tested for generating the equivalent circuit in the SPICE simulations, and the advantages of each representation were highlighted. We showed that the ECA results are within ~4% of the full-wave results with the appropriate circuit representation, but the ECA simulations are orders of magnitude faster. Moreover, the ECA also facilitates the calculation of a Transfer Function (TF), which allows us to predict the optimum waveform characteristics that maximize the coupling to the loads. Future work will extend the ECA to more complex UAV models and other practical devices with complex wiring systems.

CHAPTER 6

6 QUADCOPTER'S FRAME MATERIAL AND SHAPE EFFECT ON ITS ELECTROMAGNETIC COMPATIBILITY, CHARACTERISTIC MODE APPROACH

6.1 Abstract

The variation in the flight conditions of unmanned aerial vehicles (UAVs) affects its electromagnetic compatibility (EMC). That is, the UAV orientation, the flight height, and the speed will determine the coupling mechanism to the UAV. This work will investigate the effect of the UAV's frame material and shape on RF coupling to a UAV. Characteristic mode analysis will be employed to study the fundamental modes that can be supported by a UAV's frame, which facilitate the interpretation of its electromagnetic response and the prediction of its effect on the nearby components. Using CMA analysis, we develop a framework that can optimize the placement of wires and PCBs on the UAV frame mitigating interference from undesired electromagnetic sources. A 3-D scanner is used to provide four different realistic versions of a quadcopter UAV to study the shape effect on the coupling to realistic UAV frames. Different materials are assigned to these frame versions to assist the material effect on the EMCof the UAV. The analysis presented herein can be extended for other DUTs where the wires are placed near a large scatterer similar to the UAV frame.

6.2 Introduction

Unmanned aerial vehicles (UAVs) perform a wide range of civilian and military-related applications [97], [168]–[170]. Recently, researchers have been interested in using UAVs as mobile base stations [171]–[173], which generates a highly congested wireless spectrum flying environment for These UAVs; therefore, they are prone to Electromagnetic Interference (EMI) [174] [175]. Therefore, quantifying the electromagnetic coupling to UAVs is essential.

In previous reports, RF coupling to the receiving antenna of the UAV was studied extensively [176][177]. In [178], low-level direct drive (LLDD) and low-level swept fields (LLSF) methods have been applied to test a UAV with cables to assist the measurements of EM interference. However, the analysis in [178] illustrated that the cavity resonances of the structure, which is a geometry property, play a significant role in the EMC of the UAV cables. Therefore, the contribution of electromagnetic interference to the UAV's frame needs to be considered. On the other hand, quantifying the electromagnetic response of UAVs is complicated by their permutations of shapes, sizes, and material compositions.

In this chapter, characteristic mode analysis will be applied to quantify the EM response of the frame of a quadcopter UAV to predict the locations that will exhibit maximum or minimum coupling for any given incident wave. We will use this information to optimize the placement of the sensors and the placement of the wire systems and electronic systems on the UAV's frame.

CMA has been extensively employed in the design of antennas and the analysis of the electromagnetic scattering characteristics of various nanostructures [112]–[115], [179]. Moreover, CMA has been previously employed for studying the use of the frame of a UAV as an antenna [116], [117], [129]. Recently CMA is applied for 3-D structures such as in [119], [121], [127]–[129], [180]–[182]. Although CMA is mainly applied for antenna design, We recently employed CMA to study coupling and interference to wires and other 2-D structures [118]–[120].

CMA has been extensively applied for scatterers composed of a perfect electric conductor. However, applying CMA for complex shapes composed of lossy conductors or

dielectrics is still under development [183], [184]. Therefore, this chapter applies CMA to quadcopter frames with realistic dielectric materials.

6.3 CMA of UAV Frames

6.3.1 Shape Effect

UAVs are typically composed of many different components, with each component contributing to the overall electromagnetic response to different extents. Modeling the entire UAV with all of its components will lead to a convoluted electromagnetic response. Therefore, it will be hard to isolate the contribution of each component to the overall electromagnetic response. Therefore, we divided the UAV into components and studied each component individually. Since the frame is typically the largest component of the UAV, it will dominate the response at low frequencies. Therefore we focus our work in this paper on studying the electromagnetic response of UAV frames. Perfect Electric Conducting (PEC) material is assigned to the frame since most metals can be modeled as PEC at low frequency. In this work, we focused our analysis on the simple quadcopter UAV shown in Fig. 6.1.

Two identical bars in a cross formation were constructed to construct the UAV frame in Fig. 6.1 (b), and the CMA was performed for this structure. The single bar dimensions are 0.2 m, 0.028 m, and 0.024 m. Fig. 6.2 (b) shows the Modal Significance of the first six modes of the cross-shaped UAV frame, and Fig. 6.2 (b) shows the corresponding Modal currents.

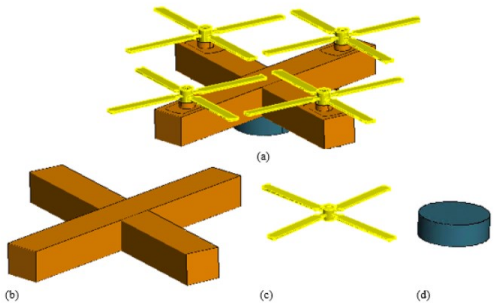

Figure 6.1 (a)Full UAV design, (b) UAV frame, (c) UAV blades, and (d) UAV transmitting and receiving system.

At a particular frequency band, the Modal Significance in Fig. 6.2(a) provides the relative importance of each mode. For example, at 0.6 GHz, Mode 1 and Mode 2 have a significance of 1, whereas all the other modes have a significance below 0.5. This means that up to 0.6 GHz, the response is dominated by Mode 1 and/or Mode 2, depending on the excitation of the modes, and the total current excited on the bar will be very similar to the Mode 1 and/or Mode 2. Beyond a frequency of 0.6 GHz, other modes start to become significant, and the response will be due to a mixture of modes based on the relative importance of each mode at a particular frequency and whether the incident wave excites a particular mode or not.

Mode 1 and Mode 2 have overlapping modal significance, as shown in Fig. 6.2(a), indicating equal significance at every frequency. This overlap arises from the symmetry of the structure and the identical dimensions of the two intersecting bars. Figure 6.2(b) shows the Modal currents of the first six modes. The hot spots, shown in red in Fig. 6.2(b), indicate the areas with the maximum currents, which will be the areas with maximum fields scattered, and the UAV electronic devices near these spots will be more prone to coupling. The blue regions in Fig. 6.2(b) show currents with low magnitudes. To simplify distinguishing between Mode

1 and Mode 2, we keep one bar and slightly modify the other bar to break the symmetry. We have added 1% of a single bar length to the modified bar. The dimensions of one bar are 0.2 m, 0.028 m, and 0.024 m, while the other bar dimensions are 0.202 m, 0.028 m, and 0.024 m. For the nonsymmetric UAV frame, Mode 1 will exhibit significant currents only in the horizontal bar, whereas in Mode 2, only the vertical bar will be significant exhibit currents. Therefore, Mode 1 will be excited if the incident field is parallel to the horizontal bar, Mode 2 will be excited if the incident field is parallel to the vertical bar, and a circularly polarized wave will excite both modes.

Modes 3 is a hybrid combination of Mode 1 and Mode 2, and they resonate at higher frequencies, as shown in the green Modal Significance curve in Fig. 6.2(a). Modes 5 and 6 overlap as their current pattern is similar but rotated by 90°. Because of the overlap in modal current at the joint part of the bars, it is expected that Mode 5 and Mode 6 will have a hybrid Mode at a higher frequency. This behavior was previously reported in similar structures with 4-fold symmetry [132], [133].

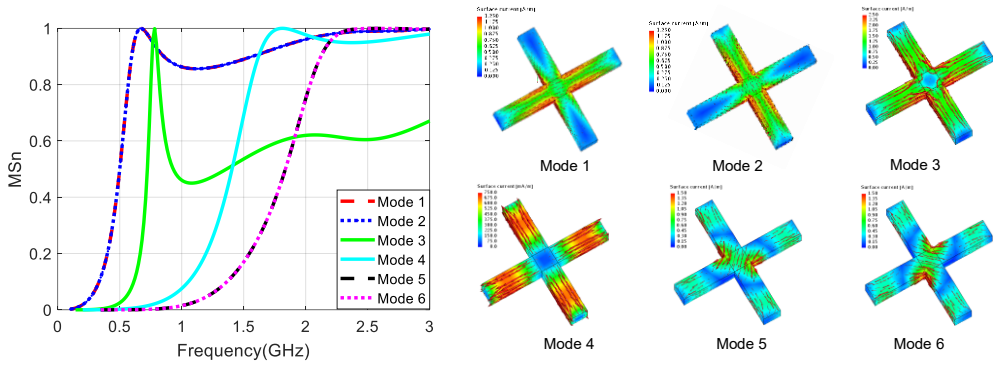

(a) (b)

Figure 6.2 (a). Modal significance of a PEC cross-shaped UAV frame. (b) Fundamental modes of a PEC cross-shaped UAV frame.

6.3.2 Realistic PEC UAV Shapes

Moving on to realistic UAV three-dimensional 3D shapes, we used the MakerBot Digitizer scanner to scan the frame of a quadcopter UAV model. The MakerBot scanner is a desktop 3D scanner with a small turntable where the object to be scanned is placed. It uses laser scanning technology to scan the object. Using the MakerBot Digitizer scanner, we developed four different 3D versions, Version 1-Version 4, of the UAV, with Version 1 being the coarsest, whereas Version 4 is the finest, as shown in Fig. 6.3. That is, Version 4 is the most accurate scanned structure, and it includes most of the features of the actual UAV frame. The single-arm length of the scanned frames is 19.5 cm, and the overall frame size is 51.1×51.1 cm.

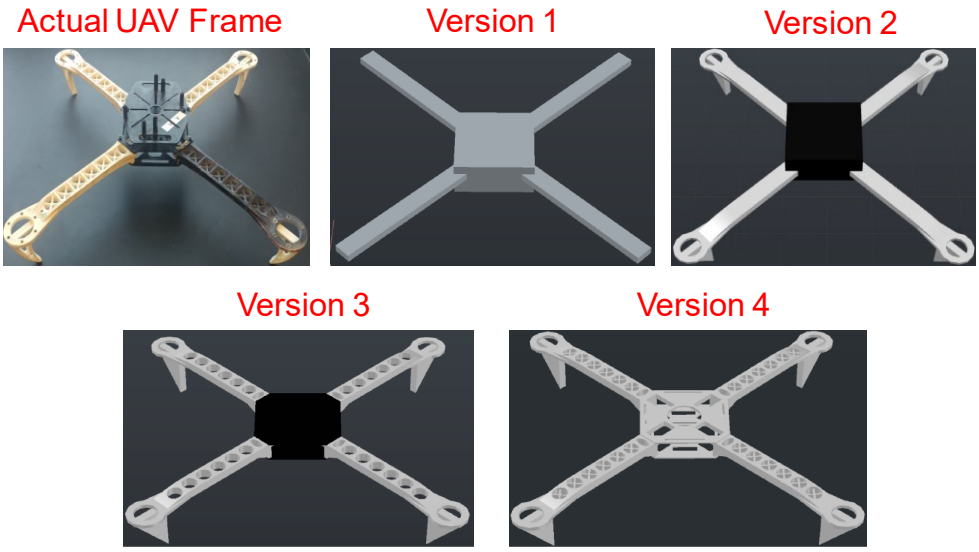

Figure 6.3 The actual frame of the UAV and four different 3D representations of its geometry.

CMA is applied to Version 1 of the frame to identify the resonance frequencies and the corresponding modal currents hot spots of the frame. Figure 6.4 (a) shows the modal significance of the frame. Up to 0.5 GHz, the frame will have three modes, two identical modes

resonate at 0.29 GHz, and Mode 3 resonates at 0.32 GHz. The identical modes are due to the 4-fold symmetry of the UAV cross bars shape studied in the previous section. Figure 6.4 (b) shows the normalized current distribution of the first three modes where the color bar clarifies that the hotspots are near the arms (see the red colors) and not the central square part of the UAV (see the blue color).

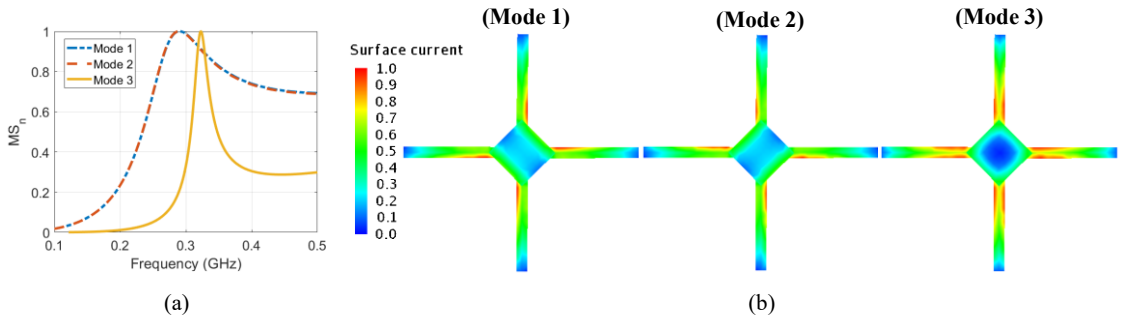

(a) (b)

Figure 6.4 (a) Modal significance of the PEC frame (V1) (b) The normalized current distribution of the first three modes.

To illustrate how the CMA can demonstrate how the relative location can affect the coupling current to the electronics above realistic UAV frames, we studied coupling to three identical wire loops, loop length = 120 mm, loop radius= 0.25 mm, and the loop height = 15 mm, and the loops are mounted at different locations above Version 1 of the UAV as shown in Fig. 6.5(a). The incident electric field is oriented parallel to the three loops, as shown in Fig. 6.5(a). Figure 6.5(b) shows the induced voltage at Load 2. Loop 1 and Loop 3 show higher overall induced voltage than Loop 2 because they are above the "hotspots" of Mode 1, as shown in Fig. 6.4 (b). The induced voltage at Load 2 on Loop 2 is lower than that of Loop 1 and Loop 3 because it is not located near the hotspot of Mode 1, as shown in Fig. 6.4 (b). Thus, the predictions of the coupling sensitivity to the wire location above a complicated structure

can be achieved using CMA. Therefore, we will study the effect of different accurate representations of the UAV by applying CMA to the other three versions of the scanned UAV.

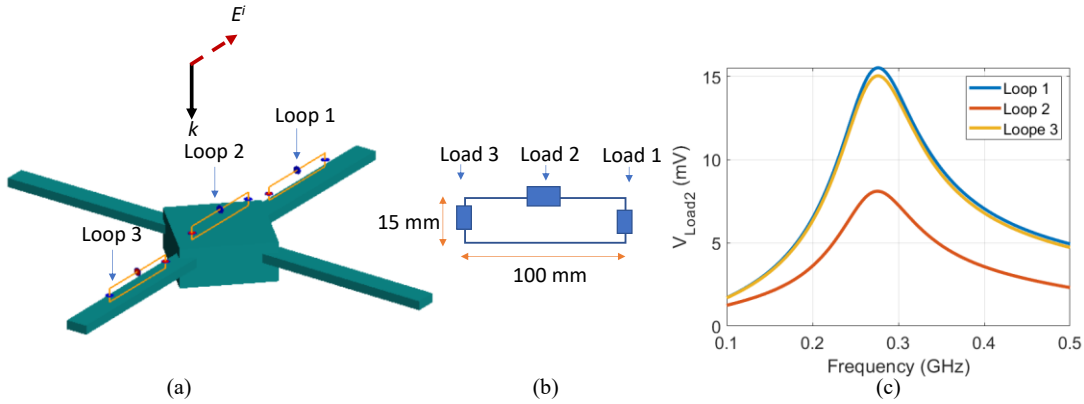

Figure 6.5 (a) Wire loops system above a PEC frame (V1) and the applied electric field orientation (b)sketch of the wire loop and its dimensions (c) Induced voltage on load 2 of different wire loops above the PEC UAV frame.

As a starting point, we will assume that the material assigned to all frames is PEC, while more realistic dielectric properties will be studied next. Figure 6.6 (a) shows the effect of the small features captured by the high-resolution scanned UAV versions on the Modal significance of the first mode, whiles its effect on Mode 3 is shown in Fig. 6.6 (b). The small features captured by high-resolution versions are not significant on the resonance frequencies of the modes as shown in Fig. 6.6 except for version 1 compared to the other versions because version one doesn't have the circular parts used to mount the motors at the end of each arm. Therefore, version 1 is electrically smaller than the other versions. The study of Mode 2 is omitted since Mode 1 and Mode 2 are identical. Due to the geometrical difference, each version will have a different current distribution for the dominant 1st Mode, as shown in Fig. 6.7. The magnitude of the modal current is increasing as we move to the more accurate representation of the UAV. Version 4 shows the highest magnitude of Mode 1 modal current, while the modal

current of Mode 1 of Version 1 has the lowest magnitude. Thus, the geometrical differences between the versions will affect the current distribution of Mode 1, affecting the coupling to wires and electronic chips at different locations above the frame. Three wire-loops are mounted at the same spots above the four different UAV versions to demonstrate this difference. The excitation field direction and the loops' locations are identical to the case in Fig. 6.5(a). Since the magnitude of the modal current of version 4 is the highest, it is expected to reradiate the highest fields to the dipoles, generating high voltages across the dipoles above the hotspots.

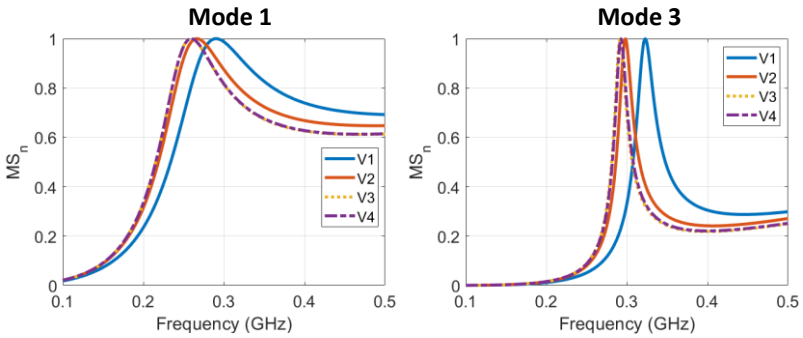

Figure 6.6 Modal significance of the four different 3D representations of the UAV frame. (a) Mode 1,(b)Mode 3

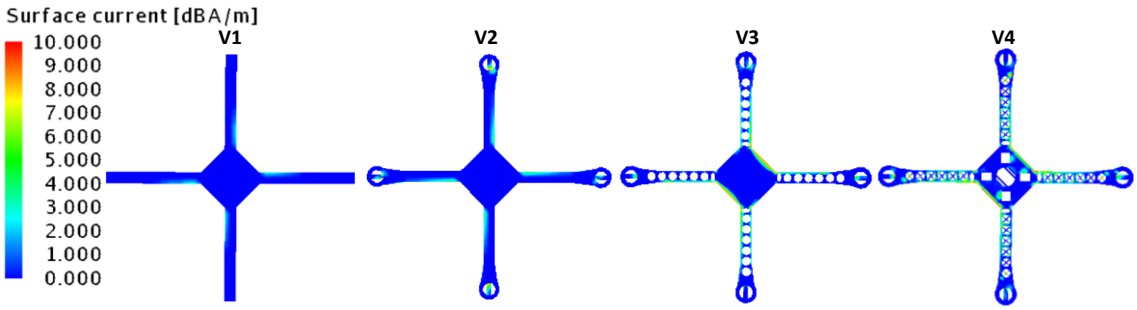

Figure 6.7 Current distribution of Mode 1 for different scanned versions on UAV.

On the other hand, Version 1 has the lowest modal currents. Therefore the induced voltages across the dipoles above the hotspots of the modal currents are expected to be the

lowest compared to the other versions of the UAV frame. Figure 6.8 shows the induced voltage across Load 2 on the loop located above the hotspot of Mode 1 for the four different UAV frame versions.

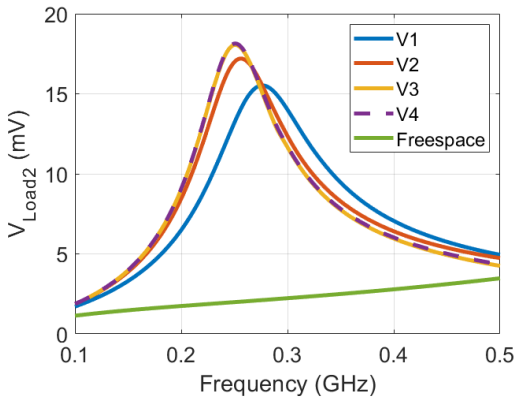

Figure 6.8 Induced voltage at load 2 on loop 1 above the four different 3D representations of the PEC UAV frame compared to the load voltage if the loops are in free space.

Clearly, the induced voltage on the loop that is located above the hotspot of Mode 1 of version 4 is the highest, while the induced voltage on the loop located above the same spot on version 1 is the lowest. Due to the slight differences between Version 3 and Version 4, the induced voltage on the loop above both versions shows a similar magnitude. The induced voltage on the loops above the PEC frames is compared to the induced voltage of the same loop configuration in free space. That is, the frame is completely removed. The comparison in Fig. 6.8 illustrates that the induced voltage at the loops will only occur at the resonance frequency of the frame, and no peak will arise on the induced voltage of the loops in free space.

The analysis provided in this section illustrates the significance of small UAV frame' features on the location optimization of the wires and electronics. It also illustrates the ability of CMA to optimize the location of the wires and electronics to maximize/minimize the coupling and interference.

It is worth emphasizing that the modal currents and modal significance are excitation independent. Thus, all the predictions performed in this section don't need stochastic analysis for location optimization, which proves the computational efficiency of the CMA compared to traditional computational techniques. In the next section, realistic material will be assigned to the scanned versions of the frame.

6.4 UAV Material Effect

This section performed CMA to the first two representations of the scanned UAV model in Fig. 6.3. Still, we changed their material properties to match common UAV frame plastics materials ($\varepsilon_r \approx 3.3$). The Modal Significance of the two versions is shown in Fig. 6.9. The Modal Significance of both versions is identical. In contrast, Version 2 has extra pieces at the arms of the UAV, which illustrates that the response of the dielectric UAV frame is less sensitive to the physical features of the arms.

The Modal currents distribution of both versions of the UAV is shown in Fig. 6.10. The current distribution of the modes is concentrated at the central part of the frame, not at the arms. Therefore, changing the length/width of the arm will have a minor contribution to the overall electrical path of the modal currents. This behavior is entirely the opposite case of the conducting frames, where we showed that the central part of the frame would have a minor contribution to mode behavior.

Similar to our previous discussions about the mode hybridization phenomena, the modal currents of Mode 2 and Mode 3 are identical, but Mode 3 is rotated by 90˚ around the axis of UAV in comparison to Mode 2. Mode 4 is a hybrid combination of Mode 2 and Mode

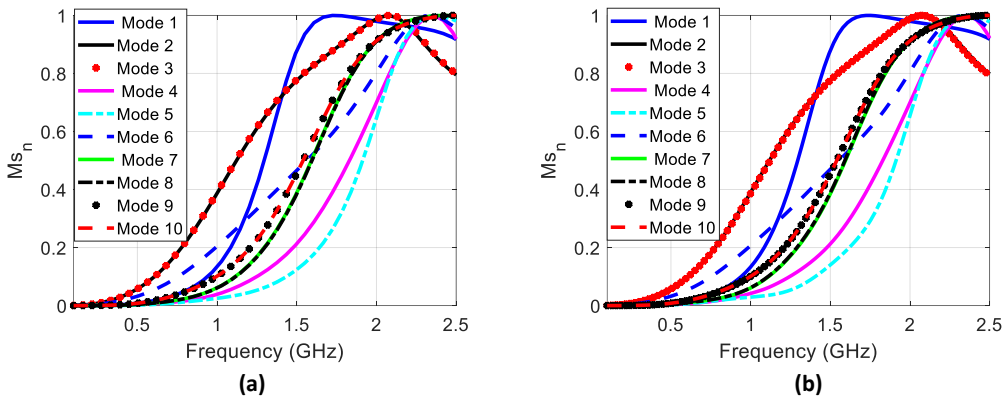

Figure 6.9 Modal significance of a dielectric UAV frame (a) The 1st version (b) The 2nd version.

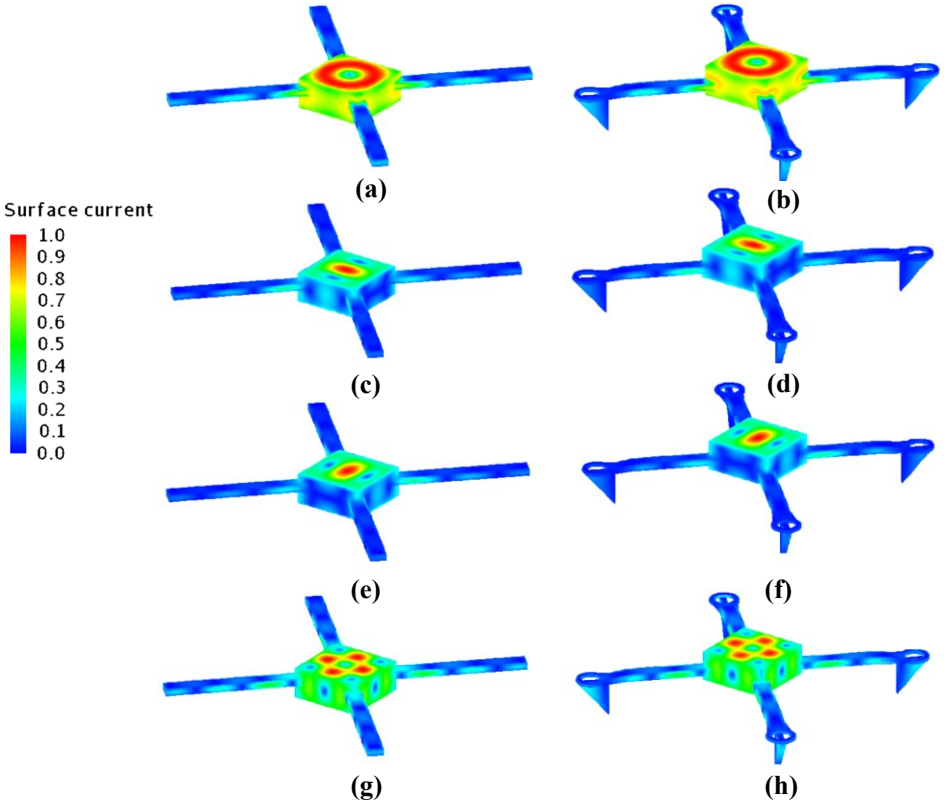

Figure 6.10 Current distribution of (a) Mode 1, (c) Mode 2, (e) Mode 3 , (g) Mode 4 for the 1st version of the dielectric UAV frame. (b) Mode 1, (d) Mode 2, (f) Mode 3 , (h) Mode 4 for the 2nd version of the dielectric UAV frame.

3. As shown in Fig. 6.9 and Fig. 6.10, it is clear that if the electronic devices are mounted on the central part of the UAV, it will be affected when any mode is excited. Therefore, any wires

on the central part of the UAV may be prone to coupling and interference.

To demonstrate how the relative location of the electronic devices can affect their EMC, we studied coupling to wire loop in three cases. The loop is mounted above Version 1 of the UAV with a 3 mm separation in the first case. Secondly, the loop is in free space, and thirdly the loop is placed 3 mm away from an infinite planar dielectric slab. The relative permittivity of the slab is similar to that of the UAV frame, i.e., $\varepsilon_r \approx 3.3$, and its thickness is similar to the frame's center part thickness, i.e., 45 mm. The incident electric field is oriented to excite Mode 2 of the frame and parallel to the loop, as shown in Fig. 6.11(a). Figure 6.11(c) shows the induced voltage at load 2 of the loop in the three studied cases. The peak in the induced voltage of all the loops at 1.4 GHz corresponds to the resonance frequency of Mode 1 of the loop itself. Clearly, the relative permittivity of the frame/layer is responsible for the

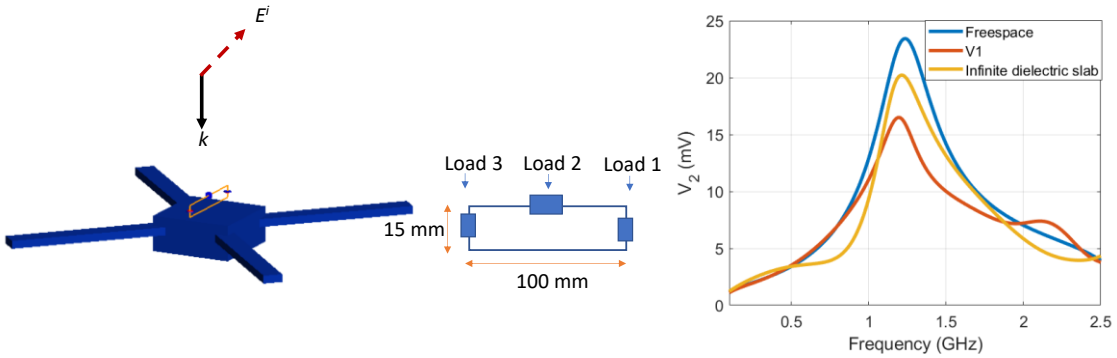

(a) (b) (c)

Figure 6.11 (a) loop above a dielectric frame (V1) and the applied electric field orientation (b) sketch of the wire loop and its dimensions (c) Induced voltage on load 2 at the loop in free space, above of V1 of the UAV frame, and above an infinite planar dielectric slab.

degradation in the coupling at 1.4 GHz. It is also responsible for the reduction in the bandwidth of the peak. Although the induced voltage on Load 2 for the loop in free space and above the

infinite dielectric slab has no peak around 2.2 GHz, Load 2 of the loop above the UAV has the highest induced voltage, which corresponds to the modes of the frame as illustrated in Fig. 6.9.

Another advantage of the CMA is that it explicitly delineates the current distribution of the modes. This current distribution will allow us to predict which modes will change their resonance frequencies and which modes will have their resonance frequencies unaffected with a change in the UAV's geometry. This can facilitate simplifying yet maintaining an accurate representation of the frame. To illustrate how to employ CMA to save the computational time of simulating the frame with different electronic components, we simplified the frame to be computationally efficient for the EM analysis. The frame's arms are removed, and only the body (where the modal currents are concentrated) is kept. CMA for both frame representations, shown in Fig.12, is performed. The two representations are assumed to have the same realistic dielectric properties as the common UAV frame plastics ($\varepsilon_r \approx 3.3$). The Modal Significance of the two representations is shown in Fig. 6.13. The Modal Significance of both representations is identical. The computational time of the CMA for the complete frame with arms is 38.9 hours, whereas the computational time of the CMA for the simplified frame is 6.7 hours. This analysis shows that the knowledge of the modal behavior can be used to simplify the computational complexity of the problem. The following Section describes how varying the UAV frame dimensions can affect previously described modal behavior.

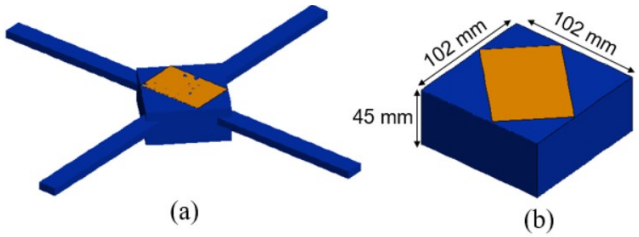

Figure 6.12 (a) The 1st version (b) Simplified representation of the dielectric UAV.

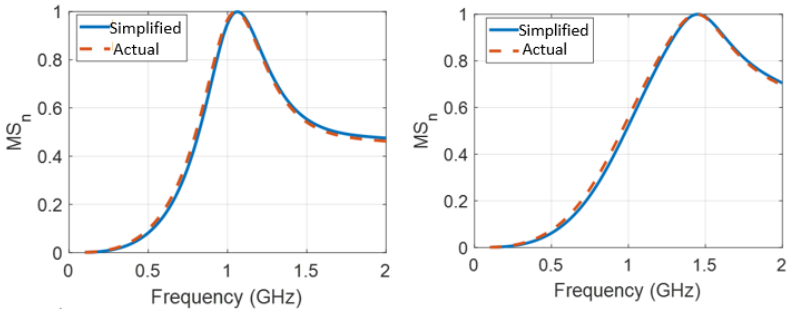

Figure 6.13 The modal significance of 1st version versus the simplified representation of the dielectric UAV (a) Mode 1 (b) Mode 2.

6.5 Sensitivity of Modes to UAV Model Dimensions and Material

The dimensions of a UAV can vary in different models. Therefore, in this Section, we explore how the modal characteristics vary with the dimensions and material of the UAV frame. Two dimensions of the UAV frame in Fig. 6.14(a) are varied: ℓ_a and ℓ_b. The effect of varying the UAV's arm length ℓ_a on the modal behavior for fixed center body dimension ℓ_b = 100 mm, is plotted in Fig. 6.14(b). For this analysis, the arm length ℓ_a is increased from 500 mm to 1000 mm in 100 mm increments. For each ℓ_a value, we recalculated the modal significance, MS, of the first mode, and we plotted the resonance frequency of MS1 in Fig, 14(b) (black line). The analysis in Fig. 6.14(b) (black line) shows that the resonance frequency

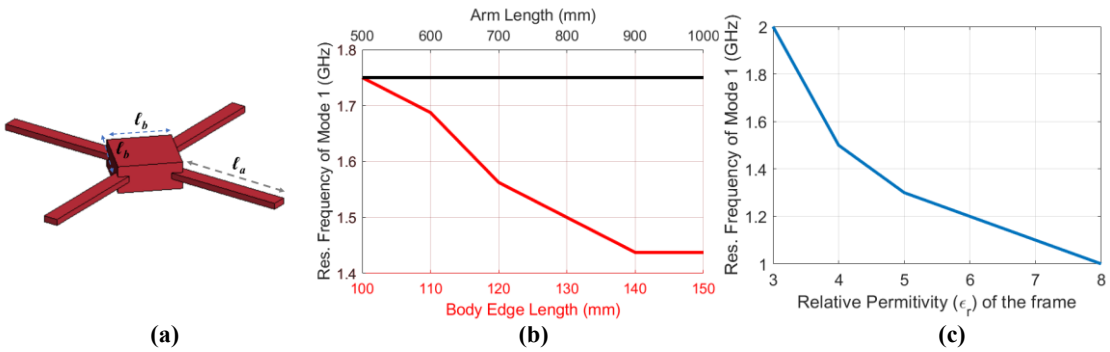

Figure 6.14 (a) A sketch of the quadcopter UAV showing the general dimensions of the structure, (b) The resonance frequencies of the modal significance of Mode 1 when the arm length and ℓa body length ℓb were varied (c) when the relative permittivity of the frame was changed

of Modes 1 is insensitive to the variation on the frame' arm since the current distribution of the first modes is concentrated at the body, not the arms as explained in the previous section.

The effect of varying the length of the center body, ℓ_b, for a fixed arm length, ℓ_a = 500 mm, is shown in Fig. 6.14(b) (red line). As the body length ℓ_b increases from 100 mm to 150 mm in 10 mm increments, the resonance frequency of Mode 1 decreases. The resonance frequency of Mode 1 is sensitive to the change in ℓ_b, decreasing from 1.75 GHz to 1.44 GHz, which corresponds to a 20% reduction in the resonance frequency for a 50% increase in the ℓ_b.

The effect of the frame material on the resonance frequency of the modes is plotted in Fig. 6.14(c). For this analysis, the arm length ℓ_a = 500, the body length ℓ_b = 100 mm, and the relative permittivity of the frame is varied from 3 to 8 in increments of unity. The resonance frequency of Mode 1 decreases from 2 GHz to 1 GHz, which corresponds to a 50% reduction in the resonance frequency for a 166% increase in the relative permittivity of the frame ε_r. The resonance frequency of the modes will decrease as the relative permittivity increases until it approaches the case of the PEC studied in the previous section.

6.6 Conclusion

In this work, we study how the frames of Unmanned Aerial Vehicles (UAVs), which in many cases are manufactured from low-loss dielectrics, can affect coupling and interference to the mounted wires and PCBs. Characteristic Mode Analysis (CMA) is evoked to calculate fundamental modes of different UAV frames and identify the locations on the UAV's frame where the modes will exhibit maximum or minimum effective currents. Using the CMA analysis, we develop a framework that can optimize the placement of sensitive wires and PCBs on the frame mitigating interference from undesired electromagnetic sources. Moreover, we can reduce the complexity of the complete UAV frames, which optimizes the computational time, by studying the modal current locations over the frame. In the future, we will extend the CMA approach employed herein to study more complicated and practical UAV models.

CHAPTER 7

7 CONCLUSION AND FUTURE RESEARCH

7.1 Conclusion

In Chapter 2, CMA was applied as an efficient method that provides a physical insight to determine field-to-wire coupling for simple wire shapes. We found that curved wires can couple to external EM field more than straight wires, with a narrower bandwidth and at slightly higher resonance frequencies.

In Chapter 3, Three different simple wire configurations were studied computationally and experimentally to prove the validity of the Characteristic Mode Analysis (CMA) in the EMC applications. CMA was applied to identify all the modes of the structures and the possible ways to maximize/minimize coupling to each mode. Moreover, the experimental validation example previously discussed validates the versatility of CMA for predicting coupling to simple wire systems.

In Chapter 4, we developed a simple model for the wires and electronic circuitry of quadcopter UAVs using a square metallic patch and four wires. CMA was successfully applied to calculate the fundamental modes supported by the UAV model and the characteristics of these modes. The knowledge of this modal behavior facilitates the quantification of the UAV's EMC to external interference and allows us to identify the resonance frequencies that maximize the coupled current. Besides, we showed that the CMA could predict the orientations that maximize the coupled current to the UAV model at a particular frequency. The CMA predictions were tested experimentally by building the UAV model, exciting it by plane waves inside a GTEM, and measuring the coupled current using a clamp-on current probe. Excellent agreement was achieved between the simulations and the measurements validating this

approach for quantifying electromagnetic coupling and interference to UAVs and similar devices of interest.

In Chapter 5, we developed an accurate model for a quadcopter Unmanned Aerial Vehicle (UAV). The Equivalent Circuit Approach (ECA) was used to study RF coupling to one of the loads of the UAV. The ECA represents the UAV wires by a Thevenin equivalent circuit that can be analytically solved for linear loads or numerically using SPICE simulations for nonlinear loads. Two different circuit representations were tested for generating the equivalent circuit in the SPICE simulations, and the advantages of each representation were highlighted. We showed that the ECA results are within ~4% of the full-wave results with the appropriate circuit representation, but the ECA simulations are orders of magnitude faster. Moreover, the ECA also facilitates the calculation of a Transfer Function (TF), which allows us to predict the optimum waveform characteristics that maximize the coupling to the loads. Future work will extend the ECA to more complex UAV models and other practical devices with complex wiring systems.

In Chapter 6, we studied how the frames of the UAV can affect coupling and interference to the mounted wires and PCBs. CMA was evoked to calculate the fundamental modes of different UAV frames and identify the UAV's frame locations where the modes will exhibit maximum or minimum effective currents. Using the CMA analysis, we develop a framework that can optimize the placement of wires on the frame mitigating interference from undesired electromagnetic sources. Moreover, we can reduce the complexity of the complete UAV frames, which optimizes the computational time, by studying the modal current locations over the frame. In the future, we will extend the CMA approach employed herein to study more complicated and practical UAV models.

7.2 Future Work

This work focused on predicting and quantifying RF coupling to quadcopter UAV models of various levels of complexity. However, additional details can be progressively added to the quadcopter UAV model to be more realistic. Also, the techniques and the guidelines developed herein can be extended to study RF coupling to a plethora of devices in complex environments. Therefore, the following sections provide some insight into suggested future work.

7.2.1 Update the UAV Model

The future plan includes updating the UAV model presented in the previous chapters to include a more accurate representation of the electronic components of the UAV. The ECA can then be used to study the updated UAV model. The UAV model updates include integrating the 3-phase representation of the motor instead of the two loads representation in the current UAV model. It also includes adding the parasitics and inter-wire connections to better model the UAV components, as illustrated in Fig. 7.1. Moreover, we only studied quadcopter UAVs in this work. However, a wide range of UAV configurations exists for various applications. These include fixed-wing, singe-rotor, and vertical take-off and landing (VTOL) UAVs. These different UAV configurations can also be studied using the ECA, and their RF coupling behavior contrasted.

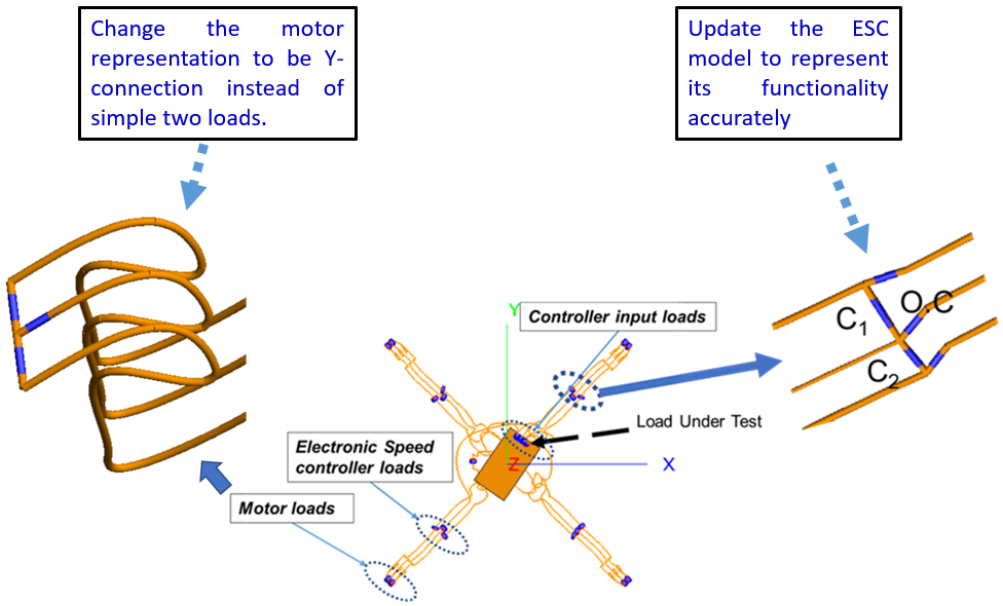

Figure 7.1 A sketch of the quadcopter UAV showing the proposed updated model of the UAV wiring system with the updated electronic components.

7.2.2 RF Coupling to Printed Circuit Boards

The UAV model studied represented the central UAV controller as a rectangular metallic sheet. However, the realistic configuration of the PCB traces will have a significant effect on the coupling. Therefore, studying RF coupling to different PCB configurations using the ECA is a necessary extension of this work. On the other hand, studying complex PCB configurations might be computationally expensive. Therefore, defining the factors, such as the nearby traces and loads, that significantly affect the coupling to PCBs is also a candidate for this work extension. Defining these factors can be done by simplifying the complex configuration and progressively increasing the complexity.

7.2.3 Prepare a Computationally Efficient Software Package

The dissertation illustrates that CMA can predict the optimum field direction to excite a wiring system. Moreover, ECA can be employed to estimate the time-domain response of the system in a computationally efficient manner. Multiple in-house programs were developed in this work over multiple years. Therefore, a proposed extension of this work is to prepare a software package that integrates all of these programs, augments them with a user-friendly Graphical User Interface (GUI), and distribute it to users to quantify RF coupling to various devices. The software package can also predict the optimum pulse parameters, resonance frequency, bandwidth, and pulse repetition frequency to maximize the coupled voltage to a system of wires with linear or nonlinear loads attached.

The package will also study the coupling and interference due to near-field sources. However, due to the uncertainty of the source parameters and the measurement environment, Machine learning algorithms can be integrated with the package to account for the uncertainty.

REFERENCES

[1] "High-intensity radiated fields (hirf) protection for aircraft electrical and electronic systems," *Federal Register*, Feb. 01, 2006. https://www.federalregister.gov/documents/2006/02/01/06-895/high-intensity-radiated-fields-hirf-protection-for-aircraft-electrical-and-electronic-systems

[2] "High-intensity radiated fields (hirf) protection for aircraft electrical and electronic systems," *Federal Register*, Aug. 06, 2007. https://www.federalregister.gov/documents/2007/08/06/E7-15195/high-intensity-radiated-fields-hirf-protection-for-aircraft-electrical-and-electronic-systems

[3] "Ac 20-158a - the certification of aircraft electrical and electronic systems for operation in the high-intensity radiated fields (hirf) environment – document information." https://www.faa.gov/regulations_policies/advisory_circulars/index.cfm/go/document.information/documentid/1024526

[4] K.-A. Lee, J. Rhee, Y.-M. Cho, J.-E. Baek, and K.-C. Ko, "Damage prediction of rf system affected by electromagnetic pulse," in *2013 19th IEEE Pulsed Power Conference (PPC)*, Jun. 2013, pp. 1–6. doi: 10.1109/PPC.2013.6627531.

[5] R. Olivier, P. Marchand, and S. Chenu, "On the use of electromagnetic simulation in front door radiofrequency interference," in *2017 International Conference on Military Communications and Information Systems (ICMCIS)*, May 2017, pp. 1–5. doi: 10.1109/ICMCIS.2017.7956492.

[6] S. van de Beek, R. Vogt-Ardatjew, and F. Leferink, "Intentional electromagnetic interference through saturation of the RF front end," in *2015 Asia-Pacific Symposium on Electromagnetic Compatibility (APEMC)*, May 2015, pp. 132–135. doi: 10.1109/APEMC.2015.7175304.

[7] T. X. Nguyen, S. V. Koppen, J. J. Ely, G. N. Szatkowski, J. Mielnik, and M. T. Salud, "Small aircraft rf interference path loss," in *2007 IEEE International Symposium on Electromagnetic Compatibility*, Jul. 2007, pp. 1–6. doi: 10.1109/ISEMC.2007.27.

[8] M. G. Backstrom and K. G. Lovstrand, "Susceptibility of electronic systems to high-power microwaves: summary of test experience," *IEEE Trans. Electromagn. Compat.*, vol. 46, no. 3, pp. 396–403, Aug. 2004, doi: 10.1109/TEMC.2004.831814.

[9] M. Ritchie, F. Fioranelli, H. Griffiths, and B. Torvik, "Micro-drone rcs analysis," in *2015 IEEE Radar Conference*, Oct. 2015, pp. 452–456. doi: 10.1109/RadarConf.2015.7411926.

[10] G. Spadacini, T. Liang, F. Grassi, and S. A. Pignari, "Worst case and statistics of waveforms involved in wideband intentional electromagnetic attacks," *IEEE Trans. Electromagn. Compat.*, vol. 60, no. 5, pp. 1436–1444, Oct. 2018, doi: 10.1109/TEMC.2017.2778017.

[11] T. Liang and Y. -z Xie, "Maximizing radiated high-power electromagnetic threat to transmission line system under the constraints of bounded bandwidth and amplitude," *IEEE Trans. Electromagn. Compat.*, pp. 1–8, 2020, doi: 10.1109/TEMC.2020.3040271.

[12] S. T. Op 't Land, M. Ramdani, R. Perdriau, M. Leone, and M. Drissi, "Simple, taylor-based worst-case model for field-to-line coupling," *Prog. Electromagn. Res.*, vol. 140, pp. 297–311, 2013, doi: 10.2528/PIER13041207.

[13] C. R. Paul, *Analysis of multiconductor transmission lines*. John Wiley & Sons, 2008.

[14] C. Taylor, R. Satterwhite, and C. Harrison, "The response of a terminated two-wire transmission line excited by a nonuniform electromagnetic field," *IEEE Trans. Antennas Propag.*, vol. 13, no. 6, pp. 987–989, Nov. 1965, doi: 10.1109/TAP.1965.1138574.
[15] A. K. Agrawal, H. J. Price, and S. H. Gurbaxani, "Transient response of multiconductor transmission lines excited by a nonuniform electromagnetic field," *IEEE Trans. Electromagn. Compat.*, vol. EMC-22, no. 2, pp. 119–129, May 1980, doi: 10.1109/TEMC.1980.303824.
[16] F. Rachidi, "Formulation of the field-to-transmission line coupling equations in terms of magnetic excitation field," *IEEE Trans. Electromagn. Compat.*, vol. 35, no. 3, pp. 404–407, Aug. 1993, doi: 10.1109/15.277316.
[17] F. Rachidi, "A review of field-to-transmission line coupling models with special emphasis to lightning-induced voltages on overhead lines," *IEEE Trans. Electromagn. Compat.*, vol. 54, no. 4, pp. 898–911, Aug. 2012, doi: 10.1109/TEMC.2011.2181519.
[18] S. Tkatchenko, F. Rachidi, and M. Ianoz, "Electromagnetic field coupling to a line of finite length: theory and fast iterative solutions in frequency and time domains," *IEEE Trans. Electromagn. Compat.*, vol. 37, no. 4, pp. 509–518, Nov. 1995, doi: 10.1109/15.477335.
[19] C. A. Nucci and F. Rachidi, "On the contribution of the electromagnetic field components in field-to-transmission line interaction," *IEEE Trans. Electromagn. Compat.*, vol. 37, no. 4, pp. 505–508, Nov. 1995, doi: 10.1109/15.477334.
[20] F. Rachidi, C. A. Nucci, and M. Ianoz, "Transient analysis of multiconductor lines above a lossy ground," *IEEE Trans. Power Deliv.*, vol. 14, no. 1, pp. 294–302, Jan. 1999, doi: 10.1109/61.736741.
[21] "0350.pdf." Accessed: Sep. 18, 2021. [Online]. Available: http://ece-research.unm.edu/summa/notes/In/0350.pdf
[22] F. M. Tesche, "On the analysis of a transmission line with nonlinear terminations using the time-dependent BLT equation," *IEEE Trans. Electromagn. Compat.*, vol. 49, no. 2, pp. 427–433, May 2007, doi: 10.1109/TEMC.2007.897141.
[23] Y. Lee, J.-G. Lee, J. So, C. Cheon, Y. Chung, and T. K. Sarkar, "Solution of time-domain BLT equations using laguerre polynomials," in *2007 IEEE Antennas and Propagation Society International Symposium*, Jun. 2007, pp. 793–796. doi: 10.1109/APS.2007.4395613.
[24] F. M. Tesche, "Development and use of the blt equation in the time domain as applied to a coaxial cable," *IEEE Trans. Electromagn. Compat.*, vol. 49, no. 1, pp. 3–11, Feb. 2007, doi: 10.1109/TEMC.2006.888184.
[25] F. M. Tesche and C. M. Butler, "On the addition of em field propagation and coupling effects in the blt equation. revision," CLEMSON UNIV SC DEPT OF ELECTRICAL AND COMPUTER ENGINEERING, Jun. 2004. Accessed: Sep. 18, 2021. [Online]. Available: https://apps.dtic.mil/sti/citations/ADA509645
[26] "0511.pdf." Accessed: Sep. 18, 2021. [Online]. Available: http://ece-research.unm.edu/summa/notes/In/0511.pdf
[27] D. Poljak and K. El Khamlichi Drissi, "Electromagnetic field coupling to overhead wire configurations: antenna model versus transmission line approach," *International Journal of Antennas and Propagation*, 2012. https://www.hindawi.com/journals/ijap/2012/730145/ (accessed Jan. 09, 2019).

[28] J. Nitsch and S. Tkachenko, “High-frequency multiconductor transmission-line theory,” *Found. Phys.*, vol. 40, no. 9, pp. 1231–1252, Oct. 2010, doi: 10.1007/s10701-010-9443-1.
[29] J. B. Nitsch and S. V. Tkachenko, “Complex-valued transmission-line parameters and their relation to the radiation resistance,” *IEEE Trans. Electromagn. Compat.*, vol. 46, no. 3, pp. 477–487, Aug. 2004, doi: 10.1109/TEMC.2004.831905.
[30] A. G. Chiariello, A. Maffucci, G. Miano, F. Villone, and W. Zamboni, “A transmission-line model for full-wave analysis of mixed-mode propagation,” *IEEE Trans. Adv. Packag.*, vol. 31, no. 2, pp. 275–284, May 2008, doi: 10.1109/TADVP.2008.920373.
[31] V. Cooray, F. Rachidi, and M. Rubinstein, “Formulation of the field-to-transmission line coupling equations in terms of scalar and vector potentials,” *IEEE Trans. Electromagn. Compat.*, vol. 59, no. 5, pp. 1586–1591, Oct. 2017, doi: 10.1109/TEMC.2017.2657891.
[32] G. Lugrin, S. V. Tkachenko, F. Rachidi, M. Rubinstein, and R. Cherkaoui, “High-frequency electromagnetic coupling to multiconductor transmission lines of finite length,” *IEEE Trans. Electromagn. Compat.*, vol. 57, no. 6, pp. 1714–1723, Dec. 2015, doi: 10.1109/TEMC.2015.2475156.
[33] A. Vukicevic, F. Rachidi, M. Rubinstein, and S. V. Tkachenko, “On the evaluation of antenna-mode currents along transmission lines,” *IEEE Trans. Electromagn. Compat.*, vol. 48, no. 4, pp. 693–700, Nov. 2006, doi: 10.1109/TEMC.2006.884511.
[34] A. Maffucci, G. Miano, and F. Villone, “An enhanced transmission line model for conducting wires,” *IEEE Trans. Electromagn. Compat.*, vol. 46, no. 4, pp. 512–528, Nov. 2004, doi: 10.1109/TEMC.2004.837685.
[35] Y. Wang, Y. S. Cao, D. Liu, R. W. Kautz, N. Altunyurt, and J. Fan, “A generalized multiple-scattering method for modeling a cable harness with ground connections to a nearby metal surface,” *IEEE Trans. Electromagn. Compat.*, vol. 61, no. 1, pp. 261–270, Feb. 2019, doi: 10.1109/TEMC.2018.2806320.
[36] Y. Wang *et al.*, “Evaluating field interactions between multiple wires and the nearby surface enabled by a generalized MTL approach,” *IEEE Trans. Electromagn. Compat.*, vol. 60, no. 4, pp. 971–980, Aug. 2018, doi: 10.1109/TEMC.2017.2756899.
[37] F. Middelstaedt, S. V. Tkachenko, R. Rambousky, and R. Vick, “High-frequency electromagnetic field coupling to a long, finite wire with vertical risers above ground,” *IEEE Trans. Electromagn. Compat.*, vol. 58, no. 4, pp. 1169–1175, Aug. 2016, doi: 10.1109/TEMC.2016.2544110.
[38] S. Chabane, P. Besnier, and M. Klingler, “A modified enhanced transmission line theory applied to multiconductor transmission lines,” *IEEE Trans. Electromagn. Compat.*, vol. 59, no. 2, pp. 518–528, Apr. 2017, doi: 10.1109/TEMC.2016.2611672.
[39] Y. Wang, Y. S. Cao, D. Liu, R. W. Kautz, N. Altunyurt, and J. Fan, “Evaluating the crosstalk current and the total radiated power of a bent cable harness using the generalized mtl method,” *IEEE Trans. Electromagn. Compat.*, vol. 62, no. 4, pp. 1256–1265, Aug. 2020, doi: 10.1109/TEMC.2019.2927222.
[40] T. J. Cui and W. C. Chew, “A full-wave model of wire structures with arbitrary cross sections,” *IEEE Trans. Electromagn. Compat.*, vol. 45, no. 4, pp. 626–635, Nov. 2003, doi: 10.1109/TEMC.2003.819062.
[41] T. J. Cui, W. C. Chew, J.-S. Zhao, and H.-Y. Chao, “Full-wave analysis of complicated transmission-line circuits using wire models,” *IEEE Trans. Antennas Propag.*, vol. 50, no. 10, pp. 1350–1360, Oct. 2002, doi: 10.1109/TAP.2002.801374.

[42] T. J. Cui and W. C. Chew, “Accurate analysis of wire structures from very-low frequency to microwave frequency,” *IEEE Trans. Antennas Propag.*, vol. 50, no. 3, pp. 301–307, Mar. 2002, doi: 10.1109/8.999620.
[43] T. J. Cui and W. C. Chew, “Accurate model of arbitrary wire antennas in free space, above or inside ground,” *IEEE Trans. Antennas Propag.*, vol. 48, no. 4, pp. 482–493, Apr. 2000, doi: 10.1109/8.843661.
[44] J. C. Pincenti and P. L. E. Uslenghi, “Incident field excitation of random cables,” *Radio Sci.*, vol. 42, no. 6, 2007, doi: 10.1029/2007RS003662.
[45] X. Liu, F. Grassi, G. Spadacini, and S. A. Pignari, “Physically based modeling of hand-assembled wire bundles for accurate emc prediction,” *IEEE Trans. Electromagn. Compat.*, vol. 62, no. 3, pp. 914–922, Jun. 2020, doi: 10.1109/TEMC.2019.2922455.
[46] G. Spadacini, F. Grassi, and S. A. Pignari, “Field-to-wire coupling model for the common mode in random bundles of twisted-wire pairs,” *IEEE Trans. Electromagn. Compat.*, vol. 57, no. 5, pp. 1246–1254, Oct. 2015, doi: 10.1109/TEMC.2015.2414356.
[47] S. A. Pignari, G. Spadacini, and F. Grassi, “Modeling field-to-wire coupling in random bundles of wires,” *IEEE Electromagn. Compat. Mag.*, vol. 6, no. 3, pp. 85–90, 2017, doi: 10.1109/MEMC.0.8093845.
[48] Y. Sun, J. Wang, W. Song, and R. Xue, “Frequency domain analysis of lossy and non-uniform twisted wire pair,” *IEEE Access*, vol. 7, pp. 52640–52649, 2019, doi: 10.1109/ACCESS.2019.2912220.
[49] X. Liu, F. Grassi, G. Spadacini, and S. A. Pignari, “Accurate geometrical modeling and field-to-wire coupling prediction in wiring-structures with loops,” in *2021 XXXIVth General Assembly and Scientific Symposium of the International Union of Radio Science (URSI GASS)*, Aug. 2021, pp. 1–4. doi: 10.23919/URSIGASS51995.2021.9560490.
[50] X. Liu, F. Grassi, G. Spadacini, and S. A. Pignari, “Toward a more realistic characterization of hand-assembled wire bundles: geometrical modeling and emc prediction,” *IEEE Access*, vol. 9, pp. 129502–129511, 2021, doi: 10.1109/ACCESS.2021.3113767.
[51] F. Grassi, H. Abdollahi, G. Spadacini, S. A. Pignari, and P. Pelissou, “Radiated immunity test involving crosstalk and enforcing equivalence with field-to-wire coupling,” *IEEE Trans. Electromagn. Compat.*, vol. 58, no. 1, pp. 66–74, Feb. 2016, doi: 10.1109/TEMC.2015.2503599.
[52] A. Tatematsu, F. Rachidi, and M. Rubinstein, “A technique for calculating voltages induced on twisted-wire pairs using the FDTD method,” *IEEE Trans. Electromagn. Compat.*, vol. 59, no. 1, pp. 301–304, Feb. 2017, doi: 10.1109/TEMC.2016.2604463.
[53] Y. Yan, L. Meng, X. Liu, T. Jiang, J. Chen, and G. Zhang, “An FDTD method for the transient terminal response of twisted-wire pairs illuminated by an external electromagnetic field,” *IEEE Trans. Electromagn. Compat.*, vol. 60, no. 2, pp. 435–443, Apr. 2018, doi: 10.1109/TEMC.2017.2729662.
[54] G. P. Veropoulos, P. J. Papakanellos, and C. Vlachos, “A probabilistic approach for the susceptibility assessment of a straight pcb trace excited by random plane-wave fields,” *IEEE Trans. Electromagn. Compat.*, vol. 60, no. 1, pp. 258–265, Feb. 2018, doi: 10.1109/TEMC.2017.2704911.
[55] C. Yang, W. Yan, Y. Zhao, Y. Chen, C. Zhu, and Z. Zhu, “Analysis on RLCG parameter matrix extraction for multi-core twisted cable based on back propagation neural network

algorithm," *IEEE Access*, vol. 7, pp. 126315–126322, 2019, doi: 10.1109/ACCESS.2019.2935467.
[56] B. Xiao, J. Zhou, X. Liu, W. Yan, Y. Cao, and Y. Zhao, "Crosstalk prediction in twisted-wire pairs based on beetle swarm optimization algorithm," *IEEE Access*, vol. 9, pp. 84588–84595, 2021, doi: 10.1109/ACCESS.2021.3088285.
[57] C. Huang, Y. Zhao, W. Yan, Q. Liu, and J. Zhou, "A new method for predicting crosstalk of random cable bundle based on bas-bp neural network algorithm," *IEEE Access*, vol. 8, pp. 20224–20232, 2020, doi: 10.1109/ACCESS.2020.2969221.
[58] "Simulation for connectivity, compatibility, and radar | altair feko." https://www.altair.com/feko/
[59] "CST studio suite 3d em simulation and analysis software." https://www.3ds.com/products-services/simulia/products/cst-studio-suite/
[60] S. Lee and M. Hayakawa, "A study on the radiation loss from a bent transmission line," *IEEE Trans. Electromagn. Compat.*, vol. 43, no. 4, pp. 618–621, Nov. 2001, doi: 10.1109/15.974642.
[61] J. Kasper, M. Magdowski, and R. Vick, "Comparison of the field-to-wire coupling to bent and curved transmission lines in reverberation chambers," in *2018 International Symposium on Electromagnetic Compatibility (EMC EUROPE)*, Aug. 2018, pp. 713–718. doi: 10.1109/EMCEurope.2018.8485080.
[62] J. Kasper and R. Vick, "Experiment investigation of radiation losses of bent transmission lines in reverberation chambers," in *2018 IEEE Radio and Antenna Days of the Indian Ocean (RADIO)*, Oct. 2018, pp. 1–2. doi: 10.23919/RADIO.2018.8572309.
[63] J. Kasper and R. Vick, "Numerical investigation of the stochastic field-to-wire coupling to transmission lines with small bend angles," in *2019 ESA Workshop on Aerospace EMC (Aerospace EMC)*, May 2019, pp. 1–5. doi: 10.23919/AeroEMC.2019.8788925.
[64] R. Michels, M. Kreitlow, A. Bausen, C. Dietrich, and F. Gronwald, "Modeling and verification of a parasitic nonlinear energy storage effect due to high-power electromagnetic excitation," *IEEE Trans. Electromagn. Compat.*, vol. 62, no. 6, pp. 2468–2475, Dec. 2020, doi: 10.1109/TEMC.2020.2980976.
[65] Z. Wen and Q. Wu, "Time domain characteristic mode theory for transmission and coupling problems," in *2018 IEEE International Conference on Computational Electromagnetics (ICCEM)*, Mar. 2018, pp. 1–3. doi: 10.1109/COMPEM.2018.8496458.
[66] Q. Wu and Z. Wen, "Time domain characteristic mode analysis for transmission problems," *IEEE Open J. Antennas Propag.*, vol. 1, pp. 339–349, 2020, doi: 10.1109/OJAP.2020.3008292.
[67] S. Hemmady, T. M. Antonsen, E. Ott, and S. M. Anlage, "Statistical prediction and measurement of induced voltages on components within complicated enclosures: a wave-chaotic approach," *IEEE Trans. Electromagn. Compat.*, vol. 54, no. 4, pp. 758–771, Aug. 2012, doi: 10.1109/TEMC.2011.2177270.
[68] G. Gradoni, J.-H. Yeh, B. Xiao, T. M. Antonsen, S. M. Anlage, and E. Ott, "Predicting the statistics of wave transport through chaotic cavities by the random coupling model: a review and recent progress," *Wave Motion*, vol. 51, no. 4, pp. 606–621, Jun. 2014, doi: 10.1016/j.wavemoti.2014.02.003.
[69] S. Huang, J. Pan, C. Wang, Y. Luo, and D. Yang, "Unified implementation and cross-validation of the integral equation-based formulations for the characteristic modes of

dielectric bodies," *IEEE Access*, vol. 8, pp. 5655–5666, 2020, doi: 10.1109/ACCESS.2019.2963278.
[70] R. Harrington and J. Mautz, "Theory of characteristic modes for conducting bodies," *IEEE Trans. Antennas Propag.*, vol. 19, no. 5, pp. 622–628, Sep. 1971, doi: 10.1109/TAP.1971.1139999.
[71] Y. Chang and R. Harrington, "A surface formulation for characteristic modes of material bodies," *IEEE Trans. Antennas Propag.*, vol. 25, no. 6, pp. 789–795, Nov. 1977, doi: 10.1109/TAP.1977.1141685.
[72] G. Antonini and A. Orlandi, "Spice equivalent circuit of a two-parallel-wires shielded cable for evaluation of the rf induced voltages at the terminations," *IEEE Trans. Electromagn. Compat.*, vol. 46, no. 2, pp. 189–198, May 2004, doi: 10.1109/TEMC.2004.826887.
[73] X. Gao and Z. Du, "Spice models of a multi-antenna system for transmitting and receiving," *IET Circuits Devices Syst.*, vol. 10, no. 3, pp. 229–236, 2016, doi: 10.1049/iet-cds.2015.0208.
[74] "Spice models for radiated and conducted susceptibility analyses of multiconductor shielded cables." https://www.jpier.org/PIER/view/10020506/ (accessed Sep. 30, 2021).
[75] D. Zhang, Y. Wen, J. Zhang, J. Xiao, D. Liu, and G. Xin, "Coupling analysis for shielded cables in the train using hybrid method," *IEEE Access*, vol. 7, pp. 76022–76029, 2019, doi: 10.1109/ACCESS.2019.2920943.
[76] M. Raya and R. Vick, "Network model of shielded cables for the analysis of conducted immunity and emissions," *IEEE Trans. Electromagn. Compat.*, vol. 61, no. 4, pp. 1167–1174, Aug. 2019, doi: 10.1109/TEMC.2018.2883384.
[77] Q. Jin, W. Sheng, C. Gao, and Y. Han, "Internal and external transmission line transfer matrix and near-field radiation of braided coaxial cables," *IEEE Trans. Electromagn. Compat.*, vol. 63, no. 1, pp. 206–214, Feb. 2021, doi: 10.1109/TEMC.2020.3010058.
[78] M. Raya and R. Vick, "Spice models of shielded single and multiconductor cables for emc analyses," *IEEE Trans. Electromagn. Compat.*, vol. 62, no. 4, pp. 1563–1571, Aug. 2020, doi: 10.1109/TEMC.2020.3006391.
[79] A. Kalantarnia, A. Keshtkar, and A. Ghorbani, "Predicting the effects of HPEM radiation on a transmission line terminated with linear/nonlinear load in perforated metallic enclosure using fddm/vf," *IEEE Trans. Plasma Sci.*, vol. 48, no. 3, pp. 669–675, Mar. 2020, doi: 10.1109/TPS.2020.2968759.
[80] R. Michels, M. Willenbockel, and F. Gronwald, "A Parametric Study of an Energy Storage Effect due to Nonlinear Components and HPEM-Excitation," in *2019 International Symposium on Electromagnetic Compatibility - EMC EUROPE*, Sep. 2019, pp. 59–64. doi: 10.1109/EMCEurope.2019.8871855.
[81] J. T. Williams, L. D. Bacon, M. J. Walker, and E. C. Zeek, "A robust approach for the analysis of EMI/EMC problems with nonlinear circuit loads," *IEEE Trans. Electromagn. Compat.*, vol. 57, no. 4, pp. 680–687, Aug. 2015, doi: 10.1109/TEMC.2015.2438065.
[82] M. Kotzev, X. Bi, M. Kreitlow, and F. Gronwald, "Equivalent circuit simulation of hpem-induced transient responses at nonlinear loads," *Adv. Radio Sci.*, vol. 15, pp. 175–180, Sep. 2017, doi: 10.5194/ars-15-175-2017.
[83] S. T. Op 't Land, M. Ramdani, R. Perdriau, M. Leone, and M. Drissi, "Simple, taylor-based worst-case model for field-to-line coupling," *Prog. Electromagn. Res.*, vol. 140, pp. 297–311, 2013, doi: 10.2528/PIER13041207.

[84] D. Poljak and K. El Khamlichi Drissi, “Electromagnetic field coupling to overhead wire configurations: antenna model versus transmission line approach,” *International Journal of Antennas and Propagation*, 2012. https://www.hindawi.com/journals/ijap/2012/730145/ (accessed Nov. 12, 2018).
[85] M. Cabedo-Fabres, E. Antonino-Daviu, A. Valero-Nogueira, and M. F. Bataller, “The theory of characteristic modes revisited: a contribution to the design of antennas for modern applications,” *IEEE Antennas Propag. Mag.*, vol. 49, no. 5, pp. 52–68, Oct. 2007, doi: 10.1109/MAP.2007.4395295.
[86] A. M. Hassan, F. Vargas-Lara, J. F. Douglas, and E. J. Garboczi, “Electromagnetic resonances of individual single-walled carbon nanotubes with realistic shapes: a characteristic modes approach,” *IEEE Trans. Antennas Propag.*, vol. 64, no. 7, pp. 2743–2757, Jul. 2016, doi: 10.1109/TAP.2016.2526046.
[87] M. Ali, S. S. Stuchly, and K. Caputa, “Characteristics of bent wire antennas,” *J. Electromagn. Waves Appl.*, vol. 9, no. 9, pp. 1149–1162, Jan. 1995, doi: 10.1163/156939395X00785.
[88] H. Nakano, H. Tagami, A. Yoshizawa, and J. Yamauchi, “Shortening ratios of modified dipole antennas,” *IEEE Trans. Antennas Propag.*, vol. 32, no. 4, pp. 385–386, Apr. 1984, doi: 10.1109/TAP.1984.1143321.
[89] J. J. Adams and J. T. Bernhard, “Broadband equivalent circuit models for antenna impedances and fields using characteristic modes,” *IEEE Trans. Antennas Propag.*, vol. 61, no. 8, pp. 3985–3994, Aug. 2013, doi: 10.1109/TAP.2013.2261852.
[90] M. Wang, M. R. Khan, M. D. Dickey, and J. J. Adams, “A compound frequency- and polarization- reconfigurable crossed dipole using multidirectional spreading of liquid metal,” *IEEE Antennas Wirel. Propag. Lett.*, vol. 16, pp. 79–82, 2017, doi: 10.1109/LAWP.2016.2556983.
[91] S. Herasati and L. Zhang, “A new method for characterizing and modeling the waviness and alignment of carbon nanotubes in composites,” *Compos. Sci. Technol.*, vol. 100, pp. 136–142, Aug. 2014, doi: 10.1016/j.compscitech.2014.06.004.
[92] T. Nakamura, N. Hayashi, H. Fukuda, and S. Yokokawa, “Radiation from the transmission line with an acute bend,” *IEEE Trans. Electromagn. Compat.*, vol. 37, no. 3, pp. 317–325, Aug. 1995, doi: 10.1109/15.406521.
[93] X. Lu, G. Wei, X. Pan, L. Fan, and H. Wan, “Dual-port pulsed differential-mode current injection method for high-level electromagnetic pulse radiated susceptibility testing,” *IET Sci. Meas. Technol.*, vol. 10, no. 5, pp. 505–512, 2016, doi: 10.1049/iet-smt.2015.0251.
[94] J. Jia, D. Rinas, and S. Frei, “Prediction of radiated fields from cable bundles based on current distribution measurements,” in *International Symposium on Electromagnetic Compatibility - EMC EUROPE*, Sep. 2012, pp. 1–7. doi: 10.1109/EMCEurope.2012.6396759.
[95] N. Toscani, G. Spadacini, F. Grassi, and S. A. Pignari, “Lumped and distributed-parameter circuit models of the electromagnetic clamp,” *IEEE Trans. Electromagn. Compat.*, vol. 58, no. 4, pp. 1007–1015, Aug. 2016, doi: 10.1109/TEMC.2016.2549702.
[96] L. Badini, G. Spadacini, F. Grassi, S. A. Pignari, and P. Pelissou, “A rationale for statistical correlation of conducted and radiated susceptibility testing in aerospace emc,” *IEEE Trans. Electromagn. Compat.*, vol. 59, no. 5, pp. 1576–1585, Oct. 2017, doi: 10.1109/TEMC.2017.2678762.

[97] B. I. Intelligence, “Drones are about to fill the skies within the next 5 years,” *Business Insider*.

[98] P. Zhan, D. W. Casbeer, and A. L. Swindlehurst, “A centralized control algorithm for target tracking with uavs,” in *Conference Record of the Thirty-Ninth Asilomar Conference onSignals, Systems and Computers, 2005.*, Oct. 2005, pp. 1148–1152. doi: 10.1109/ACSSC.2005.1599940.

[99] J. R. Insua, S. A. Utsumi, and B. Basso, “Estimation of spatial and temporal variability of pasture growth and digestibility in grazing rotations coupling unmanned aerial vehicle (uav) with crop simulation models,” *PLOS ONE*, vol. 14, no. 3, p. e0212773, Mar. 2019, doi: 10.1371/journal.pone.0212773.

[100] J. Kim and J. P. Hespanha, “Cooperative radar jamming for groups of unmanned air vehicles,” in *2004 43rd IEEE Conference on Decision and Control (CDC) (IEEE Cat. No.04CH37601)*, Dec. 2004, vol. 1, pp. 632-637 Vol.1. doi: 10.1109/CDC.2004.1428715.

[101] D. W. Casbeer, R. W. Beard, T. W. McLain, Sai-Ming Li, and R. K. Mehra, “Forest fire monitoring with multiple small uavs,” in *Proceedings of the 2005, American Control Conference, 2005.*, Jun. 2005, pp. 3530–3535 vol. 5. doi: 10.1109/ACC.2005.1470520.

[102] Z. Xiao, P. Xia, and X. Xia, “Enabling uav cellular with millimeter-wave communication: potentials and approaches,” *IEEE Commun. Mag.*, vol. 54, no. 5, pp. 66–73, May 2016, doi: 10.1109/MCOM.2016.7470937.

[103] M. Mozaffari, W. Saad, M. Bennis, and M. Debbah, “Unmanned aerial vehicle with underlaid device-to-device communications: performance and tradeoffs,” *IEEE Trans. Wirel. Commun.*, vol. 15, no. 6, pp. 3949–3963, Jun. 2016, doi: 10.1109/TWC.2016.2531652.

[104] C. Zhan, Y. Zeng, and R. Zhang, “Energy-efficient data collection in uav enabled wireless sensor network,” *IEEE Wirel. Commun. Lett.*, vol. 7, no. 3, pp. 328–331, Jun. 2018, doi: 10.1109/LWC.2017.2776922.

[105] J. Lyu, Y. Zeng, R. Zhang, and T. J. Lim, “Placement optimization of uav-mounted mobile base stations,” *IEEE Commun. Lett.*, vol. 21, no. 3, pp. 604–607, Mar. 2017, doi: 10.1109/LCOMM.2016.2633248.

[106] T. Li, B. Wen, Y. Tian, Z. Li, and S. Wang, “Numerical simulation and experimental analysis of small drone rotor blade polarimetry based on rcs and micro-doppler signature,” *IEEE Antennas Wirel. Propag. Lett.*, vol. 18, no. 1, pp. 187–191, Jan. 2019, doi: 10.1109/LAWP.2018.2885373.

[107] A. V. Khristenko *et al.*, “Magnitude and spectrum of electromagnetic wave scattered by small quadcopter in x -band,” *IEEE Trans. Antennas Propag.*, vol. 66, no. 4, pp. 1977–1984, Apr. 2018, doi: 10.1109/TAP.2018.2800640.

[108] L. Jansson and M. Backstrom, “Directivity of equipment and its effect on testing in mode-stirred and anechoic chamber,” in *1999 IEEE International Symposium on Electromagnetic Compatability. Symposium Record (Cat. No.99CH36261)*, Aug. 1999, vol. 1, pp. 17–22 vol.1. doi: 10.1109/ISEMC.1999.812860.

[109] M. Hoijer and V. Isovic, “Frequency resolved susceptibility testing as a substitute for angular resolved susceptibility testing,” in *2004 International Symposium on Electromagnetic Compatibility (IEEE Cat. No.04CH37559)*, Aug. 2004, vol. 1, pp. 29–34 vol.1. doi: 10.1109/ISEMC.2004.1349991.

[110] “En 61000-4-3 - electromagnetic compatibility (emc) - part 4-3: testing and measurement techniques - radiated, radio frequency, electromagnetic field immunity test.” https://webstore.iec.ch/publication/59849

[111] S. Kim, Y. Noh, J. Lee, J. Lee, J. Choi, and J. Yook, “Electromagnetic signature of a quadcopter drone and its relationship with coupling mechanisms,” *IEEE Access*, vol. 7, pp. 174764–174773, 2019, doi: 10.1109/ACCESS.2019.2956499.

[112] M. Cabedo-Fabres, E. Antonino-Daviu, A. Valero-Nogueira, and M. F. Bataller, “The theory of characteristic modes revisited: a contribution to the design of antennas for modern applications,” *IEEE Antennas Propag. Mag.*, vol. 49, no. 5, pp. 52–68, Oct. 2007, doi: 10.1109/MAP.2007.4395295.

[113] S. Dey, D. Chatterjee, E. J. Garboczi, and A. M. Hassan, “Plasmonic nanoantenna optimization using characteristic mode analysis,” *IEEE Trans. Antennas Propag.*, vol. 68, no. 1, pp. 43–53, Jan. 2020, doi: 10.1109/TAP.2019.2938705.

[114] K. C. Durbhakula *et al.*, “Electromagnetic scattering from individual crumpled graphene flakes: a characteristic modes approach,” *IEEE Trans. Antennas Propag.*, vol. 65, no. 11, pp. 6035–6047, Nov. 2017, doi: 10.1109/TAP.2017.2752218.

[115] A. M. Hassan, F. Vargas-Lara, J. F. Douglas, and E. J. Garboczi, “Electromagnetic resonances of individual single-walled carbon nanotubes with realistic shapes: a characteristic modes approach,” *IEEE Trans. Antennas Propag.*, vol. 64, no. 7, pp. 2743–2757, Jul. 2016, doi: 10.1109/TAP.2016.2526046.

[116] Y. Chen and C. Wang, “Electrically small uav antenna design using characteristic modes,” *IEEE Trans. Antennas Propag.*, vol. 62, no. 2, pp. 535–545, Feb. 2014, doi: 10.1109/TAP.2013.2289999.

[117] S. Sow, L. Guo, S. Zhou, and T. Chio, “Electrically small structural antenna design for small uav based on characteristics modes,” in *2017 11th European Conference on Antennas and Propagation (EUCAP)*, Mar. 2017, pp. 2134–2138. doi: 10.23919/EuCAP.2017.7928206.

[118] M. Z. M. Hamdalla, A. N. Caruso, and A. M. Hassan, “Predicting electromagnetic interference to a terminated wire using characteristic mode analysis,” in *2020 International Applied Computational Electromagnetics Society Symposium (ACES)*, Jul. 2020, pp. 1–2. doi: 10.23919/ACES49320.2020.9196133.

[119] M. Z. M. Hamdalla, A. M. Hassan, and A. N. Caruso, “Characteristic mode analysis of the effect of the uav frame material on coupling and interference,” in *2019 IEEE International Symposium on Antennas and Propagation and USNC-URSI Radio Science Meeting*, Jul. 2019, pp. 1497–1498. doi: 10.1109/APUSNCURSINRSM.2019.8888344.

[120] M. Z. M. Hamdalla, B. B. Bissen, A. N. Caruso, and A. M. Hassan, “Experimental validations of characteristic mode analysis predictions using gtem measurements,” in *2020 IEEE International Symposium on Antennas and Propagation and North American Radio Science Meeting*, Jul. 2020, pp. 1799–1800. doi: 10.1109/IEEECONF35879.2020.9330415.

[121] M. Z. M. Hamdalla *et al.*, “Electromagnetic interference of unmanned aerial vehicles: a characteristic mode analysis approach,” in *2019 IEEE International Symposium on Antennas and Propagation and USNC-URSI Radio Science Meeting*, Jul. 2019, pp. 553–554. doi: 10.1109/APUSNCURSINRSM.2019.8888398.

[122] F. A. Dicandia, S. Genovesi, and A. Monorchio, “Efficient excitation of characteristic modes for radiation pattern control by using a novel balanced inductive coupling

element," *IEEE Trans. Antennas Propag.*, vol. 66, no. 3, pp. 1102–1113, Mar. 2018, doi: 10.1109/TAP.2018.2790046.
[123] S. Ghosal, A. De, A. P. Duffy, and A. Chakrabarty, "Selection of dominant characteristic modes," *IEEE Trans. Electromagn. Compat.*, vol. 62, no. 2, pp. 451–460, Apr. 2020, doi: 10.1109/TEMC.2019.2909932.
[124] Y. S. Cao, Y. Wang, L. Jiang, A. E. Ruehli, J. Fan, and J. L. Drewniak, "Quantifying emi: a methodology for determining and quantifying radiation for practical design guidelines," *IEEE Trans. Electromagn. Compat.*, vol. 59, no. 5, pp. 1424–1432, Oct. 2017, doi: 10.1109/TEMC.2017.2677199.
[125] Q. Wu, H. Bruns, and C. Schuster, "Characteristic mode analysis of radiating structures in digital systems," *IEEE Electromagn. Compat. Mag.*, vol. 5, no. 4, pp. 56–63, Fourth 2016, doi: 10.1109/MEMC.2016.7866235.
[126] X. Wang *et al.*, "Investigation of the radiation mechanism for high-speed connectors," in *2017 IEEE 26th Conference on Electrical Performance of Electronic Packaging and Systems (EPEPS)*, Oct. 2017, pp. 1–3. doi: 10.1109/EPEPS.2017.8329711.
[127] X. Yang *et al.*, "EMI radiation mitigation for heatsinks using characteristic mode analysis," in *2018 IEEE Symposium on Electromagnetic Compatibility, Signal Integrity and Power Integrity (EMC, SI PI)*, Jul. 2018, pp. 374–378. doi: 10.1109/EMCSI.2018.8495291.
[128] Y. S. Cao, M. Ouyanz, Y. Wang, and J. Fan, "Emi modeling for antenna-chassis system using characteristic mode analysis," in *2018 IEEE Symposium on Electromagnetic Compatibility, Signal Integrity and Power Integrity (EMC, SI PI)*, Jul. 2018, pp. 181–186. doi: 10.1109/EMCSI.2018.8495389.
[129] R. Ma and N. Behdad, "Design of platform-based hf direction-finding antennas using the characteristic mode theory," *IEEE Trans. Antennas Propag.*, vol. 67, no. 3, pp. 1417–1427, Mar. 2019, doi: 10.1109/TAP.2018.2884878.
[130] C. Wang, Y. Chen, G. Liu, and S. Yang, "Aircraft-integrated VHF band antenna array designs using characteristic modes," *IEEE Trans. Antennas Propag.*, vol. 68, no. 11, pp. 7358–7369, Nov. 2020, doi: 10.1109/TAP.2020.2997468.
[131] J. Hunter, Y. Liu, D. Floyd, A. Hassan, V. Khilkevich, and D. Beetner, "Characterization of the electromagnetic coupling to uavs," presented at the Annual Directed Energy Science and Technology Symposium, Mar. 2018.
[132] R. Garbacz and E. Newman, "Characteristic modes of a symmetric wire cross," *IEEE Trans. Antennas Propag.*, vol. 28, no. 5, pp. 712–715, Sep. 1980, doi: 10.1109/TAP.1980.1142388.
[133] N. Peitzmeier and D. Manteuffel, "Upper bounds and design guidelines for realizing uncorrelated ports on multimode antennas based on symmetry analysis of characteristic modes," *IEEE Trans. Antennas Propag.*, vol. 67, no. 6, pp. 3902–3914, Jun. 2019, doi: 10.1109/TAP.2019.2905718.
[134] M. Sadraey, "Unmanned aircraft design: a review of fundamentals," *Synth. Lect. Mech. Eng.*, vol. 1, no. 2, pp. i–193, Sep. 2017, doi: 10.2200/S00789ED1V01Y201707MEC004.
[135] "ah-systems-bcp-500-series_manual.pdf." Accessed: Sep. 09, 2021. [Online]. Available: https://www.atecorp.com/atecorp/media/pdfs/data-sheets/ah-systems-bcp-500-series_manual.pdf
[136] C. R. Paul, *Introduction to electromagnetic compatibility*. John Wiley & Sons, 2006.

[137] D. Giordan *et al.*, "The use of unmanned aerial vehicles (uavs) for engineering geology applications," *Bull. Eng. Geol. Environ.*, vol. 79, no. 7, pp. 3437–3481, Sep. 2020, doi: 10.1007/s10064-020-01766-2.

[138] Y. Wu, K. H. Low, and C. Lv, "Cooperative path planning for heterogeneous unmanned vehicles in a search-and-track mission aiming at an underwater target," *IEEE Trans. Veh. Technol.*, vol. 69, no. 6, pp. 6782–6787, Jun. 2020, doi: 10.1109/TVT.2020.2991983.

[139] Y. Sh. Alqudsi, A. S. Alsharafi, and A. Mohamed, "A Review of Airborne Landmine Detection Technologies: Unmanned Aerial Vehicle-Based Approach," in *2021 International Congress of Advanced Technology and Engineering (ICOTEN)*, Jul. 2021, pp. 1–5. doi: 10.1109/ICOTEN52080.2021.9493528.

[140] S. Prager, G. Sexstone, D. McGrath, J. Fulton, and M. Moghaddam, "Snow Depth Retrieval With an Autonomous UAV-Mounted Software-Defined Radar," *IEEE Trans. Geosci. Remote Sens.*, pp. 1–16, 2021, doi: 10.1109/TGRS.2021.3117509.

[141] R. Akbar, S. Prager, A. R. Silva, M. Moghaddam, and D. Entekhabi, "Wireless Sensor Network Informed UAV Path Planning for Soil Moisture Mapping," *IEEE Trans. Geosci. Remote Sens.*, pp. 1–13, 2021, doi: 10.1109/TGRS.2021.3088658.

[142] S. Hayat, E. Yanmaz, and R. Muzaffar, "Survey on Unmanned Aerial Vehicle Networks for Civil Applications: A Communications Viewpoint," *IEEE Commun. Surv. Tutor.*, vol. 18, no. 4, pp. 2624–2661, 2016, doi: 10.1109/COMST.2016.2560343.

[143] H. Shakhatreh *et al.*, "Unmanned Aerial Vehicles (UAVs): A Survey on Civil Applications and Key Research Challenges," *IEEE Access*, vol. 7, pp. 48572–48634, 2019, doi: 10.1109/ACCESS.2019.2909530.

[144] X. Zhong, Y. Guo, N. Li, Y. Chen, and S. Li, "Deployment optimization of uav relay for malfunctioning base station: model-free approaches," *IEEE Trans. Veh. Technol.*, vol. 68, no. 12, pp. 11971–11984, Dec. 2019, doi: 10.1109/TVT.2019.2947078.

[145] Y. Yin, M. Liu, G. Gui, H. Gacanin, H. Sari, and F. Adachi, "Cross-layer resource allocation for uav-assisted wireless caching networks with noma," *IEEE Trans. Veh. Technol.*, vol. 70, no. 4, pp. 3428–3438, Apr. 2021, doi: 10.1109/TVT.2021.3064032.

[146] Y.-Y. Jeong and W.-S. Lee, "Wideband Printed Half Bow-Tie Antenna Array Based on a Quad-Mode Reconfigurable Feeding Network for UAV Communications," *IEEE Open J. Antennas Propag.*, vol. 2, pp. 238–248, 2021, doi: 10.1109/OJAP.2021.3057067.

[147] Z. Akhter, R. M. Bilal, and A. Shamim, "A Dual Mode, Thin and Wideband MIMO Antenna System for Seamless Integration on UAV," *IEEE Open J. Antennas Propag.*, vol. 2, pp. 991–1000, 2021, doi: 10.1109/OJAP.2021.3115025.

[148] P. Liu, W. Jiang, W. Hu, S.-Y. Sun, and S.-X. Gong, "Wideband Multimode Filtering Circular Patch Antenna," *IEEE Trans. Antennas Propag.*, vol. 69, no. 11, pp. 7249–7259, Nov. 2021, doi: 10.1109/TAP.2021.3070717.

[149] J.-J. Peng, S.-W. Qu, M. Xia, and S. Yang, "Conformal Phased Array Antenna for Unmanned Aerial Vehicle With ±70° Scanning Range," *IEEE Trans. Antennas Propag.*, vol. 69, no. 8, pp. 4580–4587, Aug. 2021, doi: 10.1109/TAP.2021.3060125.

[150] J. Rodríguez-Piñeiro, T. Domínguez-Bolaño, X. Cai, Z. Huang, and X. Yin, "Air-to-Ground Channel Characterization for Low-Height UAVs in Realistic Network Deployments," *IEEE Trans. Antennas Propag.*, vol. 69, no. 2, pp. 992–1006, Feb. 2021, doi: 10.1109/TAP.2020.3016164.

[151] K. Sun, M. Zhang, and D. Yang, “A new interference detection method based on joint hybrid time–frequency distribution for gnss receivers,” *IEEE Trans. Veh. Technol.*, vol. 65, no. 11, pp. 9057–9071, Nov. 2016, doi: 10.1109/TVT.2016.2515718.

[152] Z. Wang, R. Liu, Q. Liu, L. Han, and J. S. Thompson, “Feasibility Study of Uav-Assisted Anti-Jamming Positioning,” *IEEE Trans. Veh. Technol.*, vol. 70, no. 8, pp. 7718–7733, Aug. 2021, doi: 10.1109/TVT.2021.3090403.

[153] L. Zhang, L. Huang, B. Li, M. Huang, J. Yin, and W. Bao, “Fast-moving jamming suppression for uav navigation: a minimum dispersion distortionless response beamforming approach,” *IEEE Trans. Veh. Technol.*, vol. 68, no. 8, pp. 7815–7827, Aug. 2019, doi: 10.1109/TVT.2019.2924951.

[154] R. Kanyou Nana, S. Korte, S. Dickmann, H. Garbe, and F. Sabath, “Estimation of the threat of IEMI to complex electronic systems,” in *Advances in Radio Science*, May 2009, vol. 7, no. E.1, pp. 249–253. doi: 10.5194/ars-7-249-2009.

[155] M. Hamdalla *et al.*, “Prediction of experimental electromagnetic coupling to a uav model using characteristic mode analysis,” Jul. 2021, doi: 10.36227/techrxiv.14842749.v1.

[156] C. Chen *et al.*, “Simulation and analysis of emp transient electromagnetic effect of aircraft,” *J. Eng.*, vol. 2019, no. 16, pp. 2464–2467, 2019, doi: 10.1049/joe.2018.8615.

[157] K. Yu Sakharov, A. V. Sukhov, V. L. Ugolev, and Yu. M. Gurevich, “Study of uwb electromagnetic pulse impact on commercial unmanned aerial vehicle,” in *2018 International Symposium on Electromagnetic Compatibility (EMC EUROPE)*, Aug. 2018, pp. 40–43. doi: 10.1109/EMCEurope.2018.8484992.

[158] S. Ibeobi and X. Pan, “Study of electromagnetic pulse (emp) effect on surveillance unmanned aerial vehicles (uavs),” *J. Mech. Eng. Autom. Control Syst.*, vol. 2, no. 1, Art. no. 1, 2021, doi: 10.21595/jmeacs.2021.21926.

[159] Y.-F. Qian, B. Du, Z.-F. Ye, and H.-B. Zhang, “Simulation on transient electromagnetic influence of lightning strike for turboprop engine,” in *2019 4th International Conference on Electrical, Electronics, Communication, Computer Technologies and Optimization Techniques (ICEECCOT)*, Dec. 2019, pp. 1–7. doi: 10.1109/ICEECCOT46775.2019.9114767.

[160] H. Xie, J. Wang, R. Fan, and Y. Liu, “Spice models for radiated and conducted susceptibility analyses of multiconductor shielded,” in *Progress In Electromagnetics Research, Vol. 125, 2012 93 cables,” Progress In Electromagnetics Research*, pp. 241–257.

[161] D. Palur Palanivelu, R. Michels, M. Kreitlow, and F. Gronwald, “The response of nonlinearly loaded antennas to repetitive HPEM excitations as obtained from equivalent circuit models,” *Adv. Radio Sci.*, vol. 16, pp. 135–140, Sep. 2018, doi: 10.5194/ars-16-135-2018.

[162] G. Antonini, “Spice equivalent circuits of frequency-domain responses,” *IEEE Trans. Electromagn. Compat.*, vol. 45, no. 3, pp. 502–512, Aug. 2003, doi: 10.1109/TEMC.2003.815528.

[163] B. Gustavsen and C. Heitz, “Modal vector fitting: a tool for generating rational models of high accuracy with arbitrary terminal conditions,” *IEEE Trans. Adv. Packag.*, vol. 31, no. 4, pp. 664–672, Nov. 2008, doi: 10.1109/TADVP.2008.927810.

[164] B. Gustavsen, “Fast Passivity Enforcement for S-Parameter Models by Perturbation of Residue Matrix Eigenvalues,” *IEEE Trans. Adv. Packag.*, vol. 33, no. 1, pp. 257–265, Feb. 2010, doi: 10.1109/TADVP.2008.2010508.
[165] B. Gustavsen and A. Semlyen, “Rational approximation of frequency domain responses by vector fitting,” *IEEE Trans. Power Deliv.*, vol. 14, no. 3, pp. 1052–1061, Jul. 1999, doi: 10.1109/61.772353.
[166] B. Gustavsen and C. Heitz, “Fast Realization of the Modal Vector Fitting Method for Rational Modeling With Accurate Representation of Small Eigenvalues,” *IEEE Trans. Power Deliv.*, vol. 24, no. 3, pp. 1396–1405, Jul. 2009, doi: 10.1109/TPWRD.2008.2005462.
[167] “Ltspice simulator | analog devices.” https://www.analog.com/en/design-center/design-tools-and-calculators/ltspice-simulator.html
[168] V. Koo *et al.*, “A new unmanned aerial vehicle synthetic aperture radar for environmental monitoring,” *Prog. Electromagn. Res.*, vol. 122, pp. 245–268, 2012, doi: 10.2528/PIER11092604.
[169] Y. Kawamoto, H. Nishiyama, N. Kato, F. Ono, and R. Miura, “Toward future unmanned aerial vehicle networks: architecture, resource allocation and field experiments,” *IEEE Wirel. Commun.*, vol. 26, no. 1, pp. 94–99, Feb. 2019, doi: 10.1109/MWC.2018.1700368.
[170] G. Park, K. Park, and B. Song, “Spatio-temporal change monitoring of outside manure piles using unmanned aerial vehicle images,” *Drones*, vol. 5, no. 1, Art. no. 1, Mar. 2021, doi: 10.3390/drones5010001.
[171] B. Li, Z. Fei, and Y. Zhang, “Uav communications for 5g and beyond: recent advances and future trends,” *IEEE Internet Things J.*, vol. 6, no. 2, pp. 2241–2263, Apr. 2019, doi: 10.1109/JIOT.2018.2887086.
[172] N. González-Prelcic, R. W. Heath, C. Rusu, and A. Klautau, “High-capacity millimeter wave uav communications,” in *UAV Communications for 5G and Beyond*, John Wiley & Sons, Ltd, 2020, pp. 203–229. doi: 10.1002/9781119575795.ch8.
[173] M. A. Abdel-Malek, N. Saputro, A. S. Ibrahim, and K. Akkaya, “Uav-assisted multi-path parallel routing for mmwave-based wireless networks,” *Internet Things*, vol. 14, p. 100366, Jun. 2021, doi: 10.1016/j.iot.2021.100366.
[174] F. Zhou, R. Wang, and and J. Bian, “Joint trajectories and power allocation design for dual uav-enabled secrecy swipt networks,” *Prog. Electromagn. Res. M*, vol. 87, pp. 73–82, 2019, doi: 10.2528/PIERM19092802.
[175] “The role of drones in future terrorist attacks,” *AUSA*, Feb. 26, 2021. https://www.ausa.org/publications/role-drones-future-terrorist-attacks (accessed Jun. 13, 2021).
[176] D. Zhang, M. Zhao, E. Cheng, and Y. Chen, “GPR-based emi prediction for uav’s dynamic datalink,” *IEEE Trans. Electromagn. Compat.*, vol. 63, no. 1, pp. 19–29, Feb. 2021, doi: 10.1109/TEMC.2020.3000919.
[177] L. Bo, Z. Shengbing, Y. Junpeng, and W. Liang, “An anti-interference method for about unmanned aerial vehicle flight data based on vxworks,” in *2016 IEEE Chinese Guidance, Navigation and Control Conference (CGNCC)*, Aug. 2016, pp. 7–9. doi: 10.1109/CGNCC.2016.7828748.
[178] S. Fernández Romero, P. López Rodríguez, D. Escot Bocanegra, D. Poyatos Martínez, and M. Añón Cancela, “Comparing open area test site and resonant chamber for

unmanned aerial vehicle's high-intensity radiated field testing," *IEEE Trans. Electromagn. Compat.*, vol. 60, no. 6, pp. 1704–1711, Dec. 2018, doi: 10.1109/TEMC.2017.2747771.

[179] A. M. and B. R. Behera, "Characteristics mode analysis: a review of its concepts, recent trends, state-of-the-art developments and its interpretation with a fractal uwb mimo antenna," *Prog. Electromagn. Res. B*, vol. 92, pp. 19–45, 2021, doi: 10.2528/PIERB21020506.

[180] M. Meng and Z. Nie, "Study on characteristic mode analysis of three-dimensional conducting objects in lossless layered medium," *IEEE Access*, vol. 6, pp. 77606–77614, 2018, doi: 10.1109/ACCESS.2018.2883577.

[181] J. Ückerseifer and F. Gronwald, "Characteristic mode analysis of surface current distributions on metallic structures exposed to HIRF- and DCI-excitations," *Adv. Radio Sci.*, vol. 18, pp. 33–41, Dec. 2020, doi: 10.5194/ars-18-33-2020.

[182] M. Rothenhäusler and F. Gronwald, "Characteristic mode analysis of hirf- and dci-excitations of an aircraft structure," in *2017 International Symposium on Electromagnetic Compatibility - EMC EUROPE*, Sep. 2017, pp. 1–6. doi: 10.1109/EMCEurope.2017.8094764.

[183] Q. Wu, "Characteristic mode analysis of composite metallic–dielectric structures using impedance boundary condition," *IEEE Trans. Antennas Propag.*, vol. 67, no. 12, pp. 7415–7424, Dec. 2019, doi: 10.1109/TAP.2019.2934902.

[184] Q. Wu, "Characteristic mode assisted design of dielectric resonator antennas with feedings," *IEEE Trans. Antennas Propag.*, vol. 67, no. 8, pp. 5294–5304, Aug. 2019, doi: 10.1109/TAP.2019.2916763.

VITA

Mohamed Hamdalla received the B.Sc. degree and the M.Sc. in electronics and communications engineering from Arab Academy for Science, Technology, and Maritime Transport. Alexandria, Egypt in 2012 and 2016, respectively.

During his tenure of Ph.D. study at the University of Missouri-Kansas City, Mr. Hamdalla received the School of Graduate Studies Research Grant in the 2019-2020 session. He also received the UMKC Missouri Institute of Defense and Energy (MIDE) Spring Semester Student Spotlight Award in May-2021. His research interests include Antennas, Metamaterials, Microwave Filters, electromagnetic compatibility and interference, characteristic mode theory, and applications.